University of Alberta

OPTICAL AND STRUCTURAL PROPERTIES OF QUINOLINE METAL CHELATE THIN FILMS DEPOSITED BY GLANCING ANGLE DEPOSITION

by

Bryan Seung Chi Szeto

A thesis submitted to the Faculty of Graduate Studies and Research in partial fulfillment of the requirements for the degree of **Master of Science**.

Department of Electrical and Computer Engineering

Edmonton, Alberta
Fall 2007

Library and Archives Canada

Published Heritage Branch

395 Wellington Street
Ottawa ON K1A 0N4
Canada

Bibliothèque et Archives Canada

Direction du Patrimoine de l'édition

395, rue Wellington
Ottawa ON K1A 0N4
Canada

Your file Votre référence
ISBN: 978-0-494-33357-0
Our file Notre référence
ISBN: 978-0-494-33357-0

NOTICE:
The author has granted a non-exclusive license allowing Library and Archives Canada to reproduce, publish, archive, preserve, conserve, communicate to the public by telecommunication or on the Internet, loan, distribute and sell theses worldwide, for commercial or non-commercial purposes, in microform, paper, electronic and/or any other formats.

The author retains copyright ownership and moral rights in this thesis. Neither the thesis nor substantial extracts from it may be printed or otherwise reproduced without the author's permission.

AVIS:
L'auteur a accordé une licence non exclusive permettant à la Bibliothèque et Archives Canada de reproduire, publier, archiver, sauvegarder, conserver, transmettre au public par télécommunication ou par l'Internet, prêter, distribuer et vendre des thèses partout dans le monde, à des fins commerciales ou autres, sur support microforme, papier, électronique et/ou autres formats.

L'auteur conserve la propriété du droit d'auteur et des droits moraux qui protège cette thèse. Ni la thèse ni des extraits substantiels de celle-ci ne doivent être imprimés ou autrement reproduits sans son autorisation.

In compliance with the Canadian Privacy Act some supporting forms may have been removed from this thesis.

While these forms may be included in the document page count, their removal does not represent any loss of content from the thesis.

Conformément à la loi canadienne sur la protection de la vie privée, quelques formulaires secondaires ont été enlevés de cette thèse.

Bien que ces formulaires aient inclus dans la pagination, il n'y aura aucun contenu manquant.

Canada

Abstract

Highly porous organic nanostructured thin films of quinoline metal chelates have been fabricated using glancing angle deposition (GLAD). GLAD is a physical vapour deposition technique that enables precision nanostructured thin film features to be fabricated in a single step process. Quinoline GLAD films have demonstrated a notable absence of column broadening and a predominantly circular column cross-section, which is contrary to the secondary structural anisotropy commonly observed in inorganic GLAD films. These structural properties give rise to an optical anisotropy leading to negative values of in-plane birefringence that increases with deposition angle. The structure and optical anisotropy of the films were characterized using variable angle spectroscopic ellipsometry, Bruggeman effective medium approximations and scanning electron microscopy. Another unique feature of the organic films was the formation a solid wetting layer prior to nanostructure growth. The effects of substrate surface energy and vapor deposition rate on the initial wetting layer growth of porous columnar tris(8-hydroxyquinoline) aluminum (Alq_3) nanostructures are described.

Acknowledgements

First off, I would like to thank my supervisor Dr. Michael Brett for giving me this opportunity and for his guidance and support in all aspects.

I would like to thank Dr. Jeremy Sit and Dr. Jonathan Veinot for their invaluable advice.

I would also like to thank all the members of the GLAD group past and present (Dr. Peter Hrudey, Shufen Tsoi, Graeme Dice, Nick Wakefield, James Gospodyn, Andy van Popta, John Steele, Mark Summers, Matthew Hawkeye, Doug Gish, Jason Sorge, Katie Krause, Dr. Anastasia Elias, Louis Bezuidenhout, Sumudu Fernando, Dr. Mike Fleischauer, Dr. Mike Taschuk, Dr. Doug Vick, Karin Hayward, and Ben Bathgate) for making this experience so special.

A special thanks to George Braybrook for all his excellent SEM images which was essential for this work.

Finally, thanks to all my family and friends for all their support and encouragement in this endeavor called a MSc.

Table of Contents

1 Introduction **1**

1.1 Motivation 1

1.2 Scope 2

1.3 Thin films 2

1.4 Growth mechanics of evaporated thin films 3

1.5 Glancing angle deposition 4

1.5.1 Background 4

1.5.2 Fabrication methodology of GLAD structures 6

1.5.3 Nanostructure arrangement 8

1.6 Organics 9

2 Alq_3 nanostructured thin films **13**

2.1 Fabrication 13

2.2 Alq_3 morphologies 14

2.3 Summary 23

3 Control of wetting layer thickness **24**

3.1 Wetting layer vs deposition angle 24

3.2 Functionalization of substrate surface 27

3.2.1 Substrate preparation 27

3.2.2 Characterization of functionalized substrates 28

3.2.3 Control via surface functionalization and deposition rate 30

3.3 Summary 36

4 Optical properties of Alq_3 columnar thin films **37**

4.1 Background Optics 38

4.1.1 Linear Birefringence 38

4.1.2 Circular Bragg effect 42

4.2 Variable angle spectroscopic ellipsometry 43

4.3 Bruggeman effective medium approximation 50

4.3.1 Column Angle 54

4.3.2 Density and indices 54

4.3.3 Birefringence of Alq_3 columnar thin films 58

4.4 Summary 62

5 Optical and structural comparison of quinoline metal chelate thin films **63**

5.1 Basic properties 63

5.2 Index of refraction of solid films 64

5.3 Comparison of nanostructured quinoline films 65

5.3.1 Circular polarization 68

5.4 Summary 72

6 Conclusions and recommendations for future work **73**

6.1 Conclusions 73

6.2 Recommendations for future work 75

6.2.1 Investigations of other organic materials 75

6.2.2 Fundamental studies 75

Bibliography **76**

A Maple Code **84**

List of Tables

3.1 Advancing contact angle (θ) and RMS surface roughness of as-supplied, RIE-treated, and alkyltrichlorosilane derivatized Si substrates and the corresponding wetting layer thickness (WLT) of thermally evaporated Alq_3 thin films. 33

5.1 Properties of quinoline metal chelates. 64

5.2 Comparison of quinoline metal chelates slanted columnar thin films deposited at $\alpha = 80°$. 68

List of Figures

1.1 Schematic of GLAD deposition apparatus. 5

1.2 Self shadowing effect and nucleation during initial film growth. 6

1.3 Illustration of GLAD structures obtained by controlled substrate rotation: (a) slanted posts - no rotation, (b) chevrons - periodic 180° rotation, (c) helices - continuous rotation, and (d) vertical posts - fast rotation. SEM images of a SiO_2 (e) helical film and (f) vertical post film highlighting common growth defects. Images courtesy of Shufen Tsoi. 7

1.4 SEM image of (a) a tetragonal array of lithographically patterned seeds and (b) a tetragonal array of Si square spirals deposited on a seed layer. Images courtesy of Mark Summers. 8

1.5 Illustration of a carbon-carbon double bond consisting of a σ- and a π- bond. 9

1.6 Molecular structure of a (a) 8-hydroxyquinoline molecule and (b) a tris(8-hydroxyquinoline) aluminum (Alq_3) molecule. 10

1.7 Molecular structure of the meridional and facial isomers of Alq_3. 11

1.8 Illustration of the basic structure of an organic light emitting diode. 11

2.1 High vacuum thermal evaporation deposition system. 14

2.2 X-ray diffraction pattern of (a) a solid Alq_3 thin film and (b) a 4 turn Alq_3 helical thin film. 16

2.3 Examples of various Alq_3 morphologies: (a) Slanted post $\alpha = 80°$, (b) Chevron $\alpha = 80°$, (c) 5 turn helix, $\alpha = 79°$, and (d) 25 turn helix, $\alpha = 79°$. Insets are the top down images of the films. 17

2.4 Top down SEM image of a graded pitch helical thin film illustrating the hexagonal close packed arrangement in the nanostructured ordering. 18

2.5 Illustration of the initial stage of GLAD Alq_3 growth. 19

2.6 Alq_3 capping layer on top of a 2.5 turn helix. Inset shows a top down view. 19
2.7 Examples of Alq_3 morphologies: (a) a periodic bent nematic and (b) a 5 turn left-handed helical film on top of a 5 turn right-handed helical film. . . 20
2.8 Examples of Alq_3 helices with pitches of (a) 1120 nm, (b) 140 nm, (c) 70 nm, and (d) 10 nm. Insets are top down views. 22

3.1 5 turn helical films deposited at (a) α = 77° and (b) α = 80°. White horizontal lines indicate the extent of the Alq_3 wetting layer. 26
3.2 Plot of Alq_3 wetting layer thickness at various deposition angles. A linear best fit trendline has been added as a guide. 26
3.3 Illustration of a chemically functionalized surface, where R denotes the functionalization group. 28
3.4 X-ray photoelectron scan of Si substrates functionalized with (a) propyl-trichlorosilane and (b) hexyl-trichlorosilane. 31
3.5 X-ray photoelectron scan of Si substrates functionalized with (a) octadecyl-trichlorosilane and (b) trifluoropropyl-trichlorosilane. 32
3.6 Illustration of the contact angle of a liquid on a solid surface. 33
3.7 SEM images of helices at deposited at 1 Å/s (A, B, C) and 4 Å/s (D, E, F). Images consist of Alq_3 deposited on (A, D) bare silicon substrates, (B, E) hexyl-trichlorosilane functionalized substrates, and (C, F) octadecyltrichlorosilane functionalized substrates. White horizontal lines indicate the extent of the Alq_3 wetting layer. 34
3.8 Wetting layer thickness of Alq_3 deposited at 76° varies with respect to deposition rate, 4 Å/s (○) and 1 Å/s (▲), and the surface hydrophobicity of substrates as measured by advancing aqueous contact angle. 35

4.1 Illustration of a biaxial media. 38
4.2 SEM image of silica slanted columnar thin film deposited at α = 88° as viewed along the direction of the columns. The white arrow indicates the direction of the incoming vapour flux. Broadening occurs for individual columns while growth competition is observed as smaller diameter columns are visible in the background. 40

4.3 Illustration of the 1-D shadowing that occurs during tilted columnar thin film growth that causes column broadening. 40
4.4 Illustration of the competing effects that modify the biaxial properties in a slanted columnar thin film where (a) is a view perpendicular to the deposition plane showing the primary anisotropy caused by the column tilt and (b) is a view along the deposition plane showing the secondary anisotropy caused by column broadening. 41
4.5 Illustration of the indices of refraction in tilted, columnar thin films grown by GLAD. The wetting layer is a feature observed only in organic GLAD films. 41
4.6 Cross sectional SEM images of tilted columnar thin films deposited at a) α = 71° and b) α = 85°. 45
4.7 Chart outlining the optical modelling process for solid and slanted columnar Alq_3 thin films. 46
4.8 Example of model fitting in a solid Alq_3 film (a) before the fitting process and (b) after the fitting process. Only data for the 60° angle of incidence is shown for simplification. 47
4.9 Measured real and imaginary parts of the index of refraction of Alq_3. 49
4.10 Illustration of the general Bruggeman effective medium approximation with two spherical inclusions embedded into the effective medium. 51
4.11 Illustration of the Bruggeman effective medium approximation for two elliptical inclusions embedded into the effective medium. 52
4.12 Multilayer model of columnar thin film deposited at α = 71°. 52
4.13 Measured real and imaginary parts of the principle indices of refraction of the Alq_3 columnar thin film deposited at α = 71°. 53
4.14 SEM measured and BEMA model column tilt as a function of the deposition angle α. The error bars for the SEM measurements represent one standard deviation of β for each deposition angle. Column tilt value predicted by Tait's rule (solid line) is shown as a guide. 55

4.15 Normalized film density of the biaxial layer as a function of the deposition angle α. The density predicted based on Tait's rule (solid line) is shown as a guideline. 56
4.16 The principal indices of refraction for the biaxial layer of Alq_3 at a wavelength of 525 nm. 57
4.17 In-plane birefringence, Δn, shown as a function of deposition angle α. . . . 59
4.18 SEM of the film deposited at $\alpha = 85°$ as viewed along the direction of the columns. The white arrow indicates the direction of the incoming vapour flux. As can be seen, the column cross-sections are predominantly circular in shape. 60
4.19 Illustration of the change in the major elliptical cross-section diameter as the column tilt is increased. The minor elliptical cross-section diameter is equal to the columnar post diameter and thus remains unchanged as the column tilt varies. 60
4.20 SEM of the film deposited at $\alpha = 67°$ along the direction of the post growth. The white arrow indicates the direction of the incoming vapour flux. Individual columns have merged together modifying the cross-section of the columns and decreasing the number of voids. 61
4.21 Plot of the peak selective transmittance of circularly polarized light from 5 turn helical films and the birefringence squared (Δn^2) of slanted post films at various deposition angles. 61

5.1 Molecular structure of a (a) tris(8-hydroyquinoline) gallium (Gaq_3) molecule and (b) a bis(8-hydroyquinoline) zinc (Znq_2) molecule. 64
5.2 Measured real and imaginary parts of the index of refraction of Znq_2, Gaq_3, and Alq_3. 66
5.3 Slanted post columnar thin films deposited at $\alpha = 80°$ composed of (a) Alq_3, (b) Gaq_3, and (c) Znq_2. Insets are top down views. 67
5.4 5 turn right-handed helical thin films deposited at $\alpha = 80°$ composed of (a) Alq_3, (b) Gaq_3, and (c) Znq_2. Insets are top down views. 69

5.5 Transmission through a 5 turn, right-handed helical GLAD Film deposited $\alpha = 80°$ composed of (a) Alq_3, (b) Gaq_3, and (c) Znq_2. 70
5.6 Examples of Znq_2 helices with pitches of (a) 30 nm and (b) 90 nm. Insets are top down views. 71

List of Symbols

α	Flux incidence angle measured from the substrate normal
β	Column tilt angle of the thin film
γ_{sv}	Solid-vapour surface tension
γ_{lv}	Liquid-vapour surface tension
γ_{sl}	Solid-liquid surface tension
Δ	Ellipsometric parameter measuring the relative phase change
Δn	In-plane birefringence
ϵ	Dielectric constants for the effective medium
ϵ_{mat}	Dielectric constant for the material
ϵ_{void}	Dielectric constant for the void (air)
ζ	Column orientation with respect to lab coordinate system
η	Volume fraction
θ	Advancing contact angle
λ	Wavelength of light
ν	Phase velocity of light
ρ	Thin film density
ϕ	Substrate rotation measured about the axis normal to the substrate and passing through its centre

Φ	Spectrometer work function
Ψ	Ellipsometric parameter measuring the relative amplitude change
ω	Euler angle (synonymous with β)
c	Speed of light
E_{BE}	Binding energy of the electron in the atom
E_{KE}	Kinetic energy of the emitted photoelectron
$h\nu$	Photon energy of x-ray source
k	Imaginary component of the index of refraction
n	Real component of the index of refraction
n_{avg}	Average index of refraction of the medium
n_e	Ordinary index of refraction
n_o	Extraordinary index of refraction
n_x	Index of refraction in the substrate plane perpendicular to the deposition plane
n_y	Index of refraction in the deposition plane and perpendicular to the column posts
n_z	Index of refraction aligned in the direction of the posts
n_p	Index of refraction in the deposition plane parallel to the substrate
p	Helical pitch
q_x	Depolarization factors for the x principal index
q_y	Depolarization factors for the y principal index
q_z	Depolarization factors for the z principal index

r_p	Fresnel reflection coefficients in the plane of incidence
r_s	Fresnel reflection coefficients perpendicular to the plane of incidence
T_{LCP}	Transmission of left-handed circularly polarized light
T_{RCP}	Transmission of right-handed circularly polarized light

List of Abbreviations

AFM	Atomic force microscope
Alq_3	Tris(8-hydroxyquinoline) aluminum
BEMA	Bruggeman effective medium approximation
Gaq_3	Tris(8-hydroxyquinoline) gallium
GLAD	Glancing angle deposition
Hexyl-$SiCl_3$	Hexyl-trichlorosilane
MEMS	Microelectromechanical systems
OLED	Organic light emitting diode
OTS	Octadecyl-trichlorosilane
Propyl-$SiCl_3$	Propyl-trichlorosilane
QCM	Quartz crystal microbalance
RIE	Reactive ion etching
RMS	Root mean square
SBD	Serial bideposition
SCL	Standard confidence limit
SEM	Scanning electron microscopy

TFP-$SiCl_3$	3,3,3-trifluoropropyl-trichlorosilane
VASE	Variable angle spectroscopic ellipsometry
WLT	Wetting layer thickness
XPS	X-ray photoelectron spectroscopy
XRD	X-ray diffraction
Znq_2	Bis(8-hydroxyquinoline) zinc

Chapter 1

Introduction

1.1 Motivation

Thin films deposited at oblique deposition angles with respect to the substrate normal have long been of interest due to their structural anisotropy and ability to form porous films [1,2]. Thin films with anisotropic, nanostructured morphology possess unique optical, electrical, and magnetic properties [3–6], and are fabricated using deposition techniques such as glancing angle deposition (GLAD) [7, 8] and serial bideposition (SBD) [9, 10]. This thesis presents the investigation of the optical and structural properties of quinoline metal chelate thin films deposited by GLAD. Traditionally, organic GLAD films have consisted of polymers and were fabricated only via a multi-stage templating and inversion process [11], so the optical and structural properties of directly deposited organic GLAD films remained largely unexplored. Only recently has a small molecule organic material been used to fabricate nanostructured chiral thin films by deposition at oblique angles [12]. This has opened the door to a vast array of potential organic materials that can be used to fabricate nanostructured thin films for applications such as displays, solar cells, sensors, microelectromechanical systems (MEMS), and optical filters. The wide variety of available organic materials coupled with the ability to chemically tune the properties by modifying the molecular structure provide an enormous pool of deposition materials that can be chosen and specifically tailored for a given application. However, to effectively apply these materials in structured thin film form, the growth mechanisms and properties of the films must be understood. This work focuses on the optical and structural properties of molecules in the 8-hydroxyquinoline family of small molecule organics. The main

focus of this work describes the investigation of the material tris(8-hydroxyquinoline) aluminum (Alq_3) and expands to encompass two other quinoline metal chelates: tris(8-hydroxyquinoline) gallium (Gaq_3) and bis(8-hydroxyquinoline) zinc (Znq_2). Knowledge of the optical and structural parameters of the films is critical to designing and modeling of proposed nanostructured devices composed of these materials and provides a base with which to expand to other organic materials.

1.2 Scope

The remainder of this chapter begins with a brief introduction to thin films, the glancing angle deposition technique, and small molecule organics. Chapter 2 presents an overview of the nanostructured tris(8-hydroxyquinoline) aluminum (Alq_3) morphologies that can be fabricated using GLAD. The advantages and limitations of this organic material are discussed. Chapter 3 focuses on the unique solid thin film of organic material that is deposited onto the substrate prior to nanostructured Alq_3 thin film growth. Since this phenomenon is not typically observed in inorganic GLAD thin films, it warrants special attention and the chapter discusses the effects of surface energy and deposition conditions on the thickness of this wetting layer. In Chapter 4, the optical and structural properties of a series of slanted post columnar thin films deposited at various angles are discussed and the origin of the negative in-plane birefringence is explained. Chapter 5 compares and contrasts the properties of other quinoline metal chelates to Alq_3. Chapter 6 concludes with a summary of this work and suggestions for future experiments.

1.3 Thin films

Thin film technology has matured greatly over the past century and nowadays thin films are incorporated into numerous aspects of everyday life. Thin films are found in products ranging from potato chip bags, to protective coatings on glasses, displays, and computer chips to more specialized applications such as optical filters and sensors. While the exact definition of what constitutes a "thin" film varies, the general consensus is that a thin film of a material exhibits properties different from those observed for the bulk material. Thin films typically range from several nanometres to tens of micrometres in thickness. Numerous

methods exist to fabricate thin films including chemical techniques, such as self-assembly and chemical vapor deposition, and physical vapor deposition (PVD) methods such as evaporation and sputtering. For a review of thin film fabrication techniques, the reader is directed to reference [13]. PVD is the most widely used method for depositing a thin film since it is a relatively simple technique that can be employed on a wide selection of materials including metals, semiconductors, insulators, and organics. Evaporation in particular is of interest since there is a high degree of collimation of the source material flux during deposition.

1.4 Growth mechanics of evaporated thin films

In evaporation, a source material is placed within a chamber which is pumped down to high vacuum conditions (typically $< 1 \times 10^{-2}$ Pa) to increase the mean free path of the vapor flux by reducing the amount of scattering. The source material is heated, usually by resistive heating or by an electron beam, to the point where the material sublimates or evaporates, depending on the material. Deposition of the material occurs when the vapour pressure of the source material increases as it is heated and becomes higher than the surrounding vacuum pressure in the deposition chamber [14]. A standard thin film is deposited such that the incoming vapor flux arrives relatively perpendicular to the substrate surface. The initial growth and morphology of PVD thin films composed of inorganic materials have been studied in depth and were described in different structure zone models based on the deposition conditions, such as the deposition pressure and the temperature [13, 15–18]. These models take into account the shadowing, surface diffusion, bulk diffusion, and desorption that deposited flux atoms undergo before reaching an equilibrium position on the surface. Atoms impinging onto the substrate surface typically either adsorb to the film surface, referred to as adatoms, or bounce off back into the vacuum chamber. The energy of the incoming vapour atoms is larger than the energy of the adatoms already deposited. This excess energy is transferred to the film surface through surface diffusion whereby the adatom migrates a short distance before reaching an equilibrium with the film surface [19]. The adatoms migrate over the film surface by a hopping mechanism and can potentially re-evaporate off the surface if they are not buried under the incoming atoms or

trapped by chemisorption. At lower substrate temperatures, the atoms are in a low mobility regime and self shadowing effects are dominant over surface diffusion. Shadowing occurs from the geometric constraint imposed by the surface roughness of the growing film and the line-of-sight impingement of arriving atoms. In this regime, thin films with a dense columnar morphology can be be fabricated at normal angles of incidence. By depositing at oblique angles of incidence, an additional dimension of control over the film morphology is achieved and highly porous nanostructured thin films can be fabricated using GLAD.

1.5 Glancing angle deposition

1.5.1 Background

GLAD is an oblique angle physical vapor deposition technique, developed at the University of Alberta, that enables precision nanostructured thin film features to be fabricated in a single step by utilizing oblique angles of incidence in conjunction with computer controlled substrate rotation and real time flux measurement. Fig. 1.1 shows a schematic of a GLAD apparatus. Typically, deposition angles of incidence $\alpha > 75°$ are used to enhance the self-shadowing effects of the atoms while under a limited adatom diffusion regime during deposition (Fig. 1.2). Self-shadowing effects restrict the areas where material can be deposited limiting them to the tops and sides of the nuclei which allow for the formation of individual nanostructured columns. By varying the angle of incidence, the amount of shadowing encountered can be controlled, which in turn allows the density of the film, ρ, and the column tilt, β, of the deposited material to be tailored. Tait's rule (Eqn. 1.1 and 1.2) attempts to model these parameters using a purely geometrically derived system and confirmed them using simulation [20].

$$\beta = \alpha - sin^{-1}\left(\frac{1 - cos\alpha}{2}\right) \tag{1.1}$$

$$\rho = \frac{2cos\alpha}{1 + cos\alpha} \tag{1.2}$$

The incidence of the highly collimated flux is controlled by adjusting the substrate position to the incoming flux using stepper motors which allow a high degree of control

in the formation of the film structure. GLAD films are grown using deposition rate feedback from a quartz crystal microbalance (QCM) to control the rotation angle, ϕ, of the substrate, thus enabling the fabrication of thin films with various morphologies. Porous films with nanostructures such as slanted posts, chevrons, square spirals, and graded density columns can be fabricated using this technique for applications in ultra-fast humidity sensing [21,22], thermal barrier coatings [23], 3-D photonic crystals [24,25], graded index optical filters [26,27], and anti-reflection coatings [28].

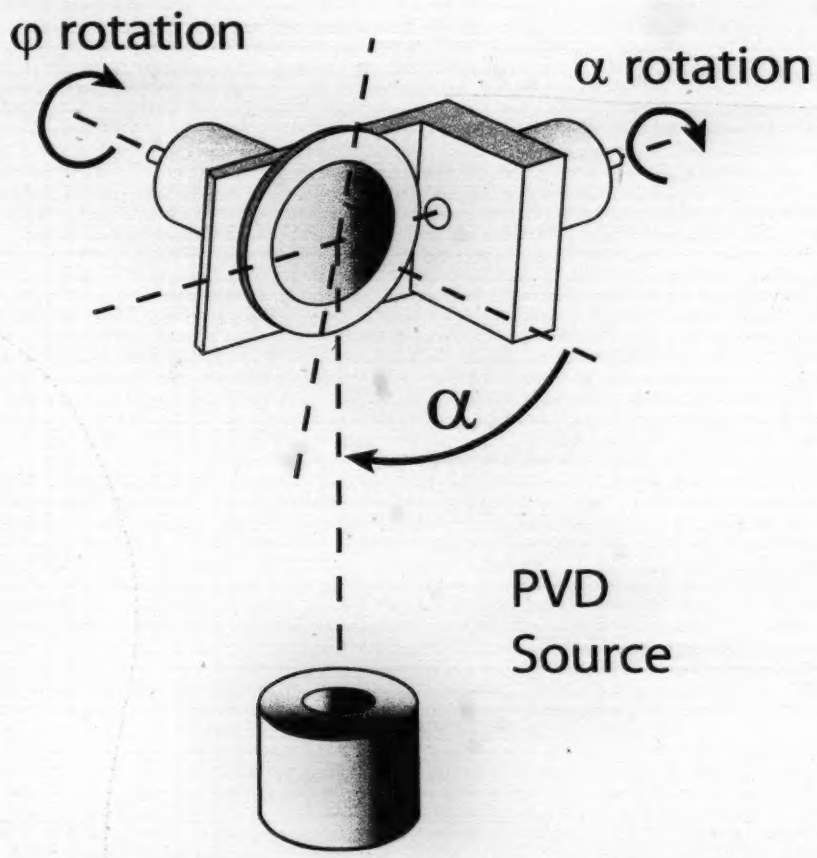

Figure 1.1: Schematic of GLAD deposition apparatus.

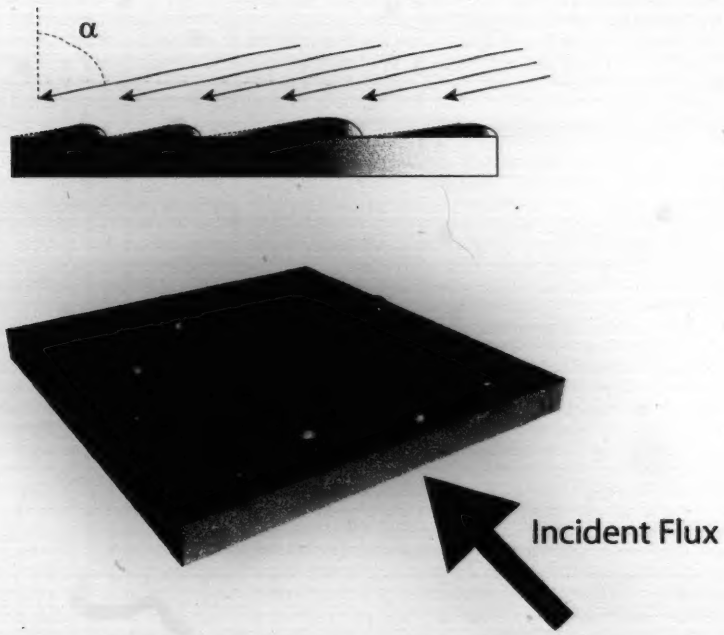

Figure 1.2: Self shadowing effect and nucleation during initial film growth.

1.5.2 Fabrication methodology of GLAD structures

GLAD nanostructures consist of individual columns which grow toward the direction of the incoming vapor flux. The most basic GLAD structure is the slanted post columnar thin film which can be fabricated by holding the substrate stationary at a constant deposition angle. By rotating the substrate abruptly by 180° at periodic intervals, chevron or zig-zag films can be grown. Helical thin films are made by depositing while the substrate is continuously rotated at a speed relative to the material deposition rate to control the pitch. Vertical posts are produced by increasing the substrate rotation to the point where the helical pitch is smaller than the column diameter. Fig. 1.3 illustrates examples of each of the above mentioned structures as well as SEM images of two of the morphologies fabricated using SiO_2. Column broadening and growth competition effects, two growth defects typically observed in inorganic GLAD films, are visible in the SEM images. More sophisticated algorithms can be used to control the substrate motion to limit such growth defects [29] and to fabricate complicated structures such as square spirals [30], s-shaped films [31], or graded index films [32].

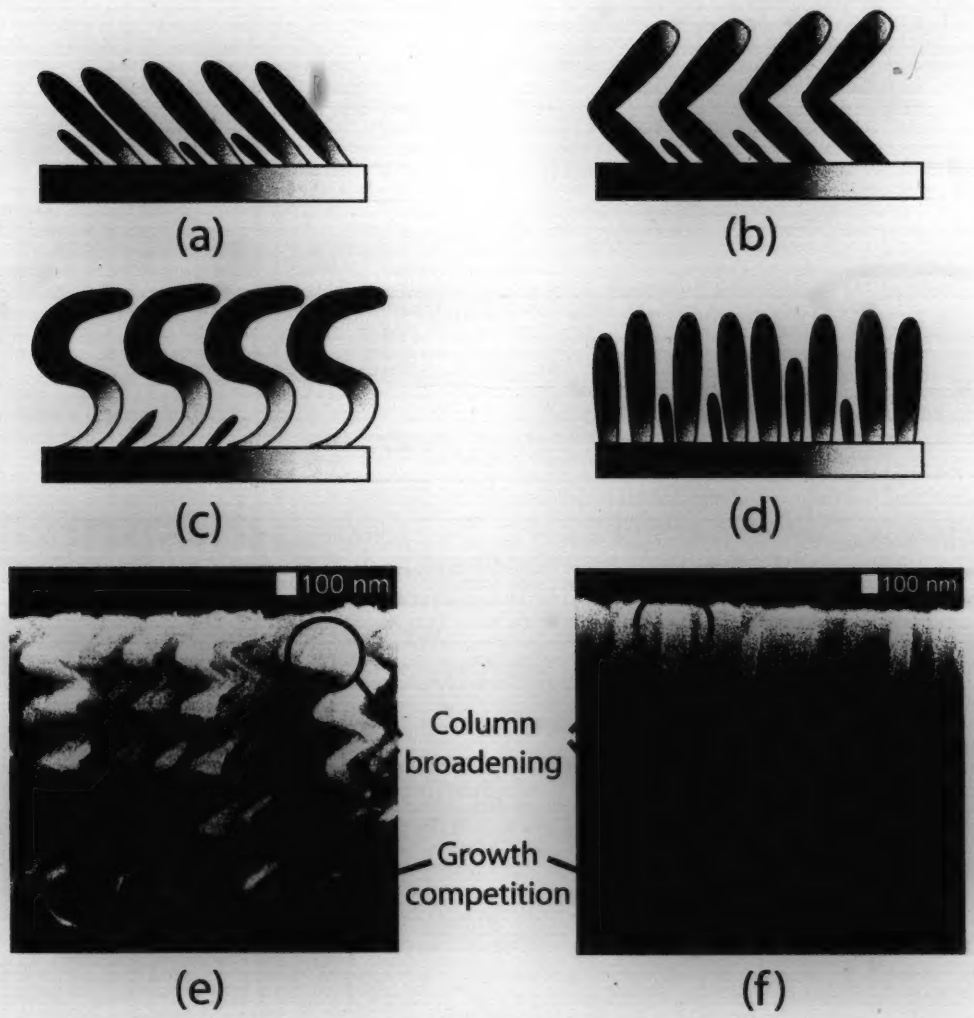

Figure 1.3: Illustration of GLAD structures obtained by controlled substrate rotation: (a) slanted posts - no rotation, (b) chevrons - periodic 180° rotation, (c) helices - continuous rotation, and (d) vertical posts - fast rotation. SEM images of a SiO_2 (e) helical film and (f) vertical post film highlighting common growth defects. Images courtesy of Shufen Tsoi.

1.5.3 Nanostructure arrangement

Normally the nanostructure arrangement in inorganic GLAD films is randomly arrayed due to the irregular pattern in the nucleation that occurs on the substrate surface. Due to self-shadowing effects, nanostructures preferentially grow at these nucleation sites, resulting in randomly arranged films. To confine growth to specified locations, substrates can be pre-patterned with a seed layer consisting of an array of relief structures that selectively shadow the substrate, forcing the material to deposit on top of the seeds and form patterned films (Fig. 1.4). A number of techniques can be used to pattern periodic arrays of sub-micron features, including laser interferometric lithography [33], embossing techniques [34], electron beam lithography [35], and conventional photolithography [24].

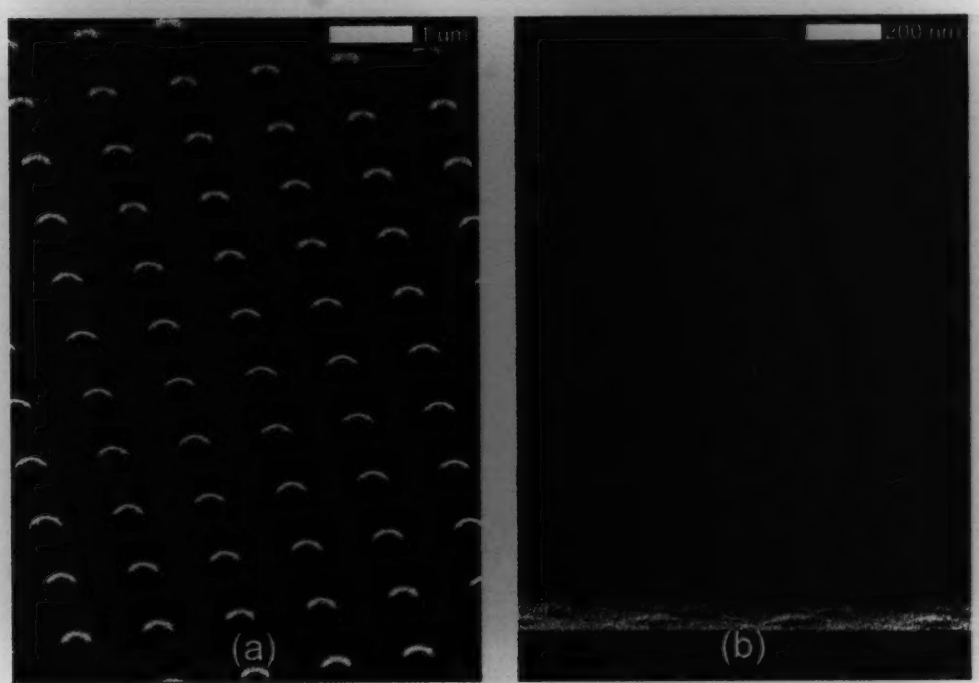

Figure 1.4: SEM image of (a) a tetragonal array of lithographically patterned seeds and (b) a tetragonal array of Si square spirals deposited on a seed layer. Images courtesy of Mark Summers.

1.6 Organics

Organics are materials that contain carbon and hydrogen (and usually other elements such as nitrogen, sulfur and oxygen) and can be found in nature or synthesized in a laboratory. Organic materials exist in a vast variety of compounds numbering in the millions in which composition control and the potential for property tuning is achieved by chemical means. Organic molecules typically have covalent bonds which mix the native atomic orbitals to form hybrid orbitals to achieve a minimum energy state. For example, the hybridization of the s, p_x, and p_y atomic orbitals in an atom results in the formation of a sp^2 hybrid orbital. These hybrid orbitals play a large role in the properties and geometric configuration of the molecule. There are two types basic types of bonds that are formed when atoms form a covalent bond: sigma (σ)- and pi (π)-bonds. A σ-bond is formed when an electron pair is shared in an area centered on a line running between the atoms. A π-bond is formed when parallel orbitals overlap and share an electron pair which occupies the space above and below a line joining the atoms (Fig. 1.5). Molecular fragments joined by a π-bond cannot rotate about that bond unless the π-bond breaks because rotation involves destroying the parallel orientation of the constituent orbitals.

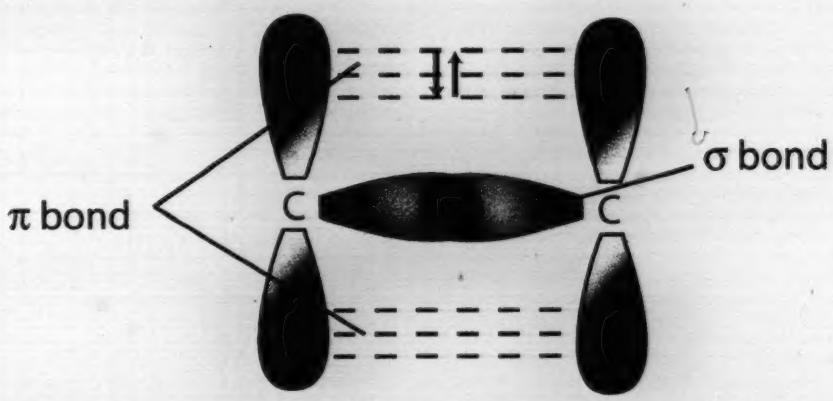

Figure 1.5: Illustration of a carbon-carbon double bond consisting of a σ- and a π- bond.

Most of the currently studied organic molecules used for photonic and electronic applications belong to the class of π-conjugated materials. Covalent σ-bonds hold the molecule together while π-electrons in π-bonds are free to move on across the molecule (conjugation). The π-electron system is responsible for most of the electronic and optical

properties. Organometallics are a category of organic compounds that contain a metal. Small molecule organometallics typically consist of a metal ion bound to a number of organic ligands to form a complex called a chelate. One of the most well known metal chelates is tris(8-hydroxyquinoline) aluminum (Alq_3), which consists of three 8-hydroxyquinoline ligands bound to a central aluminum atom (Fig. 1.6). The molecule is roughly 8 Å in diameter and has an octahedral coordination with two geometrical isomers: facial and meridional. The facial isomer has three identical ligands that are mutually cis and a meridional isomer where the three identical ligands are coplanar (Fig. 1.7).

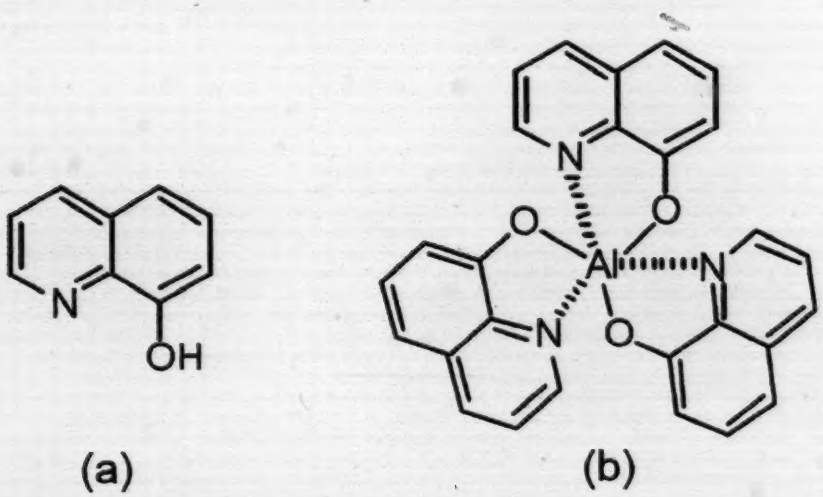

Figure 1.6: Molecular structure of a (a) 8-hydroxyquinoline molecule and (b) a tris(8-hydroxyquinoline) aluminum (Alq_3) molecule.

Since the 1950's, fluorometric determination using 8-hydroxyquinoline was used to qualitatively detect the amount of aluminum in materials including steel and paper [37,38]. Quinoline ligands chelate to a large number of metals; however, only aluminum, beryllium, gallium, indium, magnesium, and zinc form fluoroscent metal quinolates [39]. It was not until 1987, when Tang and VanSlyke first demonstrated an efficient electroluminescent device using an Alq_3 thin film, that interest in the material intensified [40]. Since then, Alq_3 has become one of the staple small molecules used in organic light emitting diodes (OLED) applications serving the dual role of electron transport layer and emission layer [41–44]. The basic OLED structure consists of three organic semiconductor layers sandwiched between two electrodes (Fig. 1.8). The first layer consists of a hole transporting material,

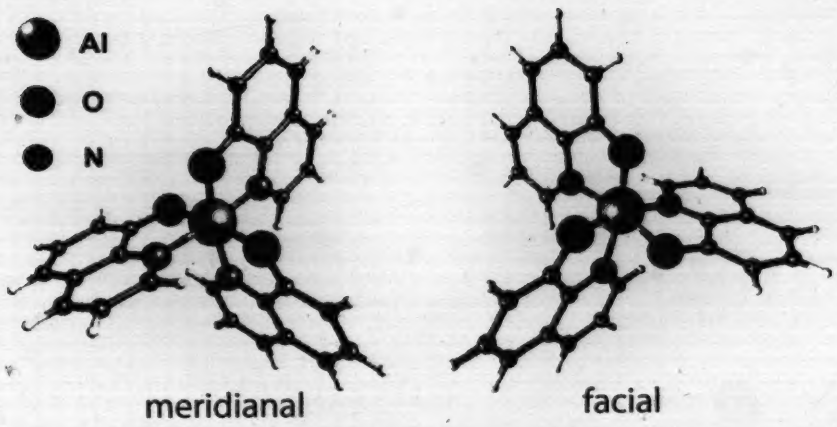

Figure 1.7: Molecular structure of the meridional and facial isomers of Alq_3. This image obtained from [36]. Copyright Wiley-VCH Verlag GmbH and Co. KGaA. Reproduced with permission.

the second layer a light emitting material, and the third layer an electron transporting material. In the case of an OLED utilizing Alq_3, the material is typically used as both the electron transport layer and the emission layer since it has a green broadband emission. The top electron-injecting electrode consists of a low work function metal or metal alloy while the bottom hole-injecting electrode consists of a thin film of transparent conducting material, commonly indium-tin oxide, in order to allow the light to pass through.

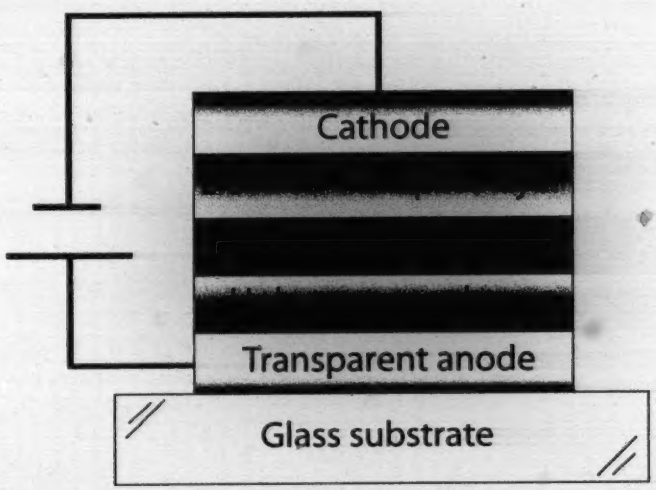

Figure 1.8: Illustration of the basic structure of an organic light emitting diode.

Alq_3 possesses many favorable characteristics including good electron mobility, high photoluminescence efficiency, a relatively high glass transition temperature of 175°C, and thermal stability at temperatures up to 350°C [45, 46]. One of the best attributes of Alq_3 is its propensity to be deposited into thin film form using vacuum deposition. In addition, the properties of the metal chelate can be also be tailored by modifying the 8-hydroxyquinoline ligand or by changing the metal center of the molecule [46–52]. Recently, studies into the properties of nanostructured Alq_3 grown using GLAD have demonstrated novel characteristics and shown potential for various applications [12,53]. In the following chapters, the investigation into the fundamental growth and optical properties of nanostructured quinoline metal chelate thin films is described.

Chapter 2

Alq_3 nanostructured thin films

While the bulk of the literature on Alq_3 has focused on the material in solid thin film form, in 2006 Hrudey *et al.* first demonstrated the potential for nanostructured Alq_3 with the fabrication of thermally evaporated helices [12, 53]. By exerting control over the orientational order of the nanostructures, films with highly uniform, self-organized arrays of submicron scale structures can be fabricated. In this chapter, the deposition system used to evaporate Alq_3 and other organic materials is introduced and a brief overview of fabricated nanostructure morphologies using the GLAD technique is presented.

2.1 Fabrication

The fabrication of organic thin films was carried out in a bell jar style high vacuum deposition system with a 24 cm throw distance shown in Fig. 2.1. The system is water cooled and uses a diffusion pump to achieve high vacuum conditions with a standard deposition base pressure of 2.6 x 10^{-4} Pa. A Kurt J. Lesker LTE21000 low temperature thermal effusion cell was used to evaporate the organic material which was contained in an alumina crucible. As-supplied Alq_3 powder purchased from Gelest Inc. (nominally 99+% pure) was placed in the crucible and heated to 150°C for several hours under rough vacuum prior to deposition, to remove water vapour and potential solvents. Alq_3 films were then deposited by thermal evaporation of the heat treated source material under high vacuum ($< 2.6 \times 10^{-4}$ Pa) at temperatures ranging from 260°C - 300°C. The morphology of the GLAD films were determined using mathematical functions for the substrate motion which were implemented using software written using the LabVIEW visual programming

language [54]. The deposition rate was monitored using a quartz crystal microbalance (QCM) and was used as feedback for the computer control software in order to control the rotation of the substrate chuck. Calibration films composed of helices were deposited at angles between 65° - 88° to determine the vertical growth ratios for Alq_3 GLAD films, which were used to control the film thickness in subsequent depositions.

Figure 2.1: High vacuum thermal evaporation deposition system.

2.2 Alq_3 morphologies

Alq_3 thin films of various morpholgies were deposited using GLAD and the resulting structures were imaged by scanning electron microscopy (SEM) using a JEOL6301F field-

emission scanning electron miroscope with a 5 kV acceleration voltage. The generally amorphous nature of the sublimed Alq_3 was confirmed on a solid film and a 4 turn helical film using X-ray diffraction (Fig 2.2). The films did not exhibit the numerous X-ray diffraction peaks at various scattering angles typically observed in polycrystalline Alq_3 [44, 55, 56]. Examples of slanted post, chevron, and helical thin films fabricated using GLAD are shown in Fig. 2.3. Analysis of sample images have revealed a number of intriguing differences between the structures produced using organic Alq_3 compared to typical GLAD films grown using inorganic materials. The Alq_3 structures have a much smoother surface and the column diameters are more uniform throughout the film, both when comparing neighboring columns and when comparing different points within the same column. The diameter for the individual structures was observed to be $\sim$75 nm throughout the thickness of various Alq_3 films, the thickest of which was a 14 micron thick, 40 turn helical film. Furthermore, the Alq_3 films seemed to exhibit much less bifurcation and column extinction than inorganic GLAD films.

In addition to the minimal deleterious effects observed in Alq_3 GLAD films, a remarkable near hexagonal close packed arrangement of the helices in chiral films has also been observed [12]. This ordering can be clearly seen from the top down SEM image of a graded pitch helical film shown in Fig. 2.4. While the cause of this ordering is still unknown, it is presumed to be a result of a combination of diffusive interactions between the Alq_3 molecules arriving at the substrate. Studies into the nucleation of initial growth of Alq_3 on apolar substrates by Brinkmann *et al.* have demonstrated a similar nearly hexagonal array of domains due to a combination of the narrow distribution of the nucleation size and narrow inter-nuclei distance [57, 58]. The ordering on the apolar substrates was due to the absence of coarsening phenomena and secondary nucleation during growth. This limited the initial domain size to a narrow distribution by causing the centres of mass to migrate to empty regions of the substrate which resulted in a preferred nearest neighbor distance.

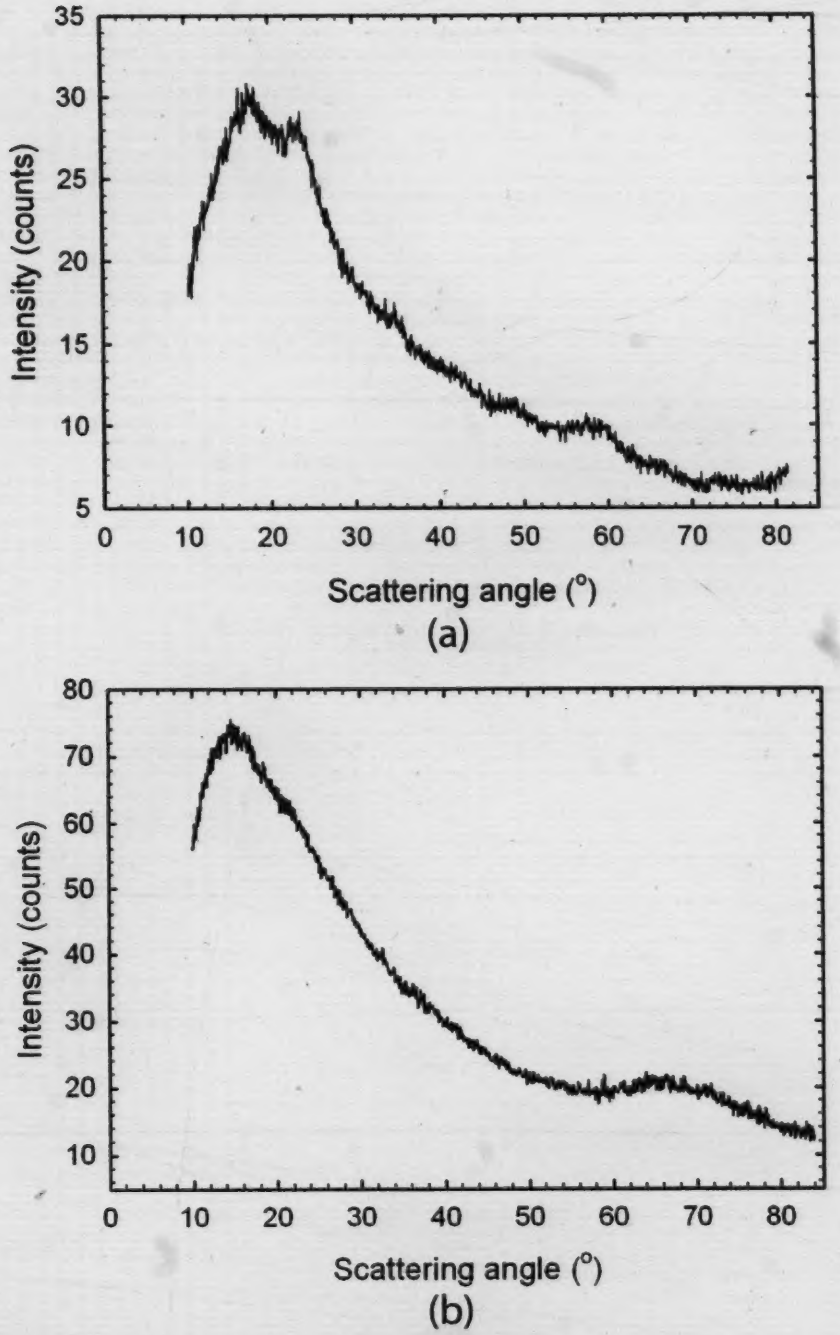

Figure 2.2: X-ray diffraction pattern of (a) a solid Alq_3 thin film and (b) a 4 turn Alq_3 helical thin film.

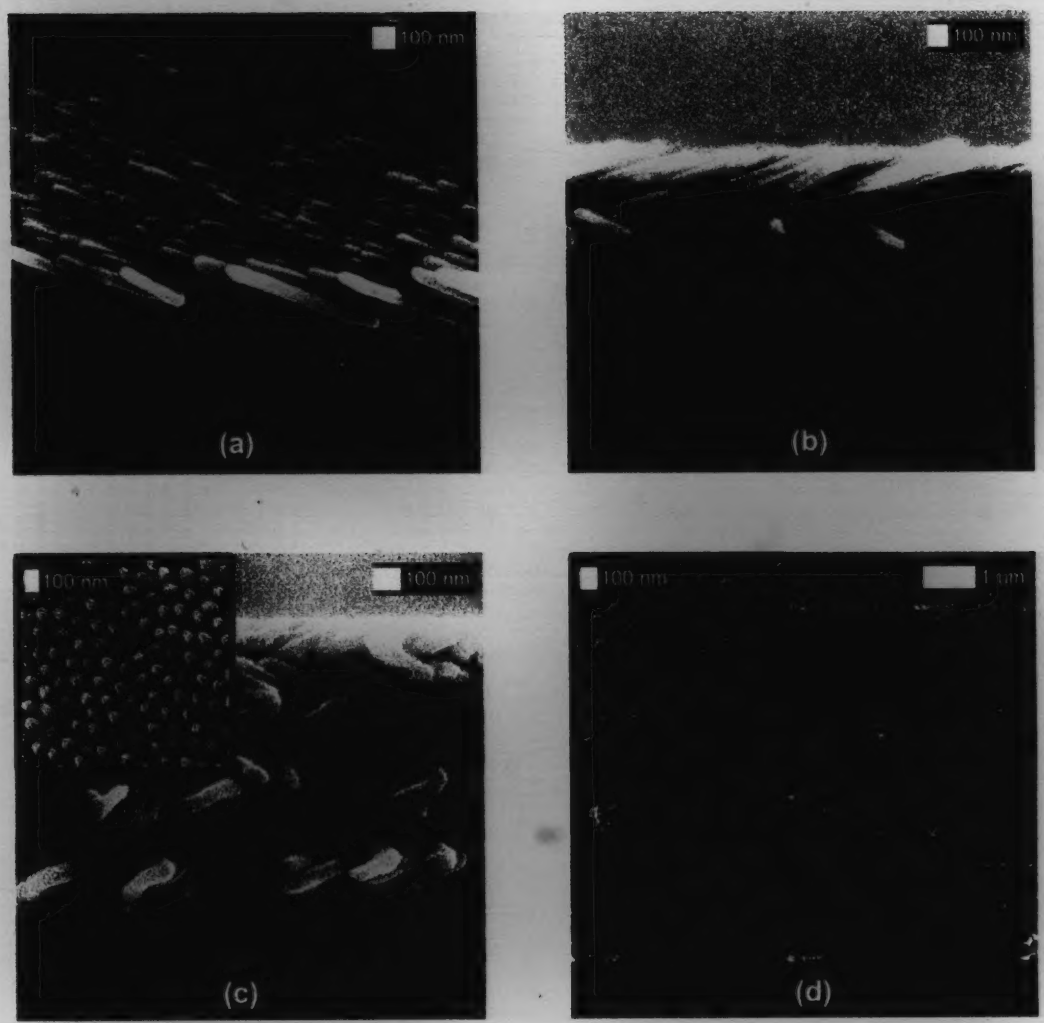

Figure 2.3: Examples of various Alq_3 morphologies: (a) Slanted post $\alpha = 80°$, (b) Chevron $\alpha = 80°$, (c) 5 turn helix, $\alpha = 79°$, and (d) 25 turn helix, $\alpha = 79°$. Insets are the top down images of the films.

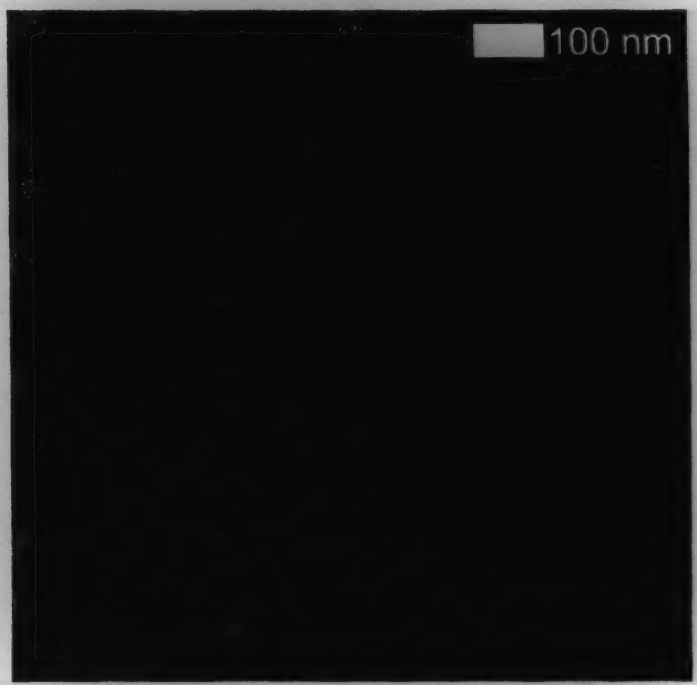

Figure 2.4: Top down SEM image of a graded pitch helical thin film illustrating the hexagonal close packed arrangement in the nanostructured ordering.

During the formation of the GLAD structure deposited onto as-supplied silicon substrates, Alq_3 molecules impinging on the substrate surface tend to form nuclei with large surface-to-volume ratios. This is due to the large interfacial energy mismatch between Alq_3 and the silicon substrate [59], which has a polar native oxide layer on the surface. Since adsorbed molecules tend to migrate to local energy minima, the large surface-to-volume ratio nuclei will coalesce to form larger islands with smaller surface-to-volume ratios, thus lowering interfacial energy [57, 58]. GLAD nanostructures can only be formed when self-shadowing dominates over the mobility of adsorbed molecules. The formation of a wetting layer prior to the growth of the Alq_3 nanostructures indicates that this condition is not met in the initial stages of Alq_3 growth. However, after wetting layer formation, the film enters a partial wetting regime where the extreme self-shadowing of GLAD overcomes molecular mobility resulting in the growth of nanostructures (Fig. 2.5).

Figure 2.5: Illustration of the initial stage of GLAD Alq_3 growth.

Several other Alq_3 morphologies have been fabricated to investigate the structure of the films. Capping layers of Alq_3 have been grown on top of GLAD films to create a solid interface for the deposition of additional thin films on top for device architectures requiring conductive layers (Fig. 2.6). Other examples of thin film morphologies grown include films deposited using periodically bent nematic growth algorithms and a left-handed helical film on top of a right-handed helical film (Fig. 2.7). All of the fabricated films exhibited the characteristic smoothness of individual structures as observed in the SEM images.

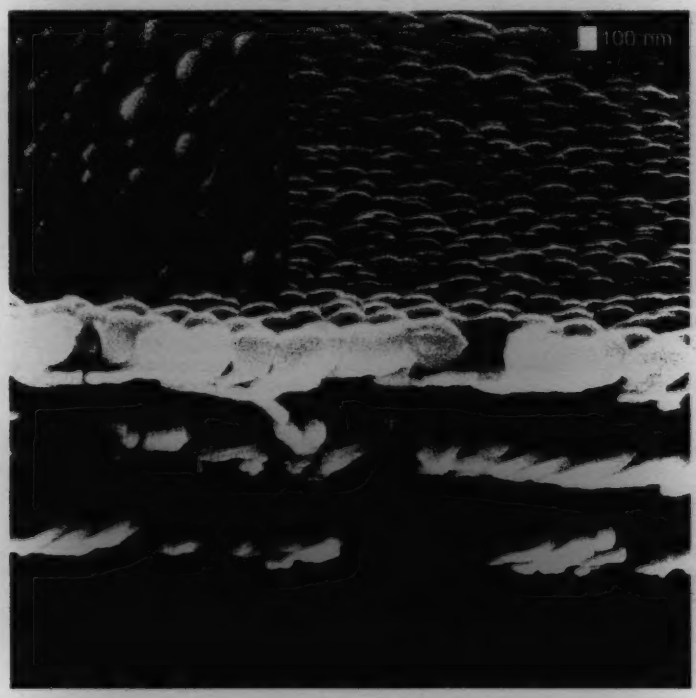

Figure 2.6: Alq_3 capping layer on top of a 2.5 turn helix. Inset shows a top down view.

Attempts to fabricate vertical posts were unsuccessful using the traditional GLAD

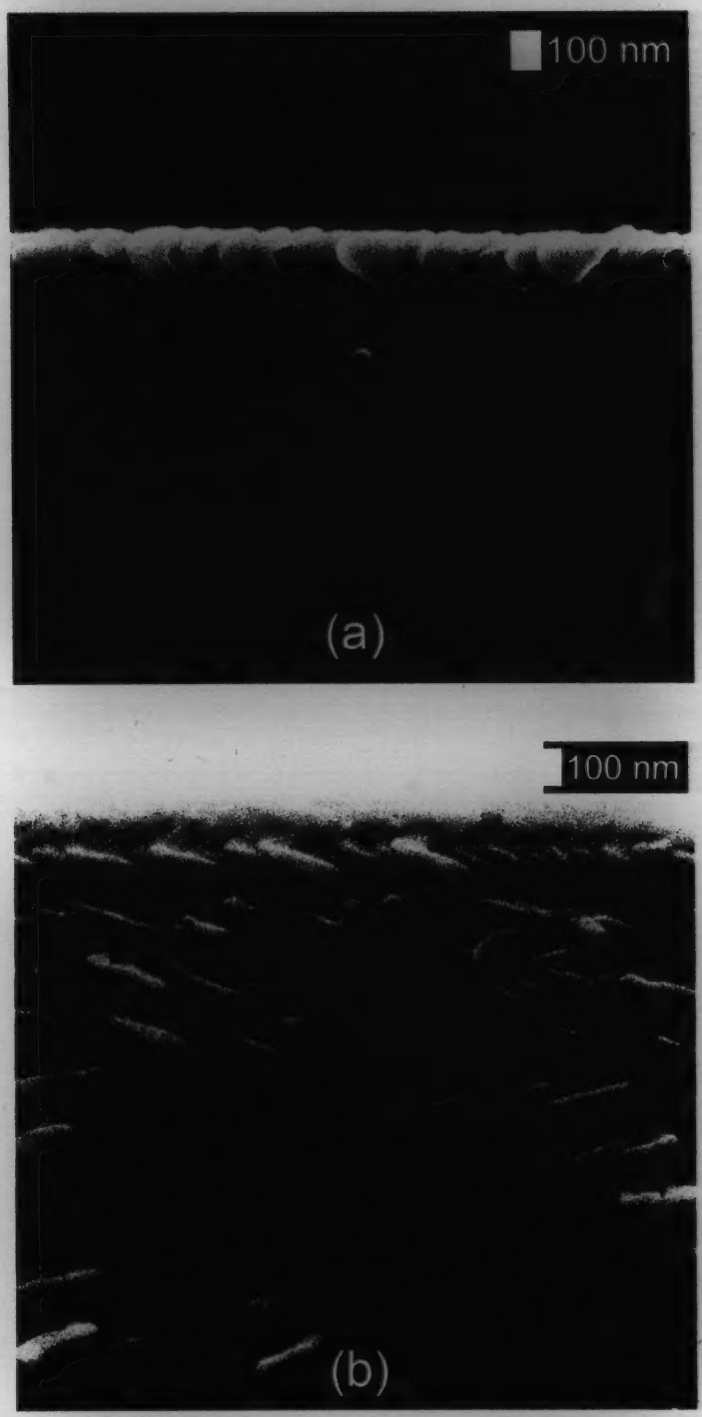

Figure 2.7: Examples of Alq_3 morphologies: (a) a periodic bent nematic and (b) a 5 turn left-handed helical film on top of a 5 turn right-handed helical film.

method of rapid rotation of the substrate about the ϕ axis, such that the helical pitch would be less than the column diameter. Examples of several vertical post attempts at varying rotation speeds fabricated by Graeme Dice are shown in Fig. 2.8. The films were fabricated using a multiple rotation chuck which allowed helical films with various pitches to be deposited in the same run. It appears that contrary to the typical behavior of inorganic vertical posts, the Alq_3 tends to grow in clusters under the high rotation regime (low helical pitch) where the pitch is comparable to the column diameter. At higher helical pitches, achieved by decreasing the substrate rotation, the individual nanostructures resemble slanted posts. As the rotation rate increases the structure gradually changes as the individual helices become defined. Based upon the SEM images of films deposited at 70 nm and 140 nm pitch, the Alq_3 transitions between the standard structured helical thin film into the clustered globular morphology between these pitches. At lower rotation speeds, the incoming molecules are constantly depositing onto the same surface of the nanostructure and thus growing in the direction of the incoming vapor flux. At high rotation speeds, the molecules impinge on the nanostructure from generally all directions. Since the distance the molecules are able to diffuse is limited by the low mobility and burial by the incoming flux, localized individual clusters grow in multiple locations on the nanostructure.

The Alq_3 films all had an initial solid layer of Alq_3 present before the porous GLAD structure began to grow, regardless of the structural morphology. This wetting layer phenomenon is discussed in further detail in the next chapter.

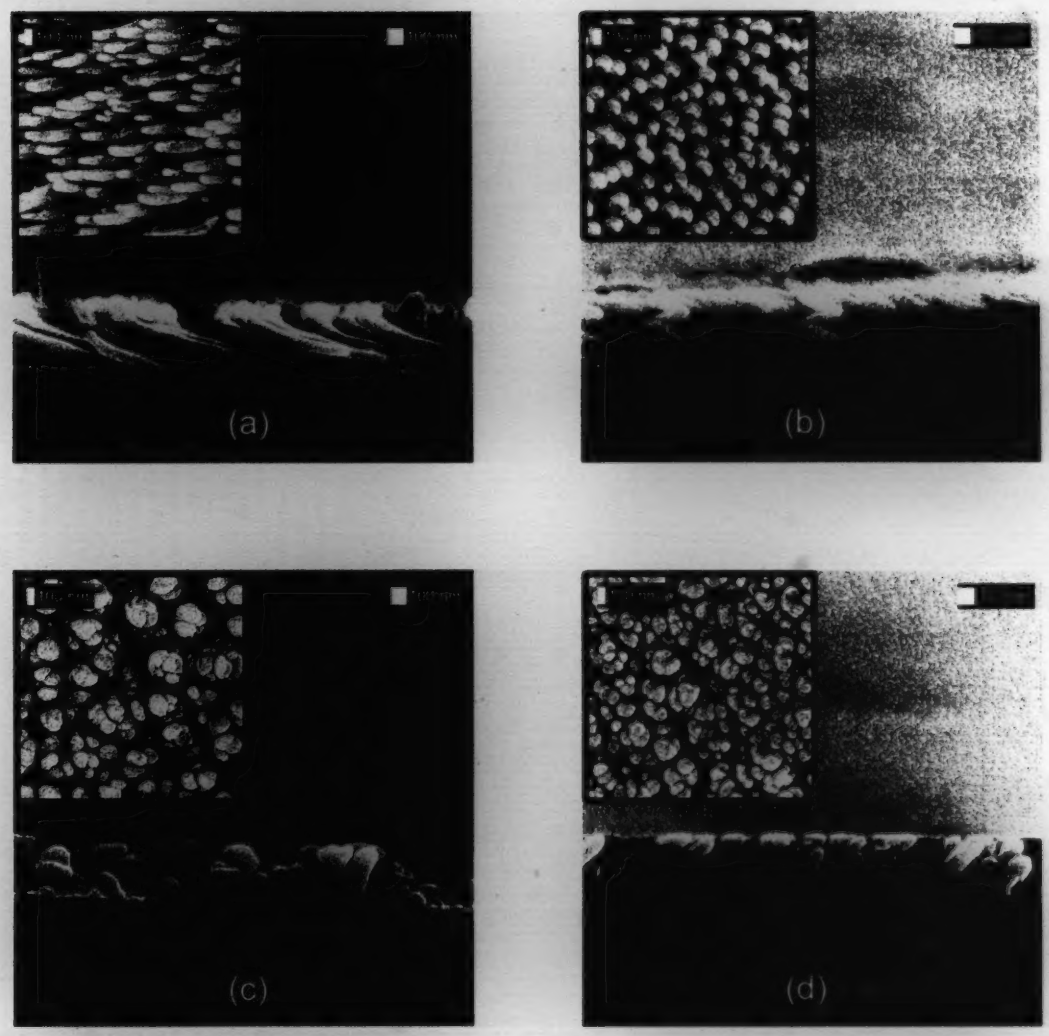

Figure 2.8: Examples of Alq_3 helices with pitches of (a) 1120 nm, (b) 140 nm, (c) 70 nm, and (d) 10 nm. Insets are top down views.

2.3 Summary

Alq_3 thin films of various morphologies have been fabricated and examined using SEM. The Alq_3 forms smooth nanostructures which generally do not appear to suffer the common defects such as column broadening and bifurcation typically observed in inorganic materials. Most common GLAD structures can be fabricated except for vertical posts. Attempts to fabricate the vertical post by rapid substrate rotation did not result in the standard pillar formation. Another unusual phenomenon observed was the formation of a solid layer of Alq_3 prior to the nanostructure formation regardless of morphology. This layer is not seen in inorganic films.

Chapter 3

Control of wetting layer thickness[1]

The ability to tailor the morphology of nanostructured thin films is one of the main advantages of the GLAD technique. While the use of GLAD to control the formation of various individual organic nanostructures has been demonstrated in the previous chapter, also observed was the presence of an initial thin solid layer of Alq_3 which formed prior to the Alq_3 columnar nanostructures. This initial formation has never been observed for inorganic films produced using the GLAD technique and limits the potential for applications where arrays of nanostructures are addressed [60] or when depositing on pre-patterned seeded substrates is required [24, 25]. In this chapter, various methods to control the thickness of the wetting layer are investigated. For the work described in this chapter, my contributions included the deposition of the Alq_3 thin films, characterization and analysis of the wetting layer thickness, and measurment of the contact angles of functionalized substrates.

3.1 Wetting layer vs deposition angle

During the investigation of the chiral optical properties of Alq_3, 5 turn helical thin films were fabricated at varying angles angles of deposition ranging from 75° - 85° [53]. SEM analysis of the films was performed using the public domain, Java-based image processing program ImageJ [61]. ImageJ was inspired by the NIH Image program for the Macintosh computer and is capable of spatial calibrations to provide real world dimensional

[1] A version of this chapter has been published and is reproduced with permission from: S. Tsoi, B. Szeto, M. D. Fleischauer, J. G. C. Veinot, and M. J. Brett, "Control of Alq_3 wetting layer thickness via substrate surface functionalization," *Langmuir*, vol. 23, no. 12, pp. 6498-6500, 2007. Copyright 2007 American Chemical Society.

measurements in units such as nanometres. The software can calculate area and pixel value statistics of user defined selections and measure distances and angles. The thickness of the wetting layer was measured from SEM images using the ImageJ software rectangular selection tool. The bottom of the rectangle was lined up to the silicon substrate-wetting layer interface while the top of the rectangle was placed at the wetting layer-nanostructure interface. The position of the wetting layer-nanostructure interface was defined as the film thickness beyond which the solid Alq_3 began to exhibit any porous columnar growth. The height of the rectangle was converted from the pixel measurement of the image to nanometres based on the magnification of the SEM image. ± 8 nm error bars were included to account for the resolution of the SEM images and the difficulty in determining the exact location where the wetting layer stopped and nanostructured growth began which varied slightly across each sample. The analysis of SEM images revealed a variation of the wetting layer thickness as the deposition angle changed, as seen in Fig. 3.1. A plot (Fig. 3.2) of the measured wetting layer thickness as a function of deposition angle shows a general decreasing trend in wetting layer thickness as the deposition angle was increased. The thickness decreased linearly with the deposition angle and a maximum wetting layer thickness of 150 nm was measured at $\alpha = 75°$ and minimum thickness of 29 nm was measured at $\alpha = 85°$. Self-shadowing and the tendency to columnar growth is more extreme at higher angles and better able to overcome the wetting regime.

To further understand the parameters affecting the wetting layer formation, substrates with chemically functionalized surfaces were fabricated and deposited onto at different deposition rates. This results are discussed in further detail in the next two sections.

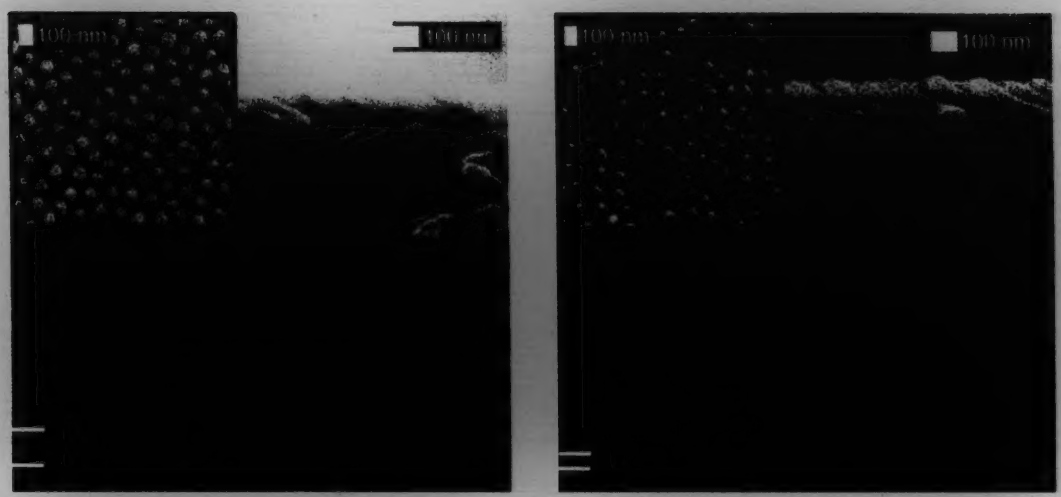

Figure 3.1: 5 turn helical films deposited at (a) $\alpha = 77°$ and (b) $\alpha = 80°$. White horizontal lines indicate the extent of the Alq_3 wetting layer.

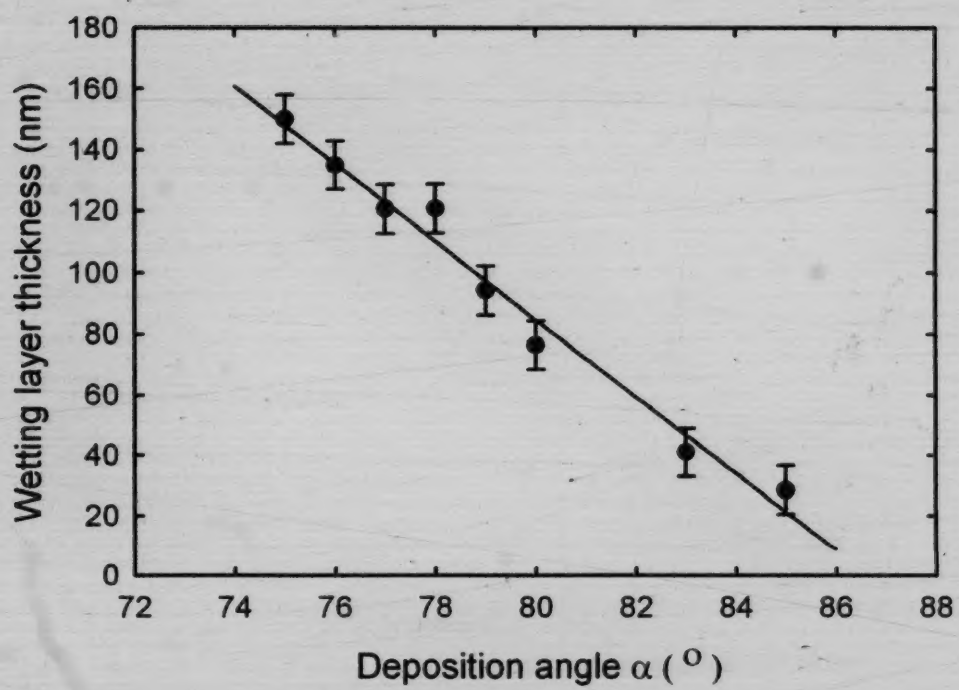

Figure 3.2: Plot of Alq_3 wetting layer thickness at various deposition angles. A linear best fit trendline has been added as a guide.

3.2 Functionalization of substrate surface

It has been previously shown that the combination of straightforward siloxane-based surface functionalization and SiO_2-GLAD films allowed for the exploitation of the synergistic effects of the film morphology and surface chemistry and provided hydrophobic and superhydrophobic surfaces [62]. Furthermore, surface modification of OLED anode surface chemistry has also been shown to increase OLED thermal stability via moderation of surface energy mismatch of hydrophilic ITO and hydrophobic hole transport materials [63, 64]. In this study, surface functionalization was used to investigate the impact of the interfacial energy mismatch between the substrate and Alq_3 wetting layer.

3.2.1 Substrate preparation

In preparation for the chemical functionalization, the substrates were cleaned and treated with an oxygen plasma. Silicon substrates were cleaned using a piranha solution (3:1 vol.:vol. H_2SO_4:H_2O_2) and baked at 130°C in a vacuum of 11.18 kPa in order to limit water vapor adsorption. Afterwards, the substrates were treated for 90 seconds with oxygen plasma reactive ion etching (RIE) using the NanoFab Trion Phantom II RIE. This technique is known to saturate the Si surface with hydroxyl moieties and hence maximizes reactivity between the substrates and the trichlorosilane reagents [62, 63]. Following standard Schlenk line protocol, all RIE treated substrates were immersed in a dry, de-oxygenated 20 mM toluene solution of various alkyltrichlorosilanes supplied by Aldrich Chemical. The substrates submerged in propyl-trichlorosilane (propyl-$SiCl_3$), hexyl-trichlorosilane (hexyl-$SiCl_3$), octadecyl-trichlorosilane (OTS), and 3,3,3-trifluoropropyl-trichlorosilane (TFP-$SiCl_3$) solutions were allowed to react for 2 hours under argon atmosphere. The alkyltrichlorosilane reaction solution was removed and the substrates were rinsed 3 times with dry toluene and finally acetone to hydrolyze any residual Si-Cl functionalities. Substrates were finally annealed in air for 12 h at 150°C. Fig. 3.3 illustrates the surface of the substrate after chemical functionalization.

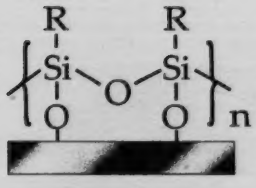

	R =
TFP-$SiCl_3$	$C_3F_3H_4$
Propyl-$SiCl_3$	C_3H_7
Hexyl-$SiCl_3$	C_6H_{13}
OTS	$C_{18}H_{37}$

Figure 3.3: Illustration of a chemically functionalized surface, where R denotes the functionalization group.

3.2.2 Characterization of functionalized substrates

The atomic force microscope (AFM) is a type of scanning probe microscope capable of topographical imaging with sub-nanometre resolution. In atomic force microscopy, a probe consisting of a microscale cantilever with a sharp tip at the end is scanned over the sample surface. The interaction force between the probe tip and the surface causes a deflection of the probe that obeys Hooke's Law for small displacements. The probe tip deflection is measured using a laser spot reflected from the top of the probe into a split photodiode. A Digital Instruments NanoScope IV Multimode Atomic Force Microscope was used to scan a sample area of 5x5 μm^2 on each sample to determine the surface roughness since it has been shown that the aqueous wettability of substrates, described by Wenzel's surface wettability equation [65], is strongly related to the chemistry and roughness of substrate surfaces.

X-ray photoelectron spectroscopy (XPS) is a quantitative spectroscopic technique based on the photoelectric effect that is used in the analysis of surface composition. This technique is capable of detecting all elements at a concentration >0.1 atomic % present in a sample except for hydrogen and helium [66]. The sample is irradiated with a monochromatic beam of X-rays under high vacuum condition which induces the direct emission of photoelectrons from the surface atoms. The binding energy of photoelectrons is characteristic of the sample material and can be determined using following equation:

$$E_{BE} = h\nu - E_{KE} - \Phi \tag{3.1}$$

where E_{BE} is the binding energy of the electron in the atom, $h\nu$ is the photon energy from of the X-ray source, E_{KE} is the kinetic energy of the emitted photoelectron, and Φ is the work function of the XPS spectrometer. The mass percentage of the elements on the surface of the sample is determined by the peak intensities of the ejected photoelectrons at specific binding energies. XPS was performed on functionalized substrates using a Kratos Axis Ultra system with a Al Kα source in order to verify the presence of the surface chemistry modifications by confirming the presence of organic moieties and the absence of residual HCl byproducts which would have generated peaks at 198.6 eV for Cl (2p) or 270 eV for Cl (2s) (Fig. 3.4,3.5) [62,63].

The surface energies of the substrates both before and after the functionalization were measured using advancing contact angle measurements. Contact angle measurements are a simple method of estimating the surface energy of a material and the interfacial liquid/vapour/solid forces. The contact angle, θ, describes the shape of a liquid droplet, in our case deionized water, resting on a solid surface by defining the angle between the tangent line from the liquid droplet to the surface of the solid (Fig. 3.6). On ideal solid surface without topography, the relationship between the contact angle, solid-liquid surface tension, γ_{sl}, solid-vapour surface tension, γ_{sv}, and the liquid-vapour surface tension, γ_{lv}, is given by Young's equation:

$$\gamma_{lv}cos\theta = \gamma_{sv} - \gamma_{sl} \tag{3.2}$$

A contact angle measurement is taken by forming a drop of liquid at the tip of a syringe and carefully placing the drop onto the solid surface. In advancing contact angle measurements, the syringe is retracted and the measurement is taken soon afterwards. Advancing refers to the state of the liquid which is fully expanded and occurs right after the drop is placed. This is commonly referred to as the "wetting angle". The opposite of this is receding contact angle measurements in which the drop retains its shape while contracting due to the extraction of liquid using the syringe. Contact angle measurements fall within a range with advanced angles approaching a maximum value and receded angles approaching

a minimum value. The difference between the maximum (advancing) and minimum (receding) contact angle values is called the contact angle hysteresis and is largely due to the surface roughness which affects the wettability of the surface in conjunction with the surface energy [67]. All advancing contact angles measurements reported were averages of 3 individual measurements taken at different locations of the same substrate.

3.2.3 Control via surface functionalization and deposition rate

Two sets of 2.5 turn GLAD helical thin films were grown onto functionalized substrates at flux incidence angle of 76° under similar chamber conditions. The only variation between the two depositions was the deposition rate which was kept stable at 1 Å/s and 4 Å/s. Table 3.1 summarizes the measurements obtained from the samples.

Advancing aqueous contact angle measurements were used to characterize the surface aqueous wettability of as-supplied and treated Si substrates. As-supplied Si substrates exhibit an advancing contact angle (θ) of 20°. After RIE treatment and baking, the Si substrates showed $\theta \approx 48°$, consistent with the removal of adsorbed water vapor from the substrate surface. Upon treatment with alkyltrichlorosilane solutions, the Si substrates were rendered hydrophobic as indicated by increasing θ values (Table 3.1).

The organosiloxane derivatized substrates exhibited similar RMS surface roughness with the exception of OTS, which had a slightly smaller roughness factor. Theoretically, Hexyl-$SiCl_3$ should exhibit a higher advancing contact angle than propyl-$SiCl_3$ due to the longer hydrocarbon chain, however, the combined surface functionalization and higher surface roughness of propyl-$SiCl_3$ led to a slightly higher advancing contact angle. The TFP-$SiCl_3$ treated substrates exhibited a contact angle similar to the results reported for other fluorinated surfaces [68]. Thermally evaporated solid Alq_3 films deposited at normal incidence were measured to have a contact angle $\theta = 82°$. Clearly, there is a smaller surface energy mismatch between Alq_3 molecules and functionalized Si substrates ($\theta = 90° - 101°$) compared to as-supplied Si ($\theta = 20°$).

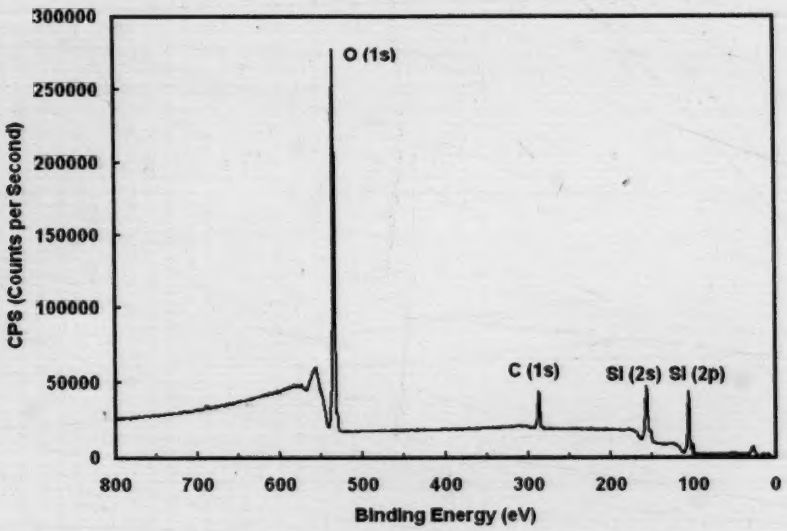

(a)

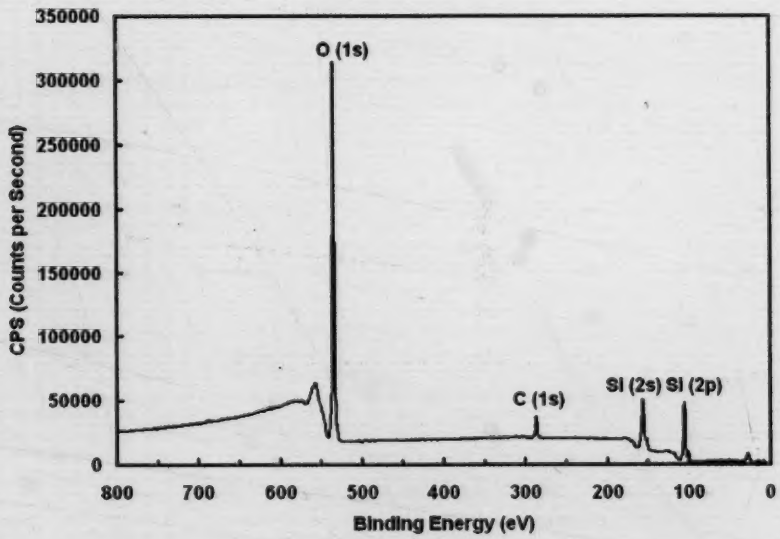

(b)

Figure 3.4: X-ray photoelectron scan of Si substrates functionalized with (a) propyl-trichlorosilane and (b) hexyl-trichlorosilane.

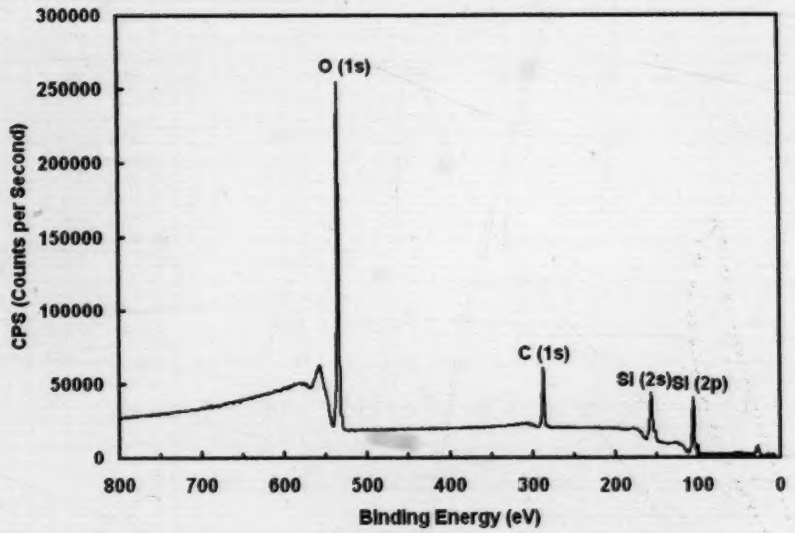

(a)

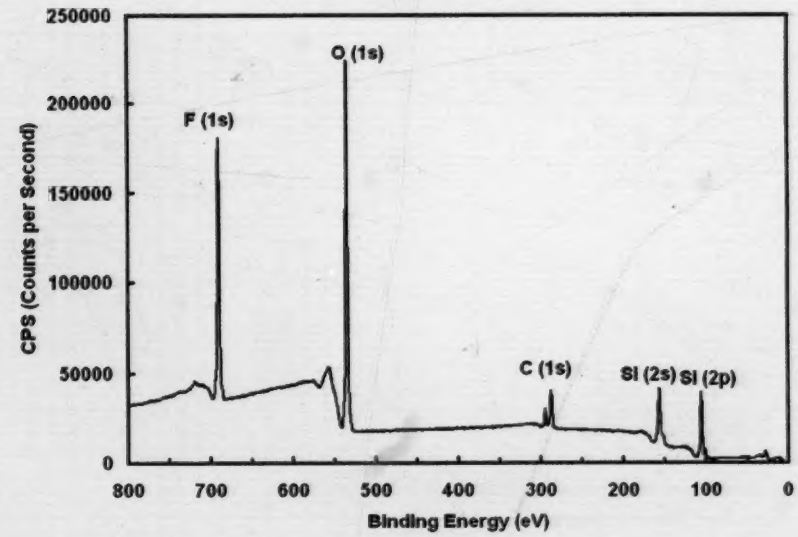

(b)

Figure 3.5: X-ray photoelectron scan of Si substrates functionalized with (a) octadecyl-trichlorosilane and (b) trifluoropropyl-trichlorosilane.

Figure 3.6: Illustration of the contact angle of a liquid on a solid surface.

Table 3.1: Advancing contact angle (θ) and RMS surface roughness of as-supplied, RIE-treated, and alkyltrichlorosilane derivatized Si substrates and the corresponding wetting layer thickness (WLT) of thermally evaporated Alq_3 thin films.

Substrate surface treatments	θ (°)	RMS (nm)	WLT (nm $\pm$ 8 nm)	
			4 Å/s	1 Å/s
Si	20	0.2	147	300
RIE treated and baked Si	48		126	283
TFP-$SiCl_3$	90	1.0	59	182
Hexyl-$SiCl_3$	93	0.8	50	176
Propyl-$SiCl_3$	99	1.1	53	165
OTS	101	0.2	44	100

SEM images of the helical Alq_3 nanostructures shown in Fig. 3.7 to illustrate that the thickness of the initial solid layer decreased with increasing substrate surface hydrophobicity, implying that greater surface hydrophobicity better matches the interfacial surface energy between Alq_3 and the substrate, as supported by contact angle measurements. This is consistent with a qualitative comparison of the advancing aqueous contact angle of Alq_3 thin films and that of functionalized substrates.

As previously stated, the Alq_3 depositions were performed at a rate of either 4 Å/s or 1 Å/s. The increased deposition rate was achieved by marginally increasing the temperature (~10°C) of the effusion cell. Since the difference in the deposition temperatures is small, the molecules deposited at both rates should have similar kinetic energies. Though the substrate temperature was not monitored, previous experiments have shown that thermal

deposition of materials with much higher source temperatures (>1500°C) led to increases in substrate temperature of ~100K after 90 minutes of deposition [69]. It is expected that Alq_3 deposition at much lower source temperatures (<300°C) will exhibit correspondingly lower substrate temperature increases. At a higher deposition rate, adsorbed molecules and impinging molecules interact more frequently, and self-shadowing becomes more dominant as surface diffusion is further limited by the incoming flux which buries the deposited material, and wetting layer thickness decreases. For both deposition rates, the manner in which the wetting layer thickness varied with substrate wettability was very similar (Fig. 3.8).

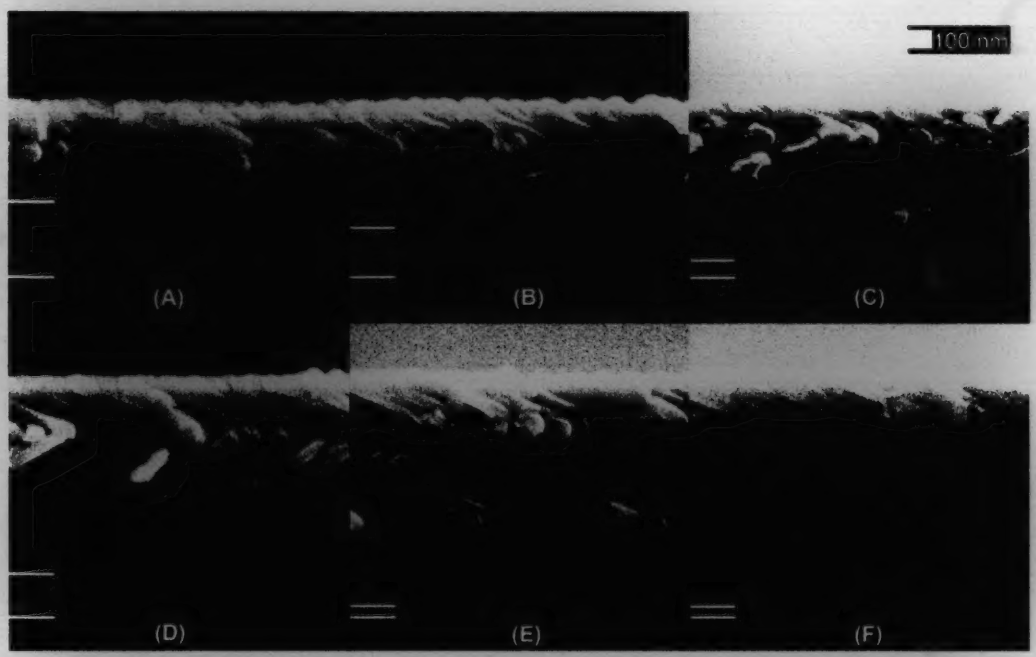

Figure 3.7: SEM images of helices at deposited at 1 Å/s (A, B, C) and 4 Å/s (D, E, F). Images consist of Alq_3 deposited on (A, D) bare silicon substrates, (B, E) hexyltrichlorosilane functionalized substrates, and (C, F) octadecyltrichlorosilane functionalized substrates. White horizontal lines indicate the extent of the Alq_3 wetting layer.

In general, the wetting layer thickness decreases for substrates with higher advancing contact angle measurements and lower surface roughness. The minimum wetting layer thickness was achieved using OTS derivatized substrates as they exhibit the greatest advancing contact angle and lowest RMS roughness. This shows that the formation

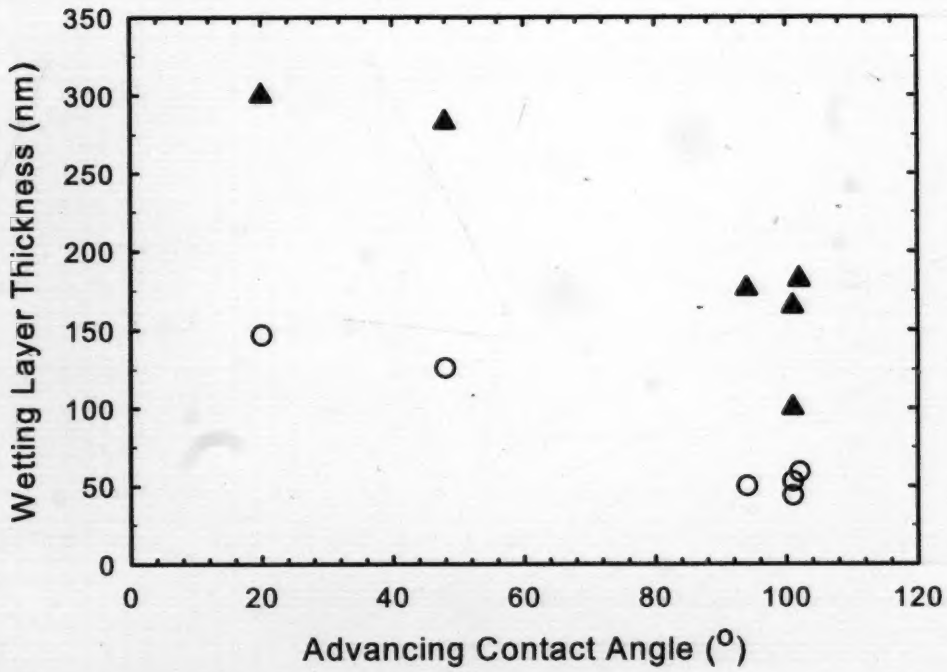

Figure 3.8: Wetting layer thickness of Alq_3 deposited at 76° varies with respect to deposition rate, 4 Å/s (○) and 1 Å/s (▲), and the surface hydrophobicity of substrates as measured by advancing aqueous contact angle.

of wetting layers at the base of Alq_3 GLAD films deposited onto alkyltrichlorosilane derivatized Si substrates at both 4 Å/s and 1 Å/s is strongly dependant upon substrate wettability as well as deposition rate.

3.3 Summary

In summary, we have demonstrated that the growth of the wetting layer is influenced by several parameters including the deposition angle, surface wettability, and deposition rate. The parameters can be used to tailor the wetting layer thickness of Alq_3 nanostructures deposited using the GLAD technique. The role of the surface energy mismatch between the impinging Alq_3 molecules and the surface substrate was investigated using chemically functionalized organosiloxane derivatized substrates and by varying the deposition rate. The wetting layer thickness was noted to decrease significantly with increasing deposition rates due to the limited surface diffusion caused by the coverage of the incoming flux. The wetting layer thickness decreased with increasing surface hydrophobicity due to the smaller surface energy mismatch. A similar trend was observed when the oblique angles of incidence increased, which increased the effects of self-shadowing and self-burying. Under these conditions, the formation of GLAD nanostructures occurred at thinner wetting layer thickness. Varying surface wettability in conjunction with the deposition parameters offers the ability to control the wetting layer thickness, which is critical for realization of optoelectronic devices.

Chapter 4

Optical properties of Alq_3 columnar thin films[1]

The optical properties of Alq_3 have been of particular interest and the focus of in depth study due to the wide use of Alq_3 as a light emitting layer in OLED devices [36,55,70–72]. Recent studies into the optical properties of chiral nanostructured Alq_3 fabricated using GLAD have demonstrated the presence of strong circular Bragg effects [12, 53]. The spectral location of the circular Bragg effects was tailored by changing the deposition angle or the substrate rotation rate, or both, which changed the porosity of the film and helical pitch of the nanostructures.

In order to understand the anisotropic properties of various inorganic materials, thin films composed of slanted columns have been fabricated using oblique angle deposition techniques in previous studies and optically characterized to demonstrate both biaxial optical anisotropy and in-plane birefringence [9,10,73,74]. These studies are fundamental to describing more complex structures that can be fabricated using deposition techniques such as GLAD. In this chapter, the fundamental optical properties of nanostructured Alq_3 slanted columns is discussed and correlated with the unique structural morphology of Alq_3 nanostructures.

[1]A version of this chapter has been published and is reproduced with permission from: B. Szeto, P. C. P. Hrudey, J. Gospodyn, J. C. Sit, and M. J. Brett, "Obliquely deposited tris(8-hydroxyquinoline) aluminum (Alq_3) biaxial thin films with negative in-plane birefringence," *J. Opt. A: Pure Appl. Opt.*, vol. 9, pp. 457-462, 2007. Copyright Institute of Physics and IOP Publishing Limited 2007.

4.1 Background Optics

4.1.1 Linear Birefringence

Columnar thin films composed of tilted columns are the most basic biaxial thin film that can be fabricated through oblique angle deposition techniques such as GLAD [75, 76]. Biaxial media are characterized by 3 distinct principal refractive indices along 3 mutually orthogonal directions referred to as n_x, n_y, and n_z (Fig. 4.1). Light polarized along any of these axes travels at a different phase velocity, ν, defined by:

$$\nu = \frac{c}{n_i} \tag{4.1}$$

where c is the speed of light.

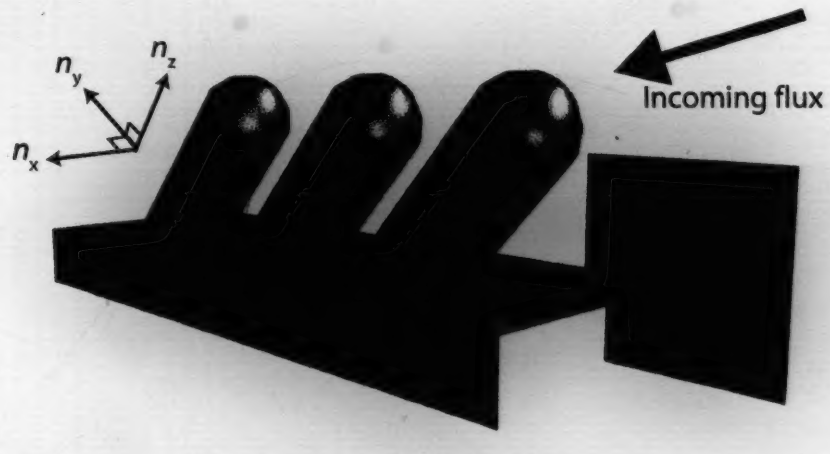

Figure 4.1: Illustration of a biaxial media.

Tilted columnar thin films are fabricated by physical vapour deposition while holding the substrate at a fixed angle of incidence, relative to the incoming vapour flux. Inorganic tilted columnar films typically grow with characteristic fan-shaped cross-sections [77] at column tilt angle β with respect to substrate normal, where $0° < \beta < \alpha$. An example of an inorganic silica slanted columnar thin film deposited at $\alpha = 88°$ is shown in Fig. 4.2. Column broadening occurs in the individual columns while growth competition effects are visible as the smaller diameter columns in the background which are shadowed by the neighbouring columns and cease to receive any additional incoming vapour flux. Column

broadening perdendicular to the deposition plane occurs due to the one-dimensional shadowing effects that occur during the deposition. As the films grows, the nanostructured columns in the front shadow the structures behind. This effect limits the available regions that material can be deposited onto by restricting deposition to sides and top of the column tip where there is no shadowing (Fig. 4.3). As a result, the column expands outwards as the film grows and forms a fan-shaped cross-section which may also cause individual columns to chain together in thicker films. This effect increases the index of refraction in the fanning direction, n_x, since the ratio of material versus void is increased as the film continues to grow. The primary anisotropy in these films is caused by the tilted nature of columns which modifies the cross-section area of the columns by increasing the length in the direction of the tilt (i.e. in the deposition plane) when sliced parallel to the substrate. The fan-shaped cross-sections cause a secondary anisotropy to occur due to the fanning shape of the columns which grow perpendicular to the column tilt. These two competing effects modify the biaxial properties of inorganic tilted columnar films and determine the birefringent nature of the film (Fig. 4.4). When viewed at normal incidence to the substrate plane, the dominant secondary structural anisotropy of inorganic tilted columnar films gives rise to positive in-plane birefringence values according to Eq. 4.2, which defines the in-plane birefringence, Δn, as:

$$\Delta n = n_x - n_p \tag{4.2}$$

where the index of refraction in the deposition plane (planes parallel to the direction of the incoming vapour flux) and parallel to the substrate, n_p, is given by:

$$n_p = \left(\frac{sin^2\beta}{n_z^2} + \frac{cos^2\beta}{n_y^2} \right)^{-1/2} \tag{4.3}$$

where n_x is in the substrate plane perpendicular to the deposition plane, n_y is in the deposition plane and perpendicular to the column posts, and n_z is aligned in the direction of the posts (Fig. 4.5).

Figure 4.2: SEM image of silica slanted columnar thin film deposited at $\alpha = 88°$ as viewed along the direction of the columns. The white arrow indicates the direction of the incoming vapour flux. Broadening occurs for individual columns while growth competition is observed as smaller diameter columns are visible in the background.

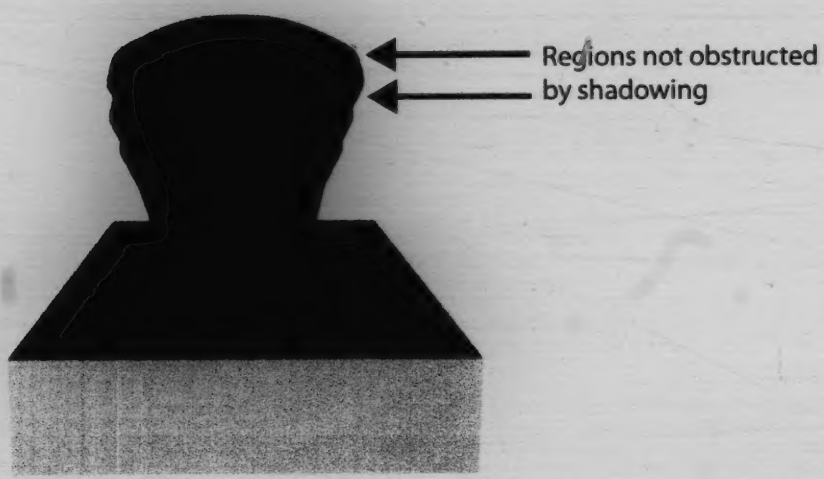

Figure 4.3: Illustration of the 1-D shadowing that occurs during tilted columnar thin film growth that causes column broadening.

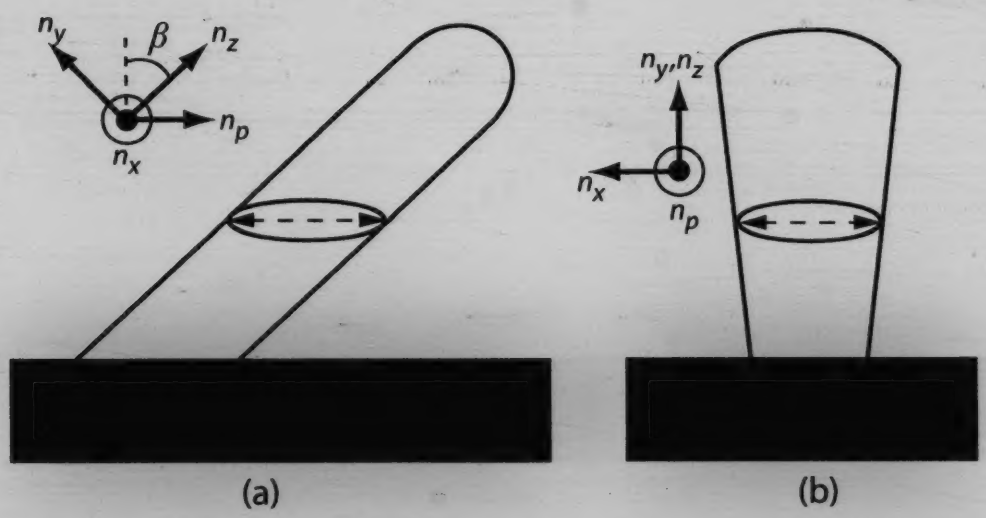

Figure 4.4: Illustration of the competing effects that modify the biaxial properties in a slanted columnar thin film where (a) is a view perpendicular to the deposition plane showing the primary anisotropy caused by the column tilt and (b) is a view along the deposition plane showing the secondary anisotropy caused by column broadening.

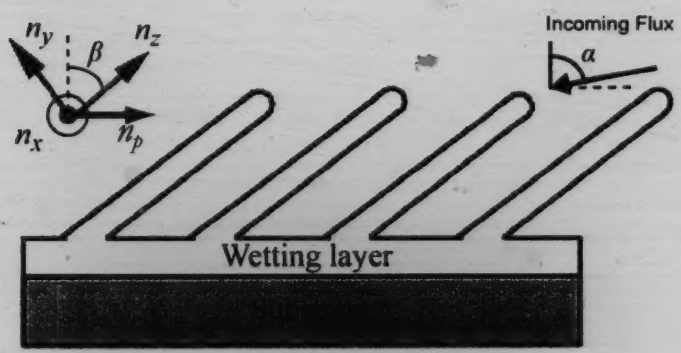

Figure 4.5: Illustration of the indices of refraction in tilted, columnar thin films grown by GLAD. The wetting layer is a feature observed only in organic GLAD films.

4.1.2 Circular Bragg effect

When circularly polarized light is transmitted through a chiral medium, the polarization of light with the same handedness as the chiral medium will interact strongly with the medium. Light of the opposite handedness does not couple to the medium and is thus not affected by the chiral structure. The circular polarization behavior of the helical samples can be measured by the transmission of light through the chiral film using variable angle spectroscopic ellipsometry (VASE) [53]. The transmittance and Mueller matrix, a 4 x 4 matrix that relates the input and output polarization states of light incident upon a sample, can be used to determine the transmittance of left-handed circularly polarized light (T_{LCP}) and right-handed circularly polarized light (T_{RCP}) through the chiral medium [5].

$$T_{LCP}(\lambda) = m_{11}(\lambda) - m_{14}(\lambda) \tag{4.4}$$

$$T_{RCP}(\lambda) = m_{11}(\lambda) + m_{14}(\lambda) \tag{4.5}$$

The circular Bragg phenomenon occurs due to the reflection of light from a periodic structure. The origin of the effect is the rotation of the linear birefringent structure. Circular Bragg effects are preferential reflections of one circular polarization state, or handedness, and transmission of the opposite circular polarization state [78]. For example, a film consisting of right handed (RH) helices will preferentially transmit left-circularly polarized (LCP) light while a film with left-handed (LH) helices will preferentially transmit right-circularly polarized (RCP) light. The wavelengths at which this circular Bragg effects occurs is dependent on the helical pitch, p, and index of refraction of the material, and lie between λ_1=pn_o and λ_2=pn_e, where n_o and n_e are the ordinary and extraordinary indices of refraction of the chiral structure. The optical properties of the chiral films can be tuned by manipulating the pitch of the individual helices and modifying the porosity of the film. The polarization of light emitted from luminescent nanostructures was of particular interest as Lakhtakia *et al.* [79] and Kopp *et al.* [80] predicted that luminescent chiral thin films that should emit circularly polarized light in the region of the optical stop band. This prediction has been recently experimentally verified by Hrudey *et al.* [12, 53].

The magnitude of the circular Bragg effect increased at higher deposition angles in Alq_3 chiral films [53]. This increase has been predicted to vary with the square of Δn, the birefringence [81]. The trend of stronger circular Bragg effects at higher deposition angles seen in chiral Alq_3 films suggests that the in-plane birefringence of tilted columnar Alq_3 films should increase with deposition angle. Such a trend would be in direct contrast to the situation observed for inorganic titled columnar films, which exhibit peak values of in-plane birefringence at deposition angles $60° < \alpha < 70°$ [81, 82]. The peak values occur at deposition angles where the column broadening effects, which increases n_x, are the most dominant over the effects caused by the column tilt, which increases n_p. Unlike this behavior in inorganic materials, the expected the magnitude of the birefringence in Alq_3 films should continue to increase as the deposition angle is increased.

To better investigate the source of the in-plane birefringence exhibited by Alq_3 films, tilted columnar thin films are fabricated (Fig. 4.6) and characterized using variable angle spectroscopic ellipsometry (VASE) and the Bruggeman effective medium approximation (BEMA) description which are described in more detail in the next section. Using VASE and BEMA, the principal indices of refraction of tilted columnar Alq_3 films, as well as structural parameters such as the column tilt angle, β, and the relative film density can be determined [83]. Knowledge of these parameters will ultimately prove useful for modelling and optimizing the optical properties of porous Alq_3 films utilized in potential devices such as luminescent coatings, optical filters, and photonic crystals.

4.2 Variable angle spectroscopic ellipsometry

Ellipsometry is a optical measurement technique that uses polarized light to characterize thin films, surfaces, and material microstructure. Ellipsometric analysis is based on solving Maxwell's equations by using the complex Fresnel reflection coefficients r_p (in the plane of incidence) and r_s (perpendicular to the plane of incidence) to determine the ellipsometric measurement parameters for the relative amplitude change (Ψ) and relative phase change (Δ) upon reflection based on the relationship:

$$\tan(\Psi)e^{i\Delta} = \frac{r_p}{r_s} \tag{4.6}$$

A similar equation is used for transmission measurements.

Ellipsometry is particularly versatile for thin film characterization due to the fact that the intensity ratio is measured instead of pure intensities which reduces the influence of intensity instabilities of the light source or atmospheric absorption. This allows highly accurate and reproducible scans to be performed [84, 85]. Spectroscopic ellipsometry (SE) measures the complex ratio as a function of wavelength, while variable angle spectroscopic ellipsometry (VASE) includes the ability to perform the measurement as a function of both wavelength and angle of incidence. This enables the sensitivity of the measurement to be optimized by providing additional information based on the different optical path lengths travelled by the light. Material parameters such as layer thickness, surface roughness, and optical constants can all be extracted from the ellipsometer data using a model-based analysis method and the VASE software. The first step is to build a model of the film that is being measured. This model needs to include the order of the layers, their optical constants, and their thickness. If these values are not known an estimate is used. Measurements from SEM images are used for estimates such as thickness and nanostructure column orientation. A model is generated from the data and compared to the experimental VASE optical measurements using the VASE software. The software uses an iterative method to change the model parameters until they correspond and fit with the experimental data. Fig. 4.7 summarizes the process used for the optical modelling of Alq_3 films.

Before analysis of obliquely deposited films could be performed, a solid Alq_3 film grown at $\alpha = 0°$ was optically characterized using a commercially available variable angle spectroscopic ellipsometer (V-VASE, J. A. Woollam Co., Inc.). The ellipsometric parameters Ψ and Δ were obtained over the wavelength range of 300 to 1300 nm for angles of light incidence from 50° to 70° with respect to substrate normal in order to avoid the Brewster's angle. The normally deposited film was then modelled optically (Fig. 4.8) using a Lorentz and Tauc-Lorentz oscillator system, which produced optical constant profiles

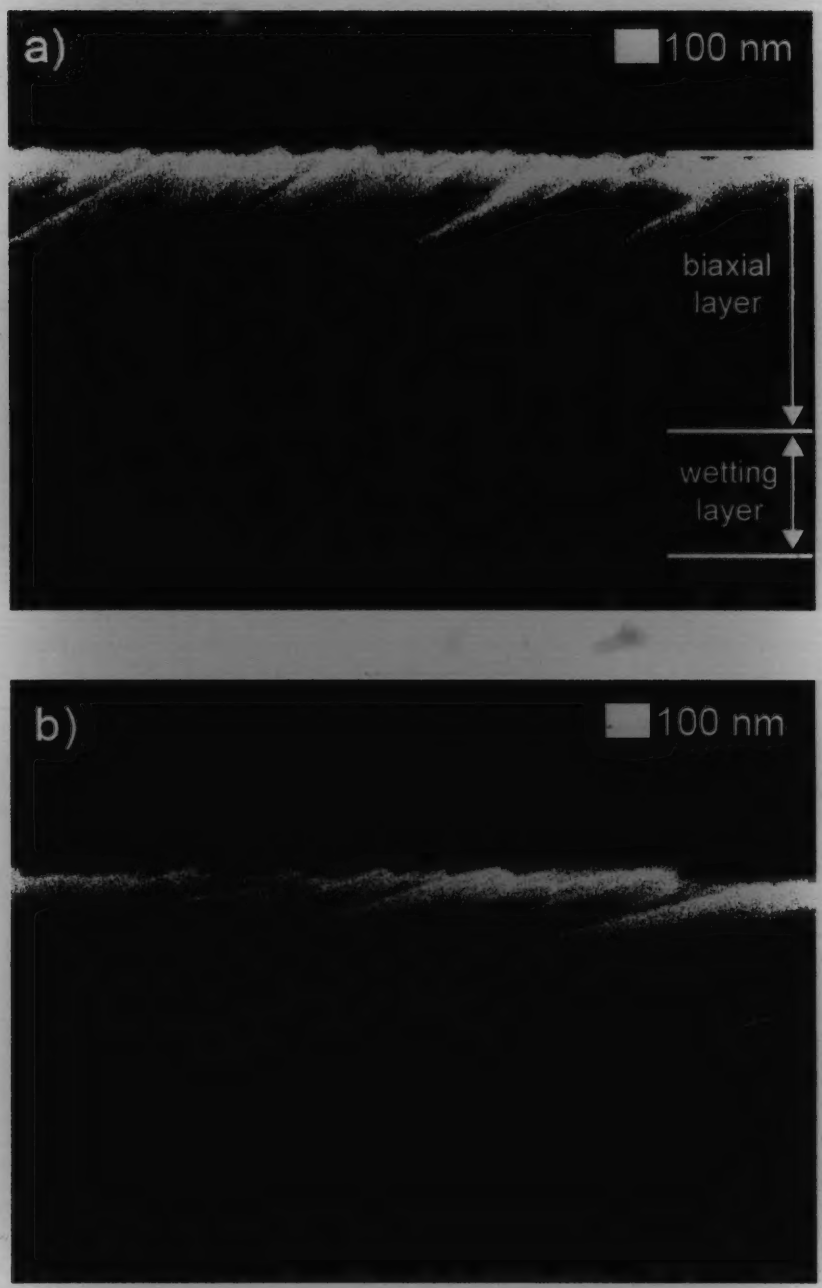

Figure 4.6: Cross sectional SEM images of tilted columnar thin films deposited at a) α = 71° and b) α = 85°.

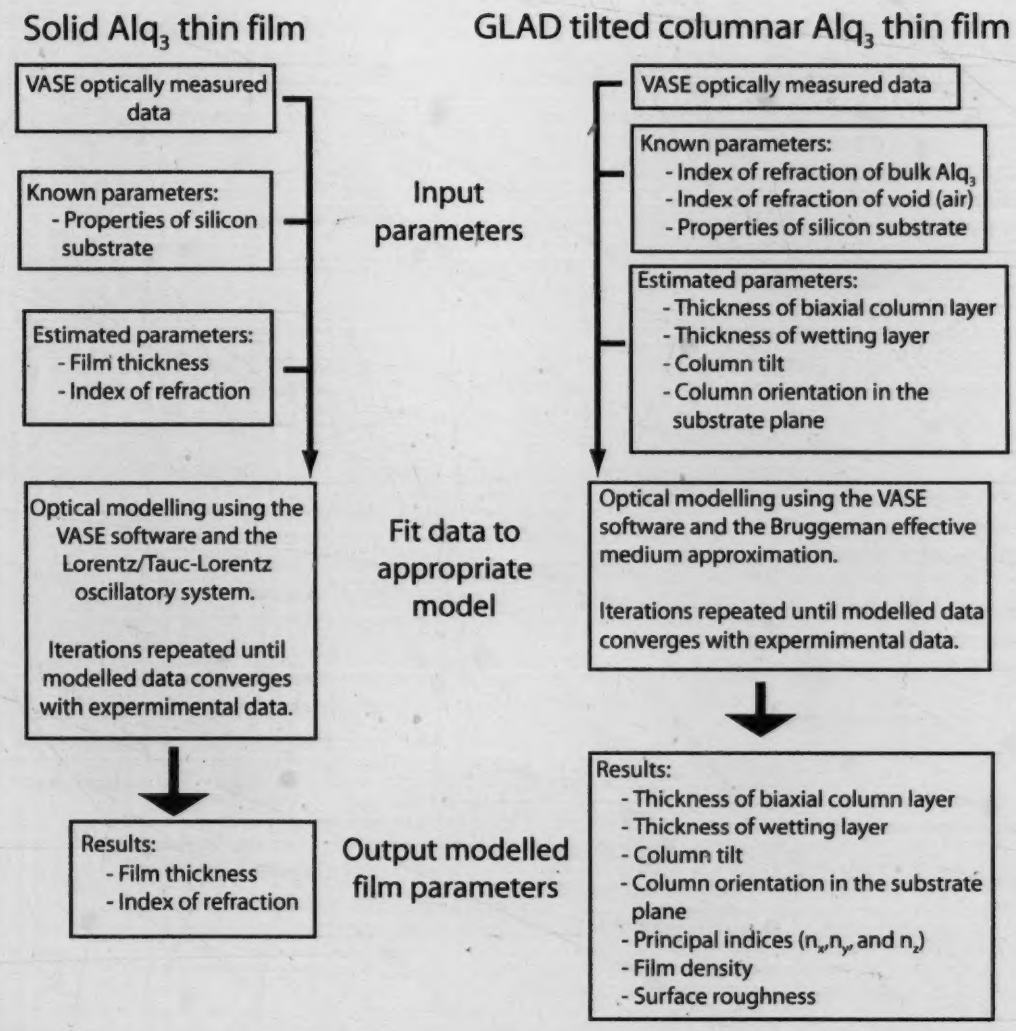
Solid Alq_3 thin film
GLAD tilted columnar Alq_3 thin film
VASE optically measured data
Known parameters:
- Properties of silicon substrate
Estimated parameters:
- Film thickness
- Index of refraction
Input parameters
VASE optically measured data
Known parameters:
- Index of refraction of bulk Alq_3
- Index of refraction of void (air)
- Properties of silicon substrate
Estimated parameters:
- Thickness of biaxial column layer
- Thickness of wetting layer
- Column tilt
- Column orientation in the substrate plane
Optical modelling using the VASE software and the Lorentz/Tauc-Lorentz oscillatory system.
Iterations repeated until modelled data converges with expermimental data.
Fit data to appropriate model
Optical modelling using the VASE software and the Bruggeman effective medium approximation.
Iterations repeated until modelled data converges with expermimental data.
Results:
- Film thickness
- Index of refraction
Output modelled film parameters
Results:
- Thickness of biaxial column layer
- Thickness of wetting layer
- Column tilt
- Column orientation in the substrate plane
- Principal indices (n_x,n_y, and n_z)
- Film density
- Surface roughness

Figure 4.7: Chart outlining the optical modelling process for solid and slanted columnar Alq_3 thin films.

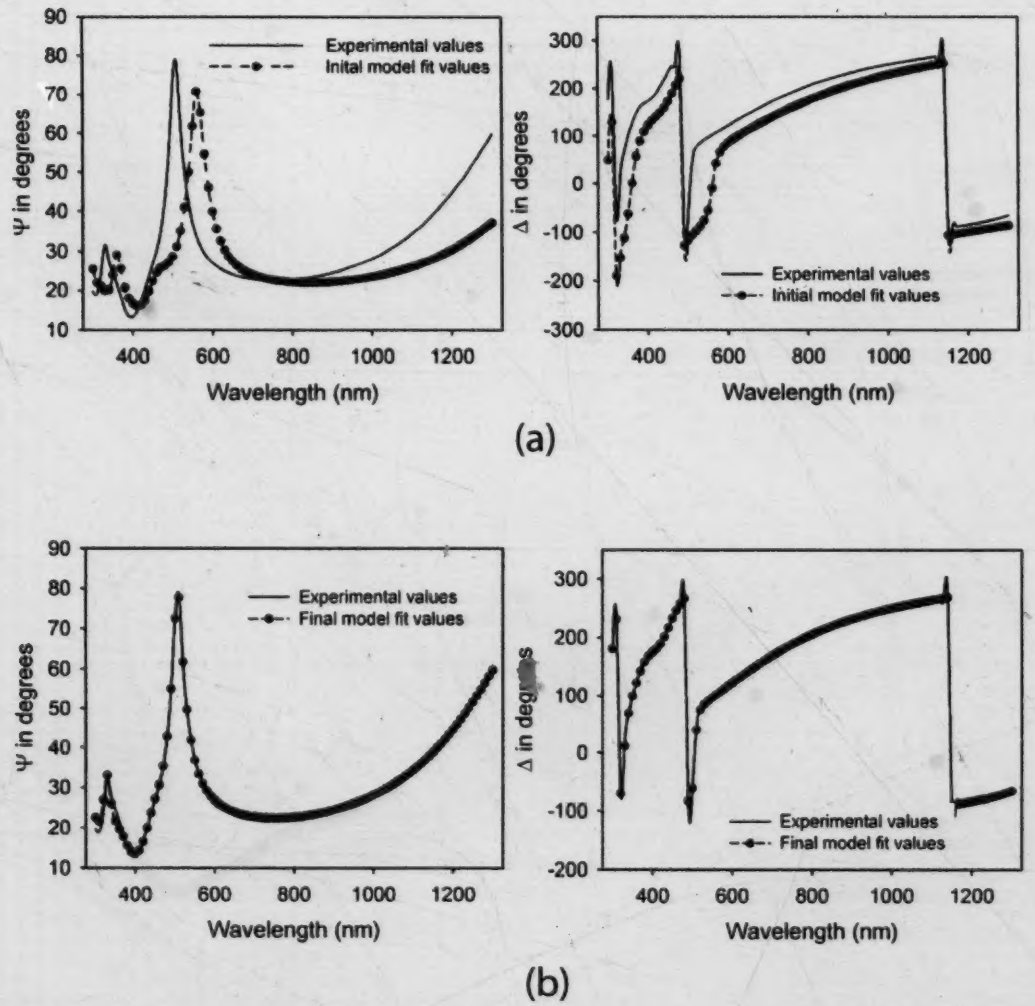

Figure 4.8: Example of model fitting in a solid Alq_3 film (a) before the fitting process and (b) after the fitting process. Only data for the 60° angle of incidence is shown for simplification.

(Fig. 4.9) comparable to previous studies [72, 86], yielding $n = 1.7343$ and $k = 0.0026$ at a wavelength of 525 nm. The particular wavelength was picked because of the minimal absorption at that wavelength which is also located at the peak of the Alq_3 photo- and electoluminescence spectra. Optical modelling was performed using the software package supplied with the ellipsometer (WVASE32 version 3.517, J. A. Woollam Co., Inc.). To analyze the optical properties of the obliquely deposited Alq_3 films, the normalized Mueller matrices [84] of the films were measured using the V-VASE in reflection mode at light angles of incidence from 40° to 60° with respect to substrate normal, for wavelengths from 400 nm to 1300 nm. The Mueller matrix is a 4 x 4 matrix that relates the input and output polarization states of light incident upon a sample. The VASE automatically normalizes the Mueller matrix measured by setting the overall transmittance of the system, defined by the m_{11} element of the matrix, to unity.

All the fit results in the VASE software were given an error bar corresponding to the 90% standard confidence limit (SCL), which was used to compute any error bars that appear in figures presented in this chapter. The confidence limit is used to describe the confidence in a fit parameter element in the covariance matrix by [87]:

$$SCL_i = 1.65 * \sqrt{C_{ii}} \tag{4.7}$$

The error in the fit value describes both the combined measurement and fitting process. The error of any modelled data collected is a function of the SCL and mean squared error (MSE) and defined by:

$$error = SCL_i * \sqrt{MSE} \tag{4.8}$$

The VASE software provides the error in all the fit parameters used in the modelling process, however it does not provide the value for the in-plane birefringence nor its error since it is not one of the model fit parameters. The in-plane birefringence is calculated based on Eq. 4.2, however, in order to calculate the error of the in-plane birefringence the error in n_p must be determined. A program was written using the

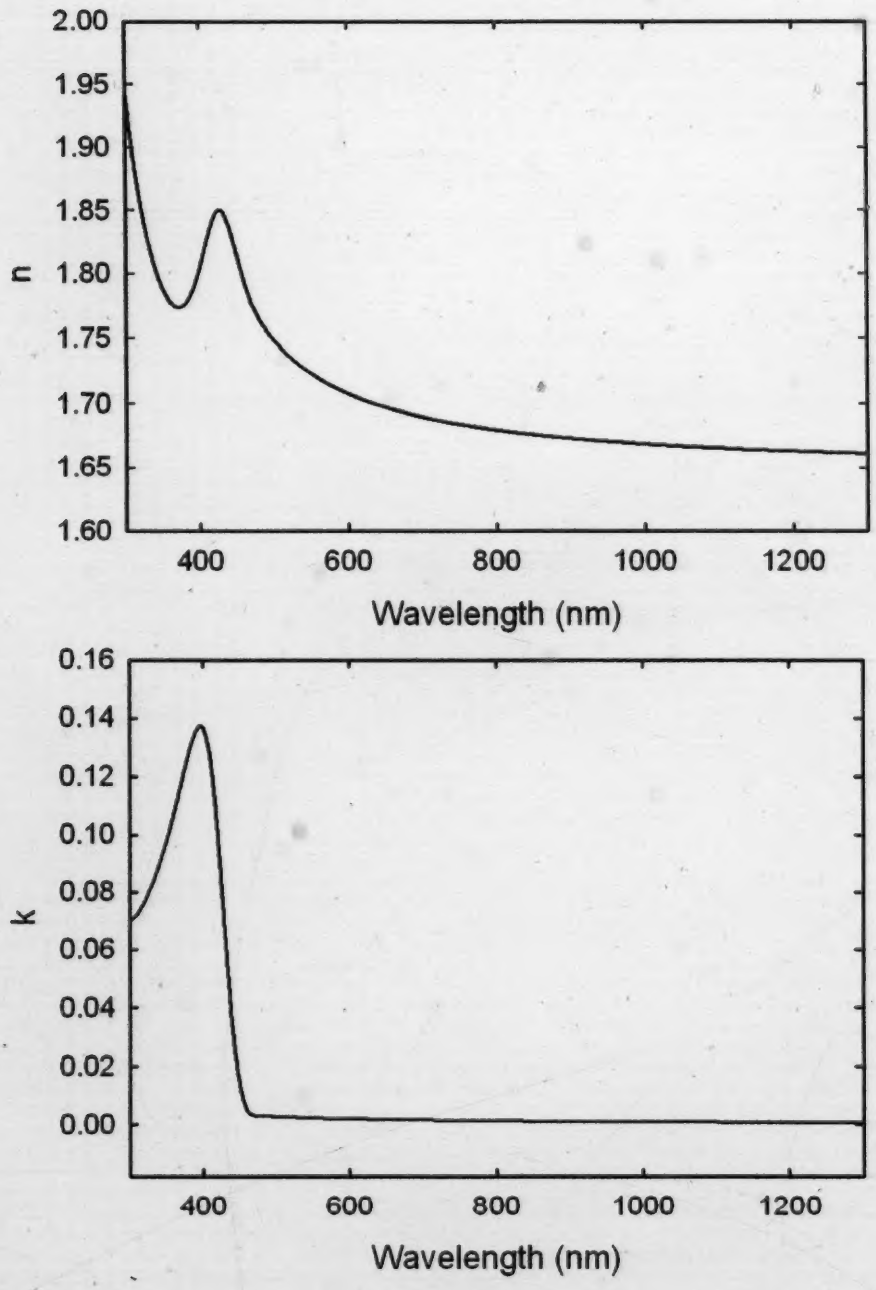

Figure 4.9: Measured real and imaginary parts of the index of refraction of Alq_3.

mathematical analytic Maple software package to calculate this value (Appendix A). Maple is a symbolic mathematics program capable of highly complex mixed symbolic and numeric programming.

4.3 Bruggeman effective medium approximation

Effective medium theories are quantitative models that are capable of obtaining the macroscopic dielectric properties of heterogeneous thin films i.e particles of one material embedded in a host matrix of a second material. Effective medium theory is derived from a solution of the Clausius Mossotti relation from basic principles which can be generalized into different effective medium approximations such as the Lorentz-Lorentz, Maxwell Garnett, and Bruggeman expressions [88]. The Bruggeman formulism is commonly used to describe bianisotropic thin films [89,90]. The Bruggeman effective medium approximation (BEMA) is particularly practical for columnar thin films since it can accomodate the elliptical inclusions caused by the anisotropic nature of the biaxial slanted posts [88, 91]. This method was used in a similar study on the inorganic materials MgF_2 and SiO_2 [74]. The general Bruggeman equation describes a random mixture of two materials embedded into the effective medium and is given by:

$$0 = \eta_1 \left(\frac{\epsilon_1 - \epsilon}{\epsilon_1 + 2\epsilon} \right) + \eta_2 \left(\frac{\epsilon_2 - \epsilon}{\epsilon_2 + 2\epsilon} \right) \tag{4.9}$$

where $\eta_{1,2}$ are the volume fractions of the two materials, $\epsilon_{1,2}$ are the dielectric constants of the two materials, and ϵ is the dielectric constant for the effective medium (Fig. 4.10).

In order to describe slanted columnar thin films, the modified Bruggeman equation for elliptical inclusions is used (Eqn. 4.10).

$$0 = \rho \left(\frac{\epsilon_{mat} - \epsilon}{\epsilon_{mat} + \epsilon(q_i^{-1} - 1)} \right) + (1 - \rho) \left(\frac{\epsilon_{void} - \epsilon}{\epsilon_{void} + \epsilon(q_i^{-1} - 1)} \right) \tag{4.10}$$

where ρ is the density of the film, ϵ_{mat}, ϵ_{void}, ϵ are the dielectric constants for the material, void, and effective medium, and q_i are the depolarization factors for the three principle

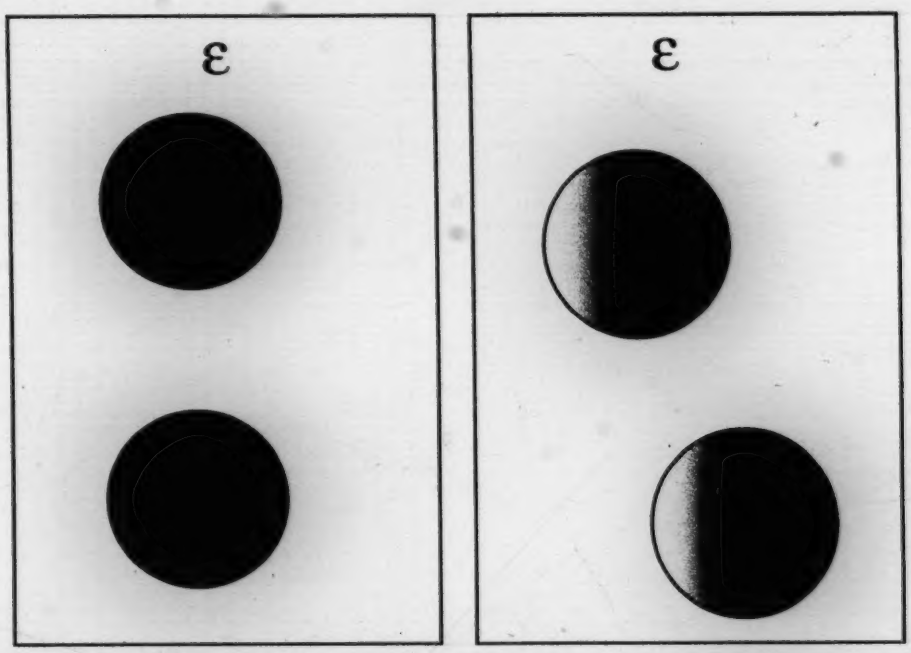

Figure 4.10: Illustration of the general Bruggeman effective medium approximation with two spherical inclusions embedded into the effective medium.

indices (Fig. 4.11). The depolarization factors (q_x, q_y, and q_z) are parameters used to describe the elliptical inclusions of the Bruggeman model and obey the relationship:

$$q_x + q_y + q_z = 1 \tag{4.11}$$

The obliquely deposited Alq_3 films were modelled using three layers on top of a silicon substrate (Fig. 4.12). The first layer modelled a solid wetting layer of Alq_3 that forms prior to the growth of individual structures [12,92]. The second layer described the biaxial slanted posts using the BEMA, where the two constituent media consisted of Alq_3 and void (i.e. $n_{void} = 1$, $k_{void} = 0$). The third layer consisted of a surface roughness layer, which was included to compensate for the slight variation in column heights between individual posts. The parameters that were simultaneously fit using the modelling software were the thicknesses of each of the three layers, the film density in the tilted column layer, the screening parameters describing the cylindrical inclusions, and the Euler angles ω (which in our case is synonymous with β) and ζ which describe the column orientation with respect

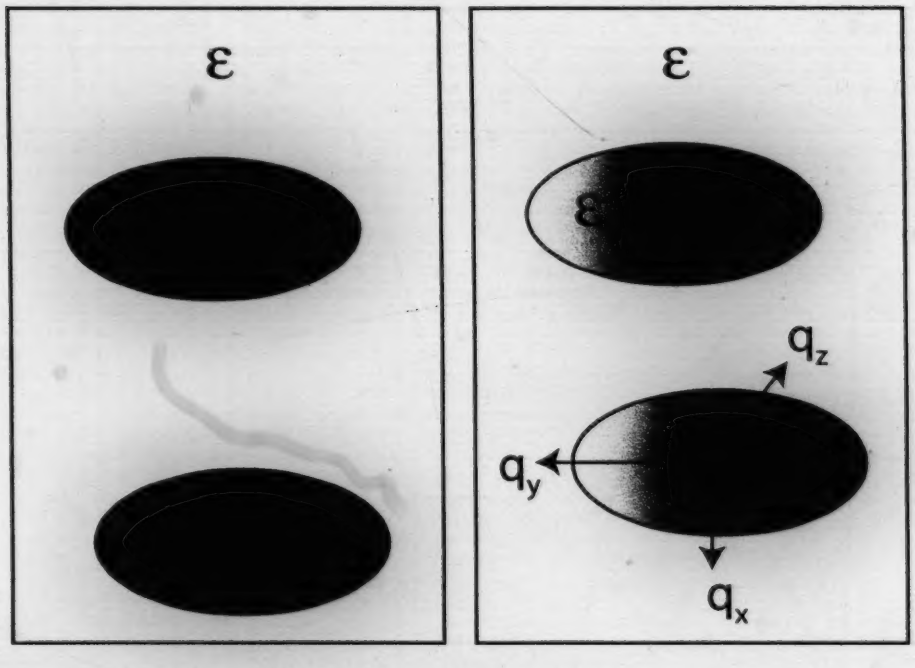

Figure 4.11: Illustration of the Bruggeman effective medium approximation for two elliptical inclusions embedded into the effective medium.

to the lab coordinate system. The Euler angle, ζ, is the azimuthal angle that describes the orientation of the columns in the substrate plane. Although the angle ζ was defined as a fit parameter, it was known to within a few degrees due to careful alignment of the sample on the ellipsometer sample stage. Correspondingly, the model fit for ζ was always within a few degrees of our estimate.

Layer Number	Layer	Thickness
3	Surface roughness	29.2 nm
2	Biaxial BEMA, Alq_3 83.5%/Void 16.5%	612 nm
1	Alq_3 wetting layer	269.5 nm
0	Silicon Substrate	0.25 mm

Figure 4.12: Multilayer model of columnar thin film deposited at $\alpha = 71°$.

From the optical model, we obtained the three principal indices of refraction for the biaxial films, which were defined in the same fashion as in previous studies and Fig. 4.5 [74, 81, 93]. By determining the principal indices of refraction (Fig. 4.13), the in-plane birefringence can be calculated using Eq. 4.2 and 4.3.

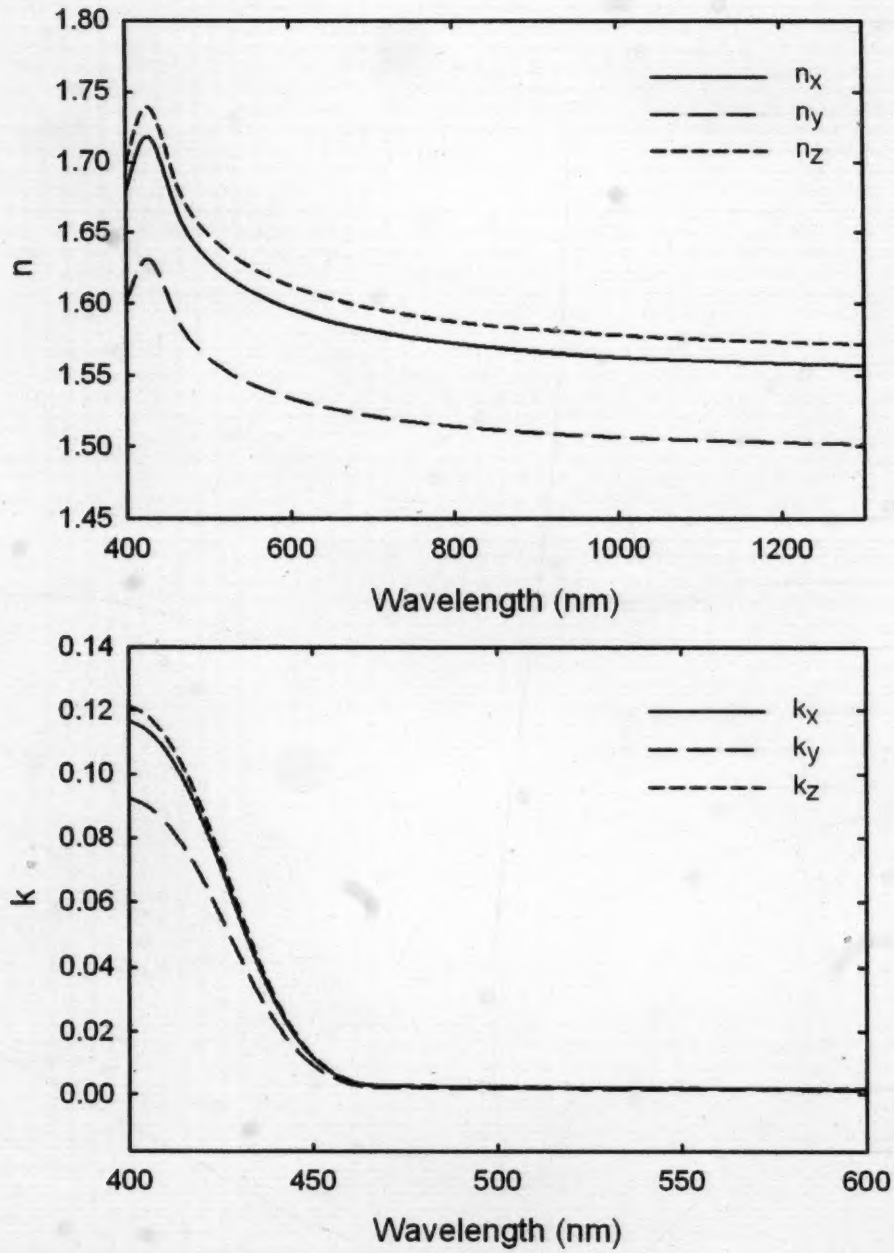

Figure 4.13: Measured real and imaginary parts of the principle indices of refraction of the Alq_3 columnar thin film deposited at $\alpha = 71°$.

4.3.1 Column Angle

To obtain an estimate for the comparison with the optically measured data, the column tilt angle β was measured by examining the cross-sectional SEM images of the films. The SEM measured column angle (○) and that given by the BEMA modelled results (▲) are shown in Fig 4.14. The modelled data are in reasonable agreement with measured values obtained from SEM images of deposition plane fractures, where discrepancies are primarily attributed to the accuracy of cleaving the SEM samples exactly parallel to deposition plane. Also shown for comparison is Tait's geometrically-derived rule for columnar growth at oblique angles of incidence (solid line) [20]. The experimental values for the column angle shows a similar trend relative to the deposition angle as the values predicted by Tait's rule however with a larger magnitude. This discrepancy is likely due to the fact that Tait's rule is a geometry based guideline that does not account for material specific behaviour including bulk diffusion, surface diffusion, and chemical interactions. The larger magnitudes of the column tilt angles observed in Alq_3 films are significant, as the column tilt angles of most inorganic tilted columnar thin films tend to be lower than the values predicted by Tait's rule [94]. This may suggest that the roles of diffusion and chemical interactions during the growth of tilted columnar Alq_3 are significantly different from the roles of such effects during inorganic oblique angle film growth.

4.3.2 Density and indices

Fig. 4.15 shows the normalized density (density compared to the film grown at $\alpha = 0°$) of the biaxial post layer as a function of deposition angle with the predicted density using Tait's rule included as a guideline. As expected, the film density decreases as the deposition angle is increased due to increased self-shadowing that occurs at higher deposition angles, thus increasing the average spacing between nucleation sites. The result is an increase in the ratio of void to film, which decreases the effective index of refraction of the tilted column layer. The computed values for the three principal indices at a wavelength of λ = 525 nm are given in Fig. 4.16, and, as expected, the values of the principal indices of refraction decrease with deposition angle, due to the increase in overall porosity.

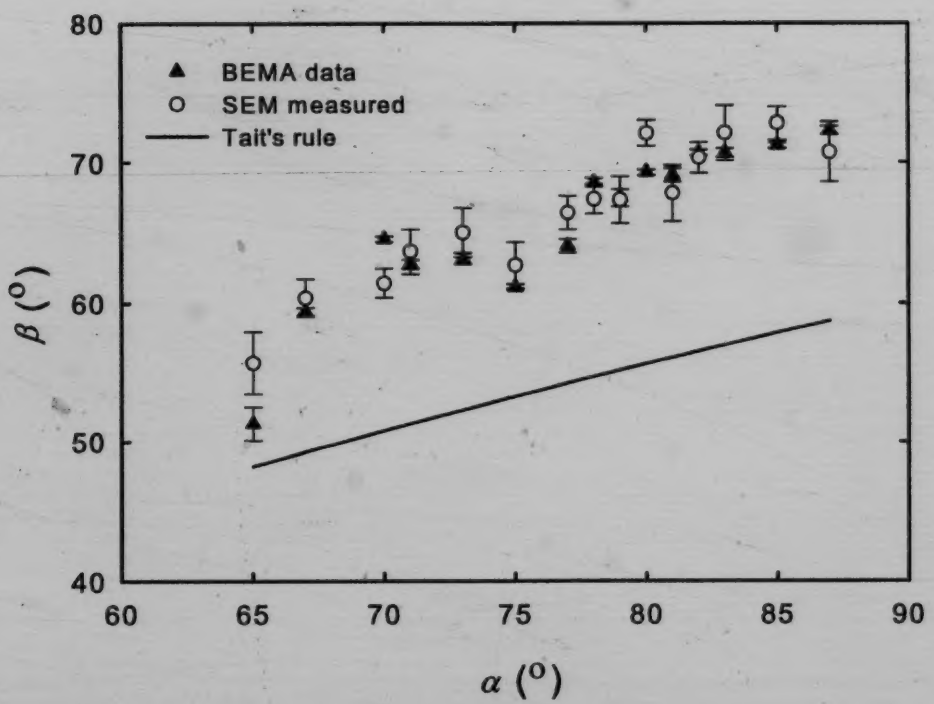

Figure 4.14: SEM measured and BEMA model column tilt as a function of the deposition angle α. The error bars for the SEM measurements represent one standard deviation of β for each deposition angle. Column tilt value predicted by Tait's rule (solid line) is shown as a guide.

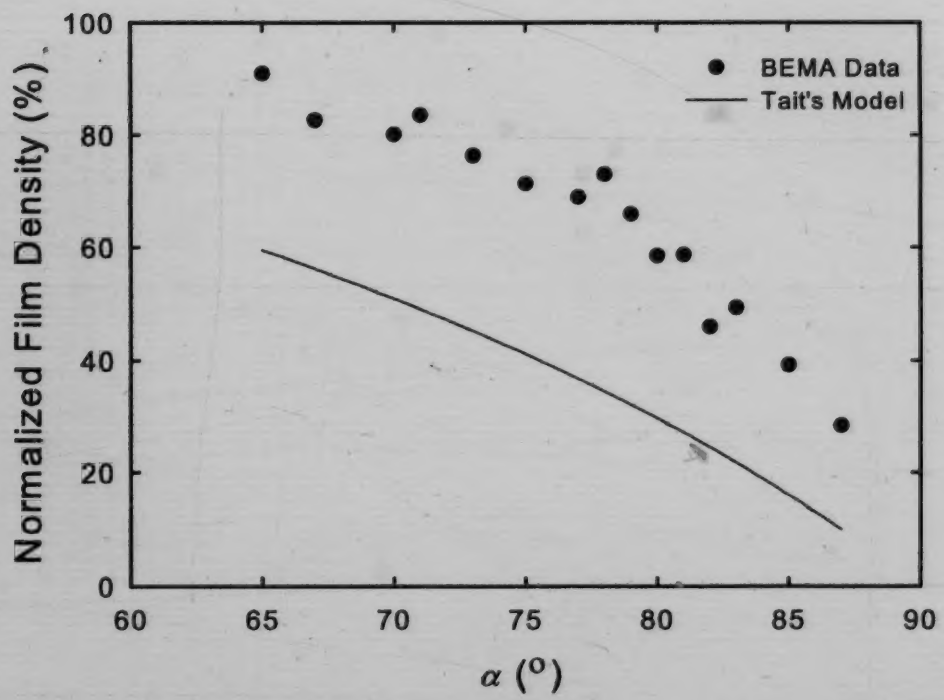

Figure 4.15: Normalized film density of the biaxial layer as a function of the deposition angle α. The density predicted based on Tait's rule (solid line) is shown as a guideline.

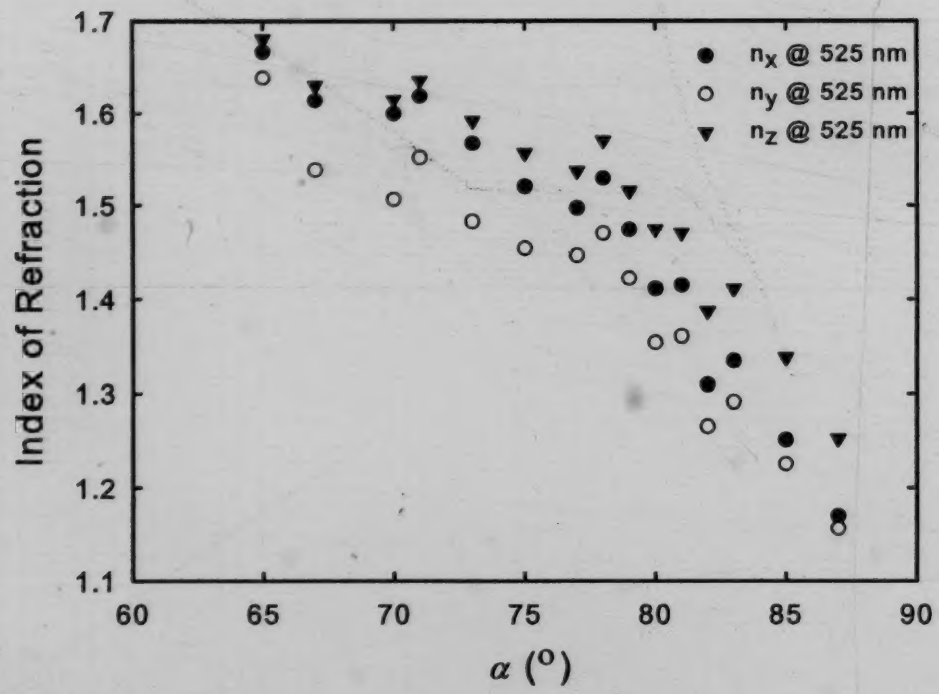

Figure 4.16: The principal indices of refraction for the biaxial layer of Alq_3 at a wavelength of 525 nm.

4.3.3 Birefringence of Alq_3 columnar thin films

Fig. 4.17 shows the calculated Δn as a function of deposition angle. At deposition angles $\alpha > 70°$, a larger index of refraction in the direction parallel to the deposition plane is measured than perpendicular to the deposition plane ($n_p > n_x$). This negative in-plane birefringence is opposite to the values previously seen in biaxial film studies of inorganic thin films [1, 73, 81, 82]. The magnitude of the birefringence showed a generally increasing trend as the deposition angle increased, with a maximum negative birefringence of 0.073 ± 0.002 obtained for the film deposited at 85°. The negative value of the in-plane birefringence is due largely to the predominantly circular cross-section of individual Alq_3 columns in the direction of column growth, illustrated in Fig. 4.18. The Alq_3 columns have diameters in the approximate range of 60 nm to 75 nm which remain constant throughout the thickness of the biaxial film layer. The columns do not exhibit the common broadening effects that are present in inorganic GLAD films. The circular cross-sections cause the variation of the post cross-sectional geometry in the substrate plane to vary as a function of the column tilt angle β. A greater column tilt causes an increase in the length of the major elliptical axis of the columns in the substrate plane whereas the length of the minor elliptical axis perpendicular to the deposition plane remains unchanged and equal to the post diameter, as shown in Fig. 4.19.

The in-plane anisotropy varies due to the form birefringence of the column cross-sections. As the deposition angle decreases and the overall film density increases, the individual post morphology deteriorates as the individual columnar posts begin to chain together with their neighbouring posts and coalesce, causing the circular cross-sections to merge and a secondary anisotropy to occur in the film perpendicular to the deposition plane (Fig. 4.20). This phenomenon causes a change in the form birefringence similar to column broadening seen in inorganic GLAD films, resulting in a decrease in the number of voids between columns and thus an increase in the refractive index perpendicular to the deposition plane. This leads to the positive in-plane birefringence values observed in Fig. 4.17 for $\alpha < 70°$. However, the column chaining seen in Alq_3 biaxial thin films did not cause growth competition or column extinction which are prevalent in inorganic column broadening. The column melding effect was more prevalent at lower deposition angles

and coupled with the smaller column tilt angle reduced the negative in-plane birefringence. This was observed to be largest in the films deposited at 67° and 70° which measured the largest positive birefringence values. The maximum in-plane positive birefringence occurs at a similar angle to that observed for inorganic biaxial thin films [81, 82].

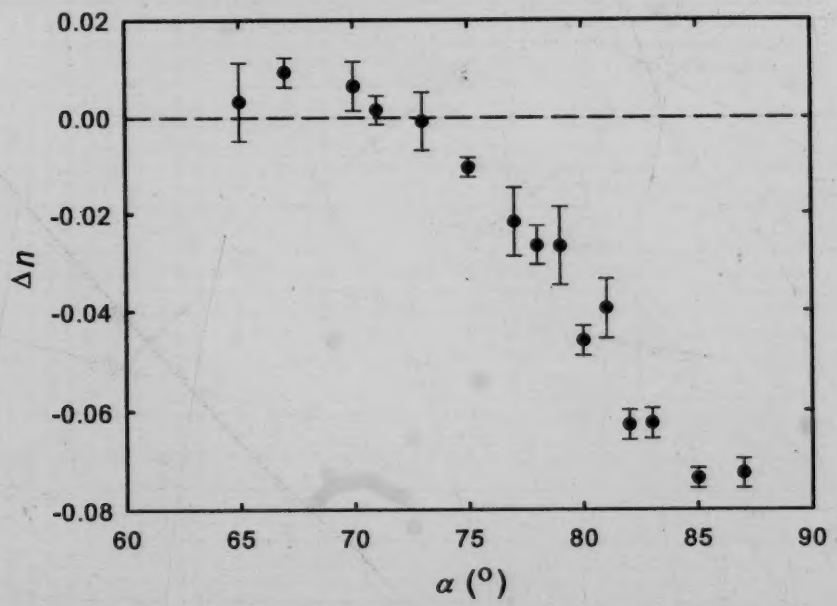

Figure 4.17: In-plane birefringence, Δn, shown as a function of deposition angle α.

At the start of the chapter, it was mentioned that the the magnitude of the circular Bragg effect in chiral films increased at higher deposition angles which in turn causes an increase in the selective transmittance of circularly polarized light in helical thin films [53]. This effect was predicted to vary with the square of Δn, the birefringence [81]. The premise of the investigation described in this chapter was to investigate the fundamental properties of Alq_3 columnar thin films and determine the relationship between the birefringence and the deposition angle in order to verify the prediction. Fig. 4.21 compares the peak selective transmittance of circularly polarized light (T_{LCP}-T_{RCP}) from 5 turn helical films deposited at α >75° [53] and the birefringence squared (Δn^2) of slanted post films at various deposition angles. Both sets of data show a similar trend of increasing magnitude as the deposition angle increases, thus providing a reasonable confirmation of the expected behavior.

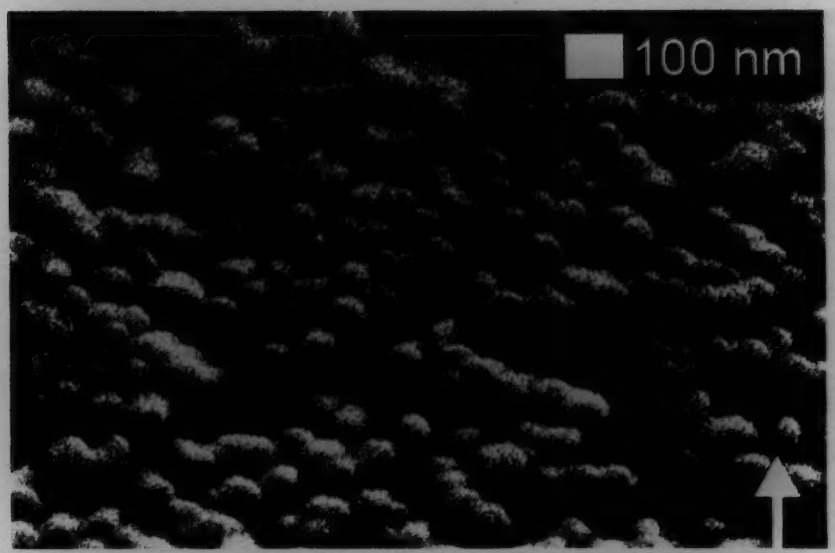

Figure 4.18: SEM of the film deposited at $\alpha = 85°$ as viewed along the direction of the columns. The white arrow indicates the direction of the incoming vapour flux. As can be seen, the column cross-sections are predominantly circular in shape.

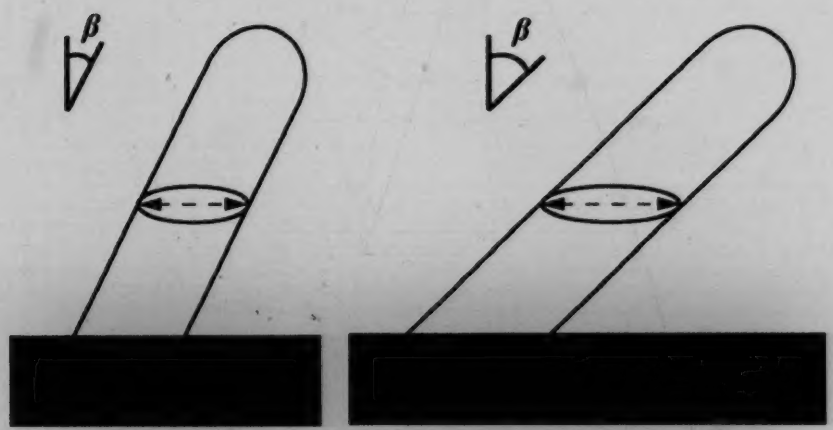

Figure 4.19: Illustration of the change in the major elliptical cross-section diameter as the column tilt is increased. The minor elliptical cross-section diameter is equal to the columnar post diameter and thus remains unchanged as the column tilt varies.

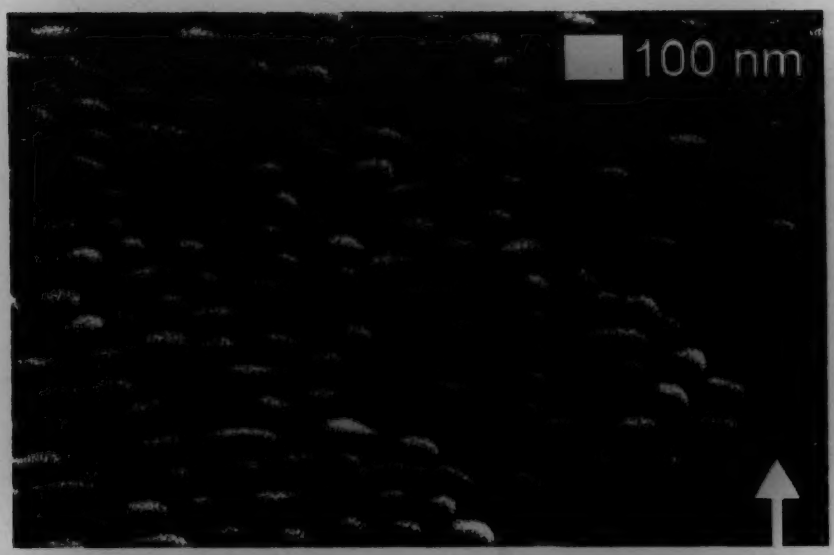

Figure 4.20: SEM of the film deposited at $\alpha = 67°$ along the direction of the post growth. The white arrow indicates the direction of the incoming vapour flux. Individual columns have merged together modifying the cross-section of the columns and decreasing the number of voids.

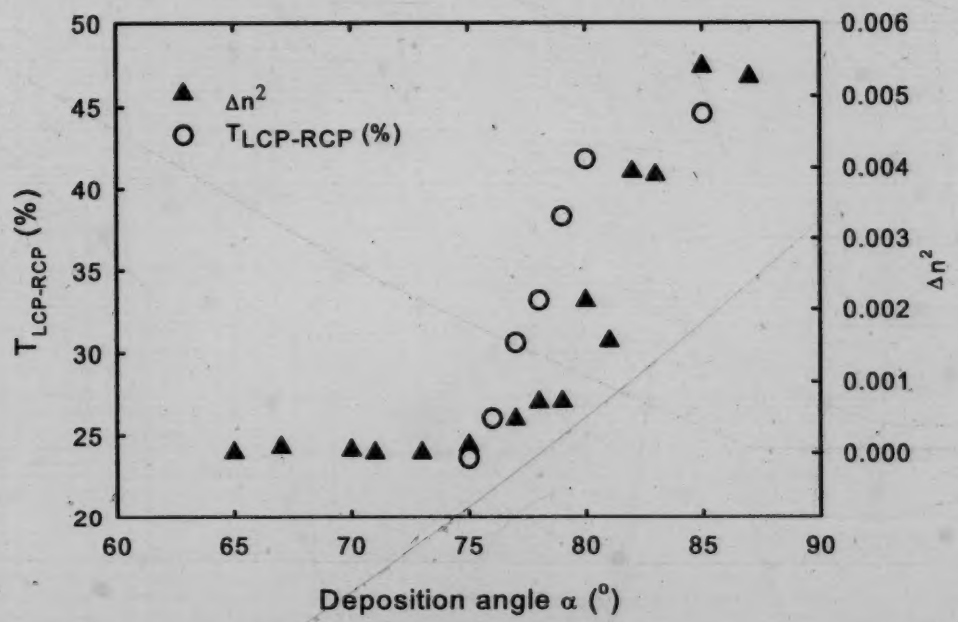

Figure 4.21: Plot of the peak selective transmittance of circularly polarized light from 5 turn helical films and the birefringence squared (Δn^2) of slanted post films at various deposition angles.

4.4 Summary

Porous biaxial thin films composed of organic Alq_3 slanted columnar posts have been fabricated and characterized using variable angle spectroscopic ellipsometry and the Bruggeman effective medium approximation. The Alq_3 films exhibited expected column angle and density behaviour in relation to the deposition angle. A negative in-plane birefringence has been achieved in GLAD thin films which is contrary to the values typically observed in inorganic materials. Negative in-plane birefringence has been achieved due to the predominantly circular cross-section of the Alq_3 columnar posts that control the form birefringence as a function of the column tilt, without the detriment of secondary anisotropic effects such as column broadening and fanning. The magnitude of the birefringence behaved as predicted with respect to the deposition angle as the magnitude of the birefringence squared exhibited a similar increasing trend as the one observed in the selective transmittance of circularly polarized light in chiral films. Knowledge of the optical parameters of Alq_3 is critical to designing and modelling of proposed nanostructured devices incorporating porous architectures using GLAD.

Chapter 5

Optical and structural comparison of quinoline metal chelate thin films

Although the tris-chelate Alq_3 has been been studied most extensively, as described in previous chapters, the many derivatives of Alq_3 have also been investigated as possible high efficiency emitter materials. These studies tended to focus on the electroluminescent and fluorescence properties of these materials in order to explore their potential for better OLED materials. Derivatives of Alq_3 are formed by substituting the central metal aluminum ion with other trivalent or bivalent metals or substituting the 8-hydroxyquionline ligand [45, 48, 51, 95]. Alq_3 was the first nanostructured organic GLAD film to be produced by direct deposition and showed many unique characteristics not typically seen in inorganic GLAD films [12]. To determine whether these features were limited to the one organic material due to the chemical composition or molecular geometry, thin films composed of tris(8-hydroxyquinoline) gallium (Gaq_3) and bis(8-hydroxyquinoline) zinc (Znq_2) were fabricated and characterized. Preliminary investigation into organic GLAD with other materials consisted of fabricating three films composed of each material: a solid thin film, a slanted columnar thin film, and a 5 turn helical film.

5.1 Basic properties

Gaq_3 has the same tris-chelate arrangement as Alq_3 but contains the heavier gallium metal in the center and thus a higher molecular mass and stronger covalent bond between the metal-ligand bonding (primarily between the metal and nitrogen atoms) [46]. Znq_2, in contrast, has only two hydoxyquinoline ligands. Fig. 5.1 shows the chemical structure of

the two molecules while Table 5.1 compares the molecular and luminescent properties of the materials with Alq_3.

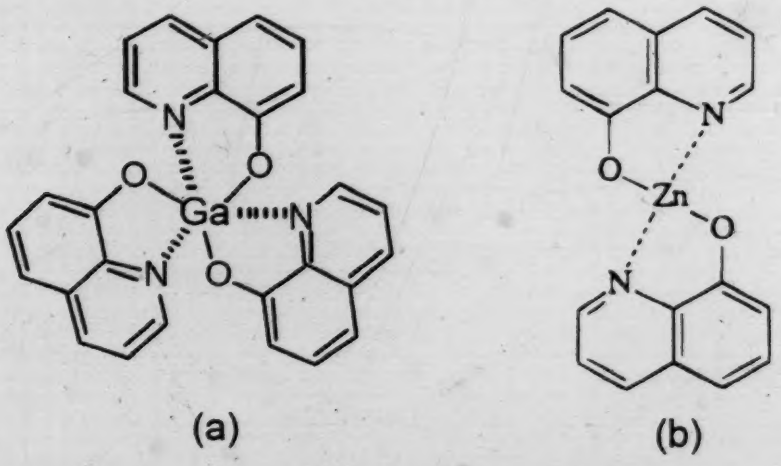

Figure 5.1: Molecular structure of a (a) tris(8-hydroyquinoline) gallium (Gaq_3) molecule and (b) a bis(8-hydroyquinoline) zinc (Znq_2) molecule.

Table 5.1: Properties of quinoline metal chelates.

	Alq_3	Gaq_3	Znq_2
Molecular weight	459.44	502.18	353.68
Formula	$C_{27}H_{18}N_3O_3Al$	$C_{27}H_{18}N_3O_3Ga$	$C_{18}H_{12}N_2O_2Zn$
Melting point	418°C	409°C	356°C
Photoluminescence peak	520 nm [45] 519 nm [48]	541 nm [45]	542 nm [48] 535, 567 nm [95]
Electroluminescence peak	532 nm [45]	535 nm [45]	568 nm [95]

5.2 Index of refraction of solid films

The optical constant profiles are necessary parameters used to model and analyze obliquely deposited thin films. To measure these profiles, solid Gaq_3 and Znq_2 thin films were grown at $\alpha = 0°$ and optically characterized using the variable angle spectroscopic ellipsometer in a similar manner as described in Chapter 4. Scans were performed over the wavelength range of 300 nm to 1300 nm for angles of light incidence of 20°, 40°, 60°, and 80° with respect to substrate normal. The normally deposited film was then modelled optically using a Lorentz and Tauc-Lorentz oscillator system. The optical constant profiles of Gaq_3 and

Znq_2 are shown in Fig. 5.2, with the profile of Alq_3 included for comparison. The optical behavior of all three quinoline materials is similar across the measured wavelengths in both the real and imaginary components of the index of refraction. The values obtained for Znq_2 are comparable with the values measured in a previous study which measured an approximate maximum peak real index value of 1.9 at 420 nm and imaginary index value of 1.35 at 380 nm [96], however the optical profile of Gaq_3 could not be compared as no other studies measuring this property of Gaq_3 were found in literature.

5.3 Comparison of nanostructured quinoline films

A slanted post columnar thin film and a 5 turn helical thin film were deposited for each quinoline material to compare the optical and structural properties of the nanostructured films. The slanted post films (Fig. 5.3) were analyzed using SEM, variable angle spectroscopic ellipsometry, and the Bruggeman effective medium approximation, as described in Chapter 4. The biaxial thin film model provided the column tilt, density and principal indices of refraction which are summarized in Table 5.2. Structures of both quinoline materials exhibited the same characteristic smoothness and lack of column broadening seen in Alq_3. The Gaq_3 nanostructures had a slightly smaller column diameter (60 nm - 70 nm) than the Alq_3 nanostructures (70 nm - 75 nm) while the Znq_2 structures had half the column diameter of the tris(8-hydroxyquinoline) nanostructures, at 30 nm - 35 nm. The reasons for the variation in the column diameter are unknown.

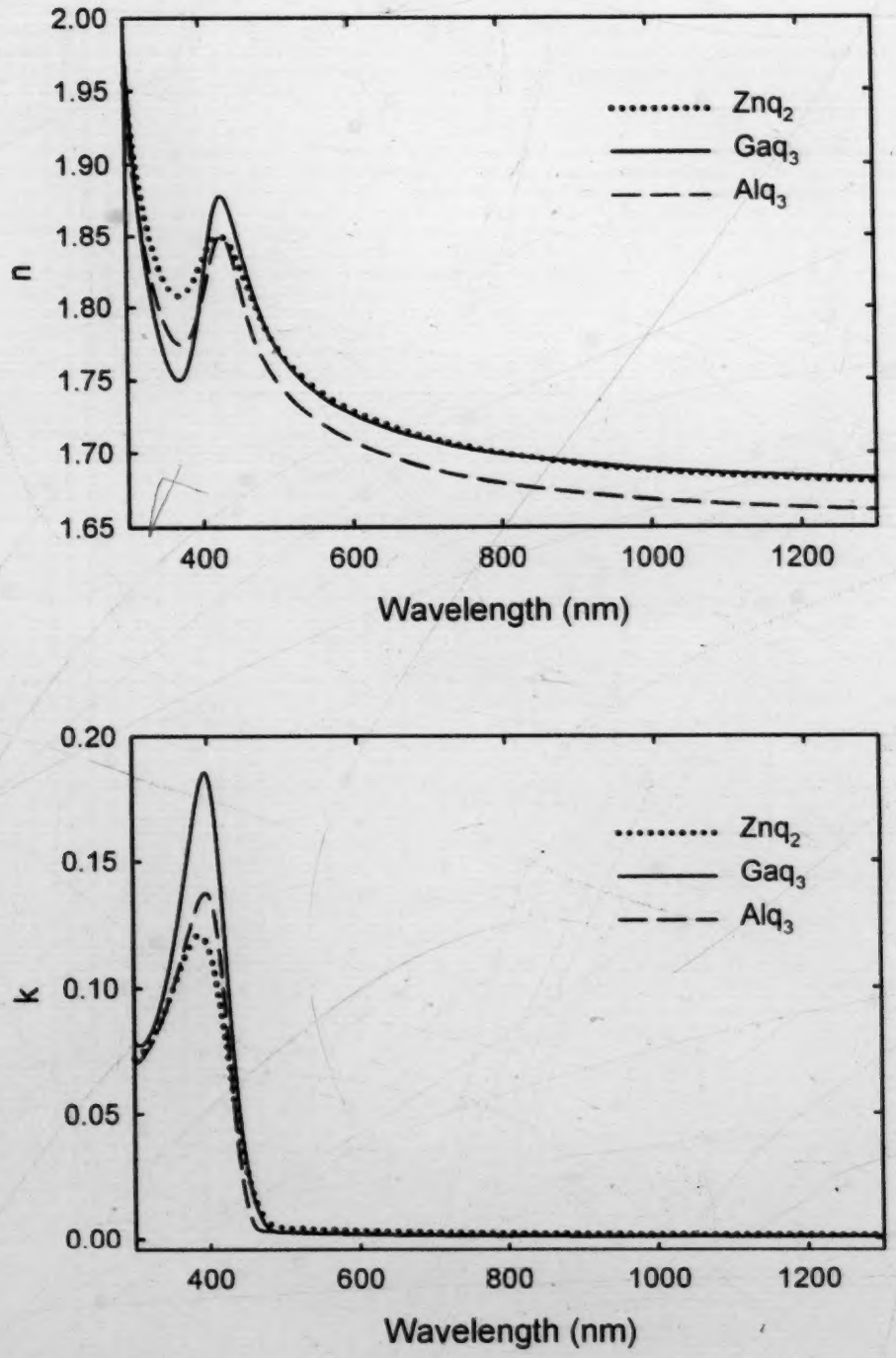

Figure 5.2: Measured real and imaginary parts of the index of refraction of Znq_2, Gaq_3, and Alq_3.

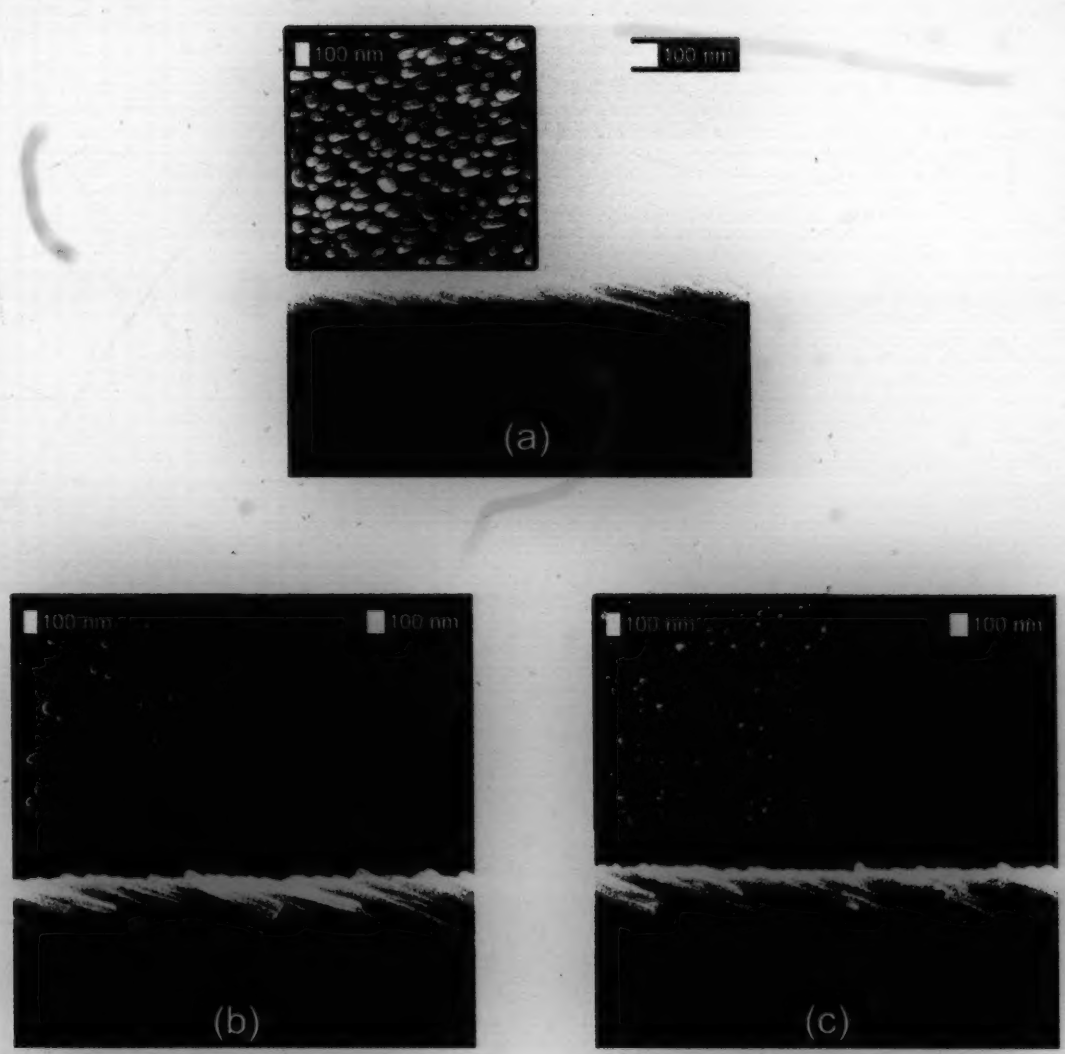

Figure 5.3: Slanted post columnar thin films deposited at $\alpha = 80°$ composed of (a) Alq_3, (b) Gaq_3, and (c) Znq_2. Insets are top down views.

Table 5.2: Comparison of quinoline metal chelates slanted columnar thin films deposited at $\alpha = 80°$.

	Alq_3	Gaq_3	Znq_2
Column Diameter ($\pm$ 4 nm)	70-75	60-70	30-35
Column tilt β (°)	69.3	65.6	65.6
Density (%)	58.5	58.7	49.6
n_{solid}	1.734	1.754	1.756
n_x	1.412	1.419	1.359
n_y	1.353	1.368	1.290
n_z	1.458	1.490	1.425
n_p	1.458	1.467	1.400
$\Delta n = n_x - n_p$	-0.046	-0.048	-0.043

All indices measured at 525 nm

5.3.1 Circular polarization

The circular polarization behavior of the helical samples (Fig. 5.4) were measured by the transmission of light through the film using the VASE [53]. The transmittance and Mueller matrix of each sample was used to determine the transmittance of left-handed circularly polarized light (T_{LCP}) and right-handed circularly polarized light (T_{RCP}) through the chiral medium [5]. Fig. 5.5 shows the transmission spectra of the quinoline helices. The helical pitch of the films varied slightly measuring 305 nm for the Alq_3 film, 311 nm for the Gaq_3 film, and 335 nm for the Znq_2 film. This variation in the helical pitch accounts for the difference in the peak selective transmittance ($T_{LCP-RCP}$) observed since it is centered at $\lambda = n_{avg}$p, where n_{avg} is the average index of refraction of the medium and p is the helical pitch [5,26,97]. The modelled birefringence values using slanted columnar posts show that all three films should theoretically have very similar birefringence values for each material. A decrease in the magnitude of selective transmission is observed among the three films where $Alq_3 > Gaq_3 > Znq_2$, however the magnitude of the peak selective transmission is still larger than values obtained from inorganic GLAD films [78]. This difference in selective transmission intensity is hypothesized to be due to the increased scattering effects caused by the reduction in the nanostructure column diameter. This increases the number scattering centers in a manner similar to the effects observed in annealed titanium dioxide GLAD films [98]. The phenomenon is not explored further in the studies discussed here.

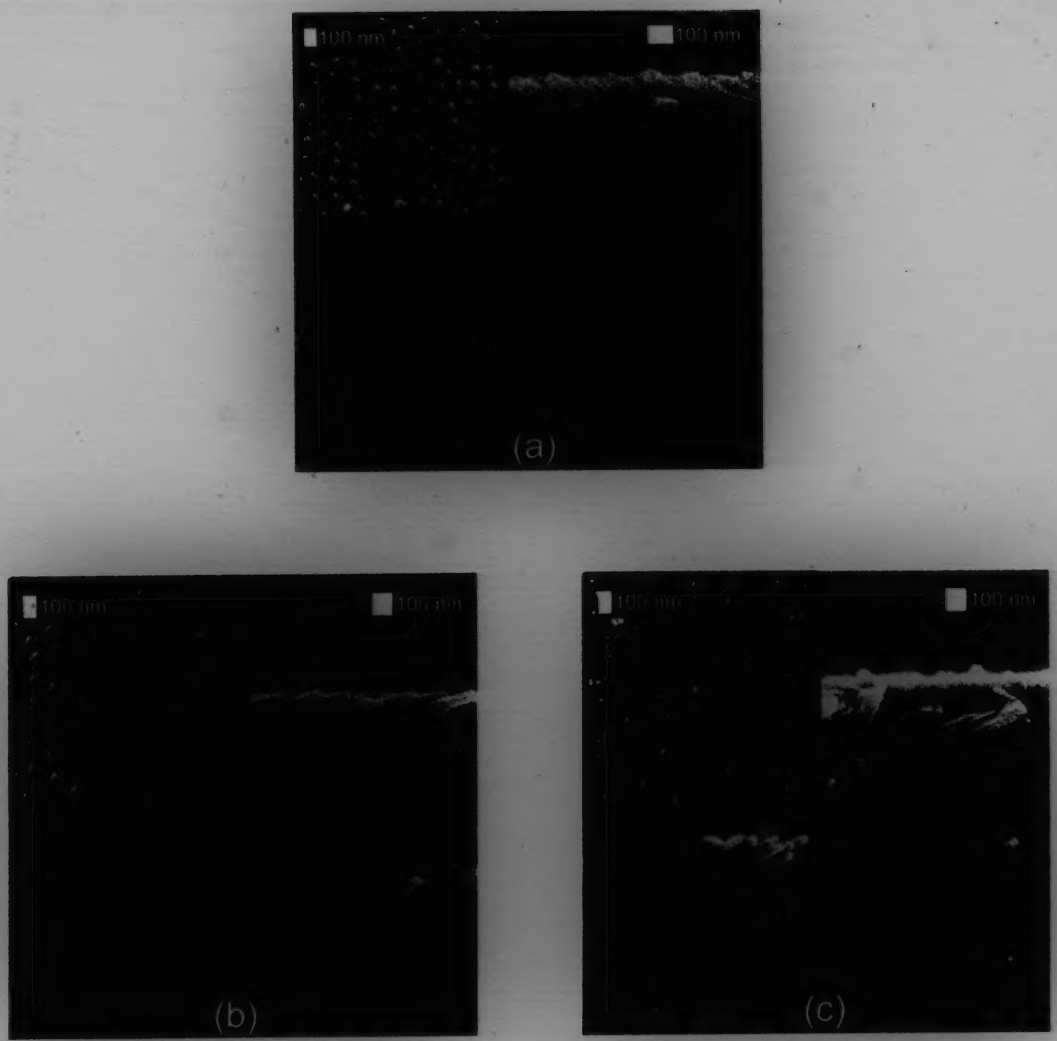

Figure 5.4: 5 turn right-handed helical thin films deposited at $\alpha = 80°$ composed of (a) Alq_3, (b) Gaq_3, and (c) Znq_2. Insets are top down views.

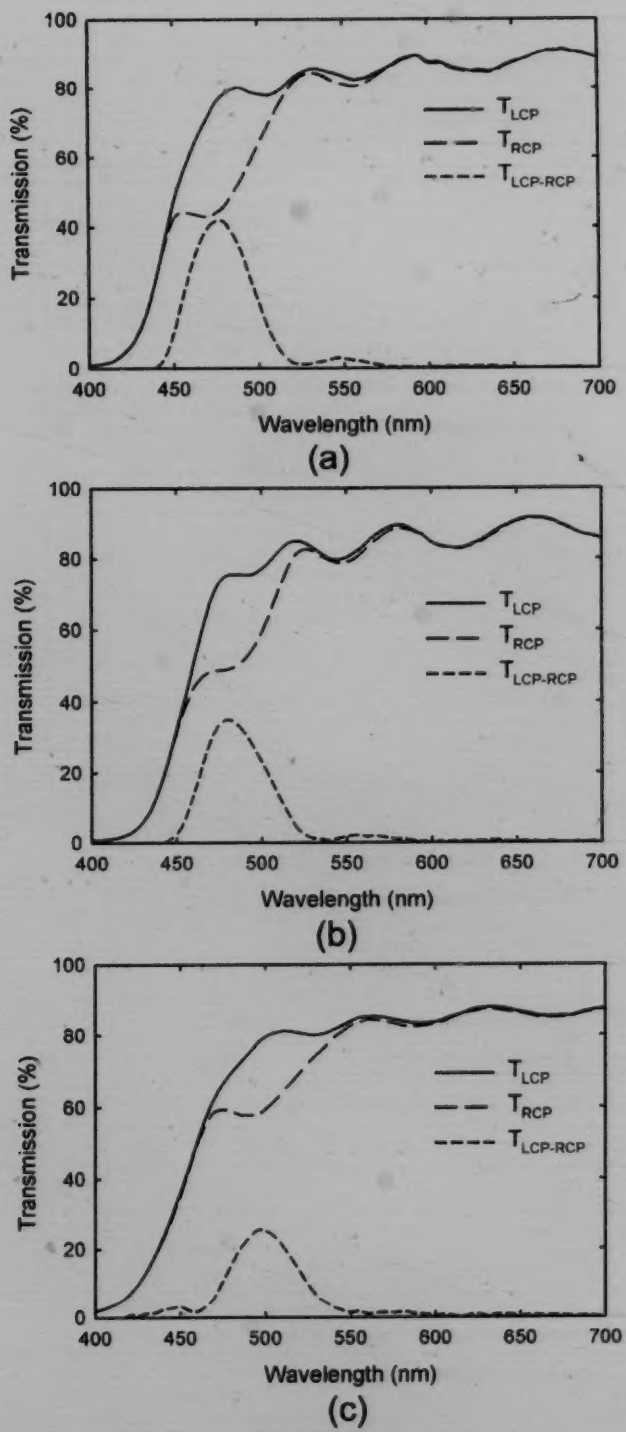

Figure 5.5: Transmission through a 5 turn, right-handed helical GLAD Film deposited $\alpha = 80°$ composed of (a) Alq_3, (b) Gaq_3, and (c) Znq_2.

As previously mentioned in Chapter 2, attempts to fabricate Alq_3 vertical posts by decreasing the helical pitch were unsuccessful. The same multiple rotation chuck was utilized to fabricate Znq_2 helices with different pitches (Fig. 5.6). The Znq_2 behaved in a similar manner to the Alq_3. At smaller helical pitches the material tends to form clumps until it transitions to a stage where the pitch is large enough for the columnar structure to become defined. Since the Znq_2 has a smaller preferential nucleation size and forms nanostructures with smaller diameter columns than the Alq_3, the pitch where the transition to defined helices was also lower, between 30 nm - 90 nm.

Figure 5.6: Examples of Znq_2 helices with pitches of (a) 30 nm and (b) 90 nm. Insets are top down views.

5.4 Summary

Nanostructured metal chelate thin films composed of Gaq_3 and Znq_2 have been fabricated using GLAD. The quinline compounds both exhibited the same nanostructured smoothness and lack of broadening observed in Alq_3 films. The optical properties of the slanted post and helical films were characterized and were similar to their Alq_3 counterparts. The successful fabrication of various organic GLAD thin films demonstrates that small molecule quinolines are certainly suitable for nanostructured thin films. However, the potential exists for the vast multitude of other organic materials to be tailored for specific properties and deposited using GLAD for various potential applications ranging from solar cells and optical displays to organic lasers and molecular electronics.

Chapter 6

Conclusions and recommendations for future work

6.1 Conclusions

This thesis has presented the characterization of quinoline metal chelate thin films deposited by glancing angle deposition. Thin films composed of Alq_3, Gaq_3, and Znq_2 were fabricated and characterized to determine their optical and structural properties, with the primary investigation centered on Alq_3. A large range of nanostructured thin film morphologies can be fabricated using these materials through GLAD, however this work primarily focused on characterizing three basic morphologies: solid, slanted columnar post, and helical thin films. Quinoline GLAD films exhibited several distinct characteristics that were not typically observed in inorganic GLAD thin films. The organic films did not suffer the deleterious broadening effects commonly observed in inorganic materials and the individual nanostructures appeared remarkably smooth under SEM. The individual structures had predominantly circular cross-sections, typically 70 nm - 75 nm in diameter. Another interesting feature of the quinoline thin films was the formation of a solid layer of material prior to the nanostructured growth formation. The influence of the deposition parameters on the wetting layer was studied in conjunction with organosiloxane derivatized silicon substrates to also determine the effects of surface hydrophobicity via substrate functionalization for Alq_3. It was revealed that certain deposition parameters had a positive effect on decreasing the wetting layer thickness. Larger deposition angles of incidence and higher material deposition rates both reduced the wetting layer thickness. It was also shown that the wetting layer formation was strongly dependent on the substrate surface

hydrophobicity. From these investigations, the ability to tailor the wetting layer thickness of Alq_3 is now possible.

The optical properties and structural properties of nanostructured quinoline thin films have been characterized using scanning electron microscopy, variable angle spectroscopic ellipsometry, and the Bruggeman effective medium approximation. A set of Alq_3 slanted post thin films deposited at varying angles of incidence were fabricated and studied to determine the column tilt of the structures, film density, and principal indices of refraction. The column tilt angle increased as the deposition angle increased, as expected, although the magnitude of the tilt was larger than the values predicted by Tait's geometrically derived rule. This is interesting to note since most inorganic tilted columnar thin films have lower column tilt values than those predicted by Tait's rule. The accuracy of the modelled Alq_3 column tilt angles were confirmed by comparisons to the values obtained from SEM images of the films. The thin film density and principal indices both exhibited typical GLAD behavior and decreased as the deposition angle increased. However, an interesting phenomenon was observed in the in-plane birefringence which is a function of the indices. The typical inorganic GLAD films has a positive in-plane birefringence, where the index of refraction perpendicular to the deposition plane is larger that the index parallel to the deposition plane. In the Alq_3 films, the opposite effect was observed at deposition angles larger than 70°. This negative in-plane birefringence was due to a combination of factors which affect the form birefringence including the higher column tilt, lack of broadening, and predominantly circular cross-sections in the nanostructures. Nanostructured films fabricated using Gaq_3 and Znq_2 were observed to have similar optical and structural properties as Alq_3. The main difference between films composed of the different materials was the nanostructure column diameters which was typically 60 nm - 70 nm for the Gaq_3 and 30 nm - 35 nm for the Znq_2.

The ability to fabricate organic nanostructures and have the films tailored for specific properties is an important step in the realization of devices. This study focused on quinoline metal chelates which are organic light emitting materials and examined their properties. Knowledge of the optical and structural properties of these films is the first step

in modelling and designing thin film architectures in future applications.

6.2 Recommendations for future work

6.2.1 Investigations of other organic materials

The potential for organic nanostructured GLAD films is tremendous given the vast range of available deposition materials. Quinoline molecules are only one of the many available and commonly used small molecule organic materials available. Areas where small molecule organics are used and may benefit from the unique advantages of GLAD thin films such as the high surface area include OLEDs, solar cells, and biological systems where nanostructured biological molecules may be useful for drug delivery and sensing applications. Recent work has investigated the formation of arrays of crystalline C_{60} and pentacene nanocolumns using GLAD [99].

6.2.2 Fundamental studies

One deposition parameter not studied in this work was the effect of substrate temperature. The impact of substrate cooling on film formation and wetting layer thickness should be investigated in future work. Previous work has looked at the impact of substrate temperature on initial growth and formation [100, 101] and may provide insight into how the films grow. A lower substrate temperature may further reduce the molecular mobility of the incoming molecules and should decrease the wetting layer thickness. The ability to cool the substrate during deposition may also prove useful when depositing with source materials with lower glass transition temperatures. Studies into the initial growth prior to the wetting layer formation of the organics may be of interest to better understand the growth mechanics of these materials. While these studies have been performed using Alq_3, they are limited to standard normal angles of incidence and do not encompass the GLAD regime. There are also additional fundamental studies into the properties of the quinoline films that have yet to be explored including additional work on the cause of the wetting layer formation. At this point in time, the z-density values for Alq_3, Gaq_3, and Znq_2 are not known as are the values for most organic materials.

Bibliography

[1] T. Motohiro and Y. Taga, "Thin-film retardation plate by oblique deposition," *Applied Optics*, vol. 28, no. 13, pp. 2466–2482, 1989.

[2] J. M. Nieuwenhuizen and H. B. Haanstra, "Microfractography of thin films," *Philips Technical Review*, vol. 27, no. 3-4, pp. 87–91, 1966.

[3] H. van Kranenburg and C. Lodder, "Tailoring growth and local composition by oblique-incidence deposition - a review and new experimental-data," *Materials Science and Engineering R-Reports*, vol. 11, no. 7, pp. 295–354, 1994.

[4] B. Dick, M. J. Brett, T. J. Smy, M. R. Freeman, M. Malac, and R. F. Egerton, "Periodic magnetic microstructures by glancing angle deposition," *Journal of Vacuum Science and Technology A-Vacuum Surfaces and Films*, vol. 18, no. 4, pp. 1838–1844, 2000.

[5] A. C. van Popta, M. J. Brett, and J. C. Sit, "Double-handed circular bragg phenomena in polygonal helix thin films," *Journal of Applied Physics*, vol. 98, no. 8, p. 083517, 2005.

[6] D. Vick and M. J. Brett, "Conduction anisotropy in porous thin films with chevron microstructures," *Journal of Vacuum Science and Technology A*, vol. 24, no. 1, pp. 156–164, 2006.

[7] K. Robbie and M. J. Brett, "Method of depositing shadow sculpted thin films," 1999.

[8] K. Robbie, M. J. Brett, and A. Lakhtakia, "Chiral sculptured thin films," *Nature*, vol. 384, no. 6610, pp. 616–616, 1996.

[9] I. Hodgkinson and Q. H. Wu, "Serial bideposition of anisotropic thin films with enhanced linear birefringence," *Applied Optics*, vol. 38, no. 16, pp. 3621–3625, 1999.

[10] I. Hodgkinson, Q. H. Wu, L. De Silva, and M. Arnold, "Inorganic positive uniaxial films fabricated by serial bideposition," *Optics Express*, vol. 12, no. 16, pp. 3840–3847, 2004.

[11] A. L. Elias, K. D. Harris, C. W. M. Bastiaansen, D. J. Broer, and M. J. Brett, "Large-area microfabrication of three-dimensional, helical polymer structures," *Journal of Micromechanics and Microengineering*, vol. 15, no. 1, pp. 49–54, 2005.

[12] P. C. P. Hrudey, K. L. Westra, and M. J. Brett, "Highly ordered organic alq3 chiral luminescent thin films fabricated by glancing-angle deposition," *Advanced Materials*, vol. 18, no. 2, pp. 224–228, 2006.

[13] M. Ohring, *Materials science of thin films*. Academic Press, 2 ed., 2002.

[14] H. Hertz *Ann. Physik.*, vol. 17, p. 177, 1882.

[15] B. A. Movchan and Demchish.Av, "Study of structure and properties of thick vacuum condensates of nickel, titanium, tungsten, aluminium oxide and zirconium dioxide," *Physics of Metals and Metallography-Ussr*, vol. 28, no. 4, pp. 83–90, 1969.

[16] J. A. Thornton, "High-rate thick-film growth," *Annual Review of Materials Science*, vol. 7, pp. 239–260, 1977.

[17] R. Messier, A. P. Giri, and R. A. Roy, "Revised structure zone model for thin-film physical structure," *Journal of Vacuum Science and Technology A-Vacuum Surfaces and Films*, vol. 2, no. 2, pp. 500–503, 1984.

[18] R. Messier, "Toward quantification of thin-film morphology," *Journal of Vacuum Science and Technology A-Vacuum Surfaces and Films*, vol. 4, no. 3, pp. 490–495, 1986.

[19] L. Abelmann and C. Lodder, "Oblique evaporation and surface diffusion," *Thin Solid Films*, vol. 305, no. 1-2, pp. 1–21, 1997.

[20] R. N. Tait, T. Smy, and M. J. Brett, "Modeling and characterization of columnar growth in evaporated films," *Thin Solid Films*, vol. 226, no. 2, pp. 196–201, 1993.

[21] K. D. Harris, A. Huizinga, and M. J. Brett, "High-speed porous thin film humidity sensors," *Electrochemical and Solid State Letters*, vol. 5, no. 11, pp. H27–H29, 2002.

[22] J. J. Steele, A. C. van Popta, M. M. Hawkeye, J. C. Sit, and M. J. Brett, "Nanostructured gradient index optical filter for high-speed humidity sensing," *Sensors and Actuators B-Chemical*, vol. 120, no. 1, pp. 213–219, 2006.

[23] K. D. Harris, D. Vick, E. J. Gonzalez, T. Smy, K. Robbie, and M. J. Brett, "Porous thin films for thermal barrier coatings," *Surface and Coatings Technology*, vol. 138, no. 2-3, pp. 185–191, 2001.

[24] S. R. Kennedy, M. J. Brett, O. Toader, and S. John, "Fabrication of tetragonal square spiral photonic crystals," *Nano Letters*, vol. 2, no. 1, pp. 59–62, 2002.

[25] M. O. Jensen and M. J. Brett, "Periodically structured glancing angle deposition thin films," *IEEE Transactions on Nanotechnology*, vol. 4, no. 2, pp. 269–277, 2005.

[26] A. C. van Popta, M. M. Hawkeye, J. C. Sit, and M. J. Brett, "Gradient-index narrow-bandpass filter fabricated with glancing-angle deposition," *Optics Letters*, vol. 29, no. 21, pp. 2545–2547, 2004.

[27] K. Kaminska, T. Brown, G. Beydaghyan, and K. Robbie, "Vacuum evaporated porous silicon photonic interference filters," *Applied Optics*, vol. 42, no. 20, pp. 4212–4219, 2003.

[28] S. R. Kennedy and M. J. Brett, "Porous broadband antireflection coating by glancing angle deposition," *Applied Optics*, vol. 42, no. 22, pp. 4573–4579, 2003.

[29] M. O. Jensen and M. J. Brett, "Porosity engineering in glancing angle deposition thin films," *Applied Physics A-Materials Science and Processing*, vol. 80, no. 4, pp. 763–768, 2005.

[30] M. O. Jensen and M. J. Brett, "Square spiral 3d photonic bandgap crystals at telecommunications frequencies," *Optics Express*, vol. 13, no. 9, pp. 3348–3354, 2005.

[31] K. Robbie, G. Beydaghyan, T. Brown, C. Dean, J. Adams, and C. Buzea, "Ultrahigh vacuum glancing angle deposition system for thin films with controlled three-dimensional nanoscale structure," *Review of Scientific Instruments*, vol. 75, no. 4, pp. 1089–1097, 2004.

[32] M. M. Hawkeye and M. J. Brett, "Narrow bandpass optical filters fabricated with one-dimensionally periodic inhomogeneous thin films," *Journal of Applied Physics*, vol. 100, no. 4, pp. –, 2006.

[33] T. A. Savas, M. Farhoud, H. I. Smith, M. Hwang, and C. A. Ross, "Properties of large-area nanomagnet arrays with 100 nm period made by interferometric lithography," *Journal of Applied Physics*, vol. 85, no. 8, pp. 6160–6162, 1999.

[34] B. Dick, J. C. Sit, M. J. Brett, I. M. N. Votte, and C. W. M. Bastiaansen, "Embossed polymeric relief structures as a template for the growth of periodic inorganic microstructures," *Nano Letters*, vol. 1, no. 2, pp. 71–73, 2001.

[35] B. Dick, M. J. Brett, T. Smy, M. Belov, and M. R. Freeman, "Periodic submicrometer structures by sputtering," *Journal of Vacuum Science and Technology B*, vol. 19, no. 5, pp. 1813–1819, 2001.

[36] M. Colle and W. Brutting, "Thermal, structural and photophysical properties of the organic semiconductor alq(3)," *Physica Status Solidi A-Applied Research*, vol. 201, no. 6, pp. 1095–1115, 2004.

[37] S. E. Wiberley and L. G. Bassett, "Colorimetric determination of aluminum in steel - use of 8-hydroxyquinoline," *Analytical Chemistry*, vol. 21, no. 5, pp. 609–612, 1949.

[38] E. Goon, J. E. Petley, W. H. Mcmullen, and S. E. Wiberley, "Fluorometric determination of aluminum - use of 8-quinolinol," *Analytical Chemistry*, vol. 25, no. 4, pp. 608–610, 1953.

[39] D. C. Freeman and C. E. White, "The structure and characteristics of the fluorescent metal chelates of ortho,ortho-'-dihydroxyazo compounds," *Journal of the American Chemical Society*, vol. 78, no. 12, pp. 2678–2682, 1956.

[40] C. W. Tang and S. A. Van Slyke, "Organic electroluminescent diodes," *Appl. Phys. Lett.*, vol. 51, no. 12, pp. 913–915, 1987.

[41] J. R. Sheats, H. Antoniadis, M. Hueschen, W. Leonard, J. Miller, R. Moon, D. Roitman, and A. Stocking, "Organic electroluminescent devices," *Science*, vol. 273, no. 5277, pp. 884–888, 1996.

[42] S. A. VanSlyke, C. H. Chen, and C. W. Tang, "Organic electroluminescent devices with improved stability," *Applied Physics Letters*, vol. 69, no. 15, pp. 2160–2162, 1996.

[43] F. Papadimitrakopoulos, X.-M. Zhang, D. L. Thomsen, and K. A. Higginson, "A chemical failure mechanism for aluminum(iii) 8-hydroxyquinoline light-emitting devices," *Chemisty of Materials*, vol. 8, pp. 1363–1365, 1996.

[44] M. Colle, J. Gmeiner, W. Milius, H. Hillebrecht, and W. Brutting, "Preparation and characterization of blue-luminescent tris(8-hydroxyquinoline) aluminum (alq(3))," *Advanced Functional Materials*, vol. 13, no. 2, pp. 108–112, 2003.

[45] P. E. Burrows, L. S. Sapochak, D. M. Mccarty, S. R. Forrest, and M. E. Thompson, "Metal-ion dependent luminescence effects in metal tris-quinolate organic heterojunction light-emitting devices," *Applied Physics Letters*, vol. 64, no. 20, pp. 2718–2720, 1994.

[46] C. H. Chen and J. M. Shi, "Metal chelates as emitting materials for organic electroluminescence," *Coordination Chemistry Reviews*, vol. 171, pp. 161–174, 1998.

[47] R. Ballardini, G. Varani, M. T. Indelli, and F. Scandola, "Phosphorescent 8-quinolinol metal-chelates - excited-state properties and redox behavior," *Inorganic Chemistry*, vol. 25, no. 22, pp. 3858–3865, 1986.

[48] T. A. Hopkins, K. Meerholz, S. Shaheen, M. L. Anderson, A. Schmidt, B. Kippelen, A. B. Padias, H. K. Hall, N. Peyghambarian, and N. R. Armstrong, "Substituted aluminum and zinc quinolates with blue-shifted absorbance/luminescence bands: Synthesis and spectroscopic, photoluminescence, and electroluminescence characterization," *Chemistry of Materials*, vol. 8, no. 2, pp. 344–351, 1996.

[49] Y. Hamada, "The development of chelate metal complexes as an organic electroluminescent material," *Ieee Transactions on Electron Devices*, vol. 44, no. 8, pp. 1208–1217, 1997.

[50] L. S. Sapochak, A. Padmaperuma, N. Washton, F. Endrino, G. T. Schmett, J. Marshall, D. Fogarty, P. E. Burrows, and S. R. Forrest, "Effects of systematic methyl substitution of metal (iii) tris(n-methyl-8-quinolinolato) chelates on material properties for optimum electroluminescence device performance," *Journal of the American Chemical Society*, vol. 123, no. 26, pp. 6300–6307, 2001.

[51] L. S. Sapochak, F. E. Benincasa, R. S. Schofield, J. L. Baker, K. K. C. Riccio, D. Fogarty, H. Kohlmann, K. F. Ferris, and P. E. Burrows, "Electroluminescent zinc(ii) bis(8-hydroxyquinoline): Structural effects on electronic states and device performance," *Journal of the American Chemical Society*, vol. 124, no. 21, pp. 6119–6125, 2002.

[52] L. S. Hung and C. H. Chen, "Recent progress of molecular organic electroluminescent materials and devices," *Materials Science and Engineering R-Reports*, vol. 39, no. 5-6, pp. 143–222, 2002.

[53] P. C. P. Hrudey, B. Szeto, and M. J. Brett, "Strong circular bragg phenomena in self-ordered porous helical nanorod arrays of alq3," *Applied Physics Letters*, vol. 88, no. 25, p. 251106, 2006.

[54] J. C. Sit, *Thin film/liquid crystal composite optical materials and devices*. PhD thesis, University of Alberta, 2002.

[55] M. Brinkmann, G. Gadret, M. Muccini, C. Taliani, N. Masciocchi, and A. Sironi, "Correlation between molecular packing and optical properties in different crystalline polymorphs and amorphous thin films of mer-tris(8-hydroxyquinoline)aluminum(iii)," *Journal of the American Chemical Society*, vol. 122, no. 21, pp. 5147–5157, 2000.

[56] M. Braun, J. Gmeiner, M. Tzolov, M. Coelle, F. D. Meyer, W. Milius, H. Hillebrecht, O. Wendland, J. U. von Schutz, and W. Brutting, "A new crystalline phase of the electroluminescent material tris(8-hydroxyquinoline) aluminum exhibiting

blueshifted fluorescence," *Journal of Chemical Physics*, vol. 114, no. 21, pp. 9625–9632, 2001.

[57] M. Brinkmann, F. Biscarini, C. Taliani, I. Aiello, and M. Ghedini, "Growth of mesoscopic correlated droplet patterns by high-vacuum sublimation," *Physical Review B*, vol. 61, no. 24, pp. R16339–R16342, 2000.

[58] M. Brinkmann, S. Graff, and F. Biscarini, "Mechanism of nonrandom pattern formation of polar-conjugated molecules in a partial wetting regime," *Physical Review B*, vol. 66, no. 16, p. 165430, 2002.

[59] S. Tsoi, B. Szeto, M. D. Fleischauer, J. G. C. Veinot, and M. J. Brett, "Control of alq3 wetting layer thickness via substrate surface functionalization," *Langmuir*, vol. 23, no. 12, pp. 6498–6500, 2007.

[60] J. G. C. Veinot, H. Yan, S. M. Smith, J. Cui, Q. L. Huang, and T. J. Marks, "Fabrication and properties of organic light-emitting "nanodiode" arrays," *Nano Letters*, vol. 2, no. 4, pp. 333–335, 2002.

[61] M. D. Abramoff, P. J. Magelhaes, and S. J. Ram, "Image processing with imagej," *Biophotonics International*, vol. 11, no. 7, pp. 36–42, 2004.

[62] S. Tsoi, E. Fok, J. C. Sit, and J. G. C. Veinot, "Superhydrophobic, high surface area, 3-d sio2 nanostructures through siloxane-based surface functionalization," *Langmuir*, vol. 20, no. 24, pp. 10771–10774, 2004.

[63] J. E. Malinsky, J. G. C. Veinot, G. E. Jabbour, S. E. Shaheen, J. D. Anderson, P. Lee, A. G. Richter, A. L. Burin, M. A. Ratner, T. J. Marks, N. R. Armstrong, B. Kippelen, P. Dutta, and N. Peyghambarian, "Nanometer-scale dielectric self-assembly process for anode modification in organic light-emitting diodes. consequences for charge injection and enhanced luminous efficiency," *Chemistry of Materials*, vol. 14, no. 7, pp. 3054–3065, 2002.

[64] J. G. C. Veinot and T. J. Marks, "Toward the ideal organic light-emitting diode. the versatility and utility of interfacial tailoring by cross-linked siloxane interlayers," *Accounts of Chemical Research*, vol. 38, pp. 632–643, 2005.

[65] R. N. Wenzel, "Resistance of solid surfaces to wetting by water," *Industrial and Engineering Chemistry*, vol. 28, no. 8, pp. 988–994, 1936.

[66] J. C. Vickerman, *Surface Analysis-The Principle Techniques*. John Wiley and Sons, 1997.

[67] D. Y. Kwok, C. N. C. Lam, A. Li, A. Leung, R. Wu, E. Mok, and A. W. Neumann, "Measuring and interpreting contact angles: a complex issue," *Colloids and Surfaces A-Physicochemical and Engineering Aspects*, vol. 142, no. 2-3, pp. 219–235, 1998.

[68] T. J. Markley, J. A. Marsella, E. A. Robertson, G. E. Parris, Z. Zarkov, V. Jakubek, and C. K. Ober, "Wetting and dissolution studies of fluoropolymers used in 157 nm photolithography applications," *Journal of Vacuum Science and Technology B*, vol. 22, no. 1, pp. 140–145, 2004.

[69] M. W. M. Seto, *Mechanical Response of Microspring Thin Films*. PhD thesis, University of Alberta, 2004.

[70] D. Z. Garbuzov, V. Bulovic, P. E. Burrows, and S. R. Forrest, "Photoluminescence efficiency and absorption of aluminum-tris-quinolate (alq(3)) thin films," *Chemical Physics Letters*, vol. 249, no. 5-6, pp. 433–437, 1996.

[71] A. Aziz and K. L. Narasimhan, "Optical absorption in alq," *Synthetic Metals*, vol. 114, no. 2, pp. 133–137, 2000.

[72] A. B. Djurisic, C. Y. Kwong, T. W. Lau, E. H. Li, Z. T. Liu, H. S. Kwok, L. S. M. Lam, and W. K. Chan, "Optical functions of tris (8-hydroxyquinoline) aluminum (alq(3)) by spectroscopic ellipsometry," *Applied Physics A-Materials Science and Processing*, vol. 76, no. 2, pp. 219–223, 2003.

[73] Y. Taga and T. Motohiro, "Growth of birefringent films by oblique deposition," *Journal of Crystal Growth*, vol. 99, no. 1-4, pp. 638–642, 1990.

[74] J. Gospodyn and J. C. Sit, "Characterization of dielectric columnar thin films by variable angle mueller matrix and spectroscopic ellipsometry," *Optical Materials*, vol. 29, no. 2-3, pp. 318–325, 2006.

[75] K. Robbie and M. J. Brett, "Sculptured thin films and glancing angle deposition: Growth mechanics and applications," *Journal of Vacuum Science and Technology A*, vol. 15, no. 3, pp. 1460–1465, 1997.

[76] I. Hodgkinson, Q. H. Wu, and J. Hazel, "Empirical equations for the principal refractive indices and column angle of obliquely deposited films of tantalum oxide, titanium oxide, and zirconium oxide," *Applied Optics*, vol. 37, no. 13, pp. 2653–2659, 1998.

[77] D. Vick, T. Smy, and M. J. Brett, "Growth behavior of evaporated porous thin films," *Journal of Materials Research*, vol. 17, no. 11, pp. 2904–2911, 2002.

[78] A. C. van Popta, J. C. Sit, and M. J. Brett, "Optical properties of porous helical thin films," *Applied Optics*, vol. 43, no. 18, pp. 3632–3639, 2004.

[79] A. Lakhtakia, R. Messier, M. J. Brett, and K. Robbie, "Sculptured thin film (stfs) for optical, chemical, and biological applications," *Innovations in Materials Research*, vol. 1, no. 2, pp. 167–176, 1996.

[80] V. I. Kopp, Z. Q. Zhang, and A. Z. Genack, "Lasing in chiral photonic structures," *Progress in Quantum Electronics*, vol. 27, no. 6, pp. 369–416, 2003.

[81] I. Hodgkinson, Q. H. Wu, and S. Collet, "Dispersion equations for vacuum-deposited tilted-columnar biaxial media," *Applied Optics*, vol. 40, no. 4, pp. 452–457, 2001.

[82] G. Beydaghyan, K. Kaminska, T. Brown, and K. Robbie, "Enhanced birefringence in vacuum evaporated silicon thin films," *Applied Optics*, vol. 43, no. 28, pp. 5343–5349, 2004.

[83] G. Beydaghyan, C. Buzea, Y. Cui, C. Elliott, and K. Robbie, "Ex situ ellipsometric investigation of nanocolumns inclination angle of obliquely evaporated silicon thin films," *Applied Physics Letters*, vol. 87, no. 15, p. 153103, 2005.

[84] B. Johs, J. A. Woollam, C. M. Herzinger, J. Hilfiker, R. Synowicki, and C. L. Bungay, "Overview of variable angle spectroscopic ellipsometry (vase), part ll: Advanced applications," in *Optical Metrology* (G. A. Al-Jumaily, ed.), vol. CR72, (Denver), pp. 29–58, SPIE - The international Society for Optical Engineers, 1999.

[85] J. A. Woollam, B. Johs, C. M. Herzinger, J. Hilfiker, R. Synowicki, and C. L. Bungay, "Overview of variable angle spectroscopic ellipsometry (vase), part 1: Basic theory and typical applications," in *Optical Metrology* (G. A. Al-Jumaily, ed.), vol. CR72, (Denver), pp. 3–28, SPIE - The international Society for Optical Engineers, 1999.

[86] A. B. Djurisic, C. Y. Kwong, W. L. Guo, T. W. Lau, E. H. Li, Z. T. Liu, H. Kwok, L. S. M. Lam, and W. K. Chan, "Spectroscopic ellipsometry of the optical functions of tris (8-hydroxyquinoline) aluminum (alq3)," *Thin Solid Films*, vol. 416, pp. 233–241, 2002.

[87] C. M. Herzinger, B. Johs, W. A. McGahan, J. A. Woollam, and W. Paulson, "Ellipsometric determination of optical constants for silicon and thermally grown silicon dioxide via a multi-sample, multi-wavelength, multi-angle investigation," *Journal of Applied Physics*, vol. 83, no. 6, pp. 3323–3336, 1998.

[88] D. E. Aspnes, "Optical-properties of thin-films," *Thin Solid Films*, vol. 89, no. 3, pp. 249–262, 1982.

[89] G. B. Smith, "Effective medium theory and angular-dispersion of optical-constants in films with oblique columnar structure," *Optics Communications*, vol. 71, no. 5, pp. 279–284, 1989.

[90] W. S. Weiglhofer, A. Lakhtakia, and B. Michel, "Maxwell garnett and bruggeman formalisms for a particulate composite with bianisotropic," *Microwave and Optical Technology Letters*, vol. 15, no. 4, pp. 263–266, 1997.

[91] T. C. Choy, *Effective Medium Theory Principles and Applications*. Oxford University Press, Oxford, 1999.

[92] B. Szeto, P. C. P. Hrudey, M. Taschuk, and M. J. Brett, "Circularly polarized luminescence from chiral thin films," in *Photonics West 2006*, vol. Proc. of SPIE 6135, (San Jose, CA), p. 613511, The International Society for Optical Engineering (SPIE), 2006.

[93] I. Hodgkinson and Q. H. Wu, "Vacuum deposited biaxial thin films with all principal axes inclined to the substrate," *Journal of Vacuum Science and Technology A-Vacuum Surfaces and Films*, vol. 17, no. 5, pp. 2928–2932, 1999.

[94] K. D. Harris, D. Vick, T. Smy, and M. J. Brett, "Column angle variations in porous chevron thin films," *Journal of Vacuum Science and Technology A-Vacuum Surfaces and Films*, vol. 20, no. 6, pp. 2062–2067, 2002.

[95] Y. Hamada, T. Sano, M. Fujita, T. Fujii, Y. Nishio, and K. Shibata, "Organic electroluminescent devices with 8-hydoxyquinoline derivative-metal complexes as an emitter," *Jpn. J. Appl. Phys.*, vol. 32, no. Part 2, No. 4A, pp. L514–L515, 1993.

[96] D. Datta, V. Tripathi, C. K. Suman, V. K. Shukla, and S. Kumar, "Optical properties of electroluminescent zinc(llbis(8-hydroxyquinoline) thin films prepared at different deposition rates," in *The 9th Asian Symposium on Information Display*, (New Delhi, India), pp. 206–209, 2006.

[97] I. Hodgkinson, Q. H. Wu, B. Knight, A. Lakhtakia, and K. Robbie, "Vacuum deposition of chiral sculptured thin films with high optical activity," *Applied Optics*, vol. 39, no. 4, pp. 642–649, 2000.

[98] M. J. Colgan, B. Djurfors, D. G. Ivey, and M. J. Brett, "Effects of annealing on titanium dioxide structured films," *Thin Solid Films*, vol. 466, no. 1-2, pp. 92–96, 2004.

[99] J. Zhang, I. Salzmann, S. Rogaschewski, J. P. Rabe, N. Koch, F. Zhang, and Z. Xu, "Arrays of crystalline c60 and pentacene nanocolumns," *Appl. Phys. Lett.*, vol. 90, p. 193117, 2007.

[100] D. S. Qin, D. C. Li, Y. Wang, J. D. Zhang, Z. Y. Xie, G. Wang, L. X. Wang, and D. H. Yan, "Effects of the morphologies and structures of light-emitting layers on the performance of organic electroluminescent devices," *Applied Physics Letters*, vol. 78, no. 4, pp. 437–439, 2001.

[101] J. M. Chung, Y. Z. Luo, Z. A. Jian, M. C. Kuo, C. S. Yang, W. C. Chou, and K. C. Chiu, "Effects of substrate temperature on the properties of alq(3) amorphous layers prepared by vacuum deposition," *Jpn. J. Appl. Phys.*, vol. 43, no. 4A, pp. 1631–1632, 2004.

Appendix A

Maple Code

The error calculation in the BEMA description of the birefringence in slanted columnar thin films was calculated based on the fit results provided by the VASE software. The values were given an error bar corresponding to the 90% confidence limit which was used to compute any error bars that appear in the calculation of the birefringence using the mathematical analytic software Maple. All values corresponding to the error in a particular measurement preceeded by a "d_".

```
Calculation for the x-depolarization factor, qx
> q[1]:=(1-q[3])*xy_split:

Calculation for the error in qx
> d_q[1]:=xy_split*d_q[3] + (1-q[3])*d_xy_split:

Calculation for the y-depolarization factor, qy
> q[2]:=1-q[3]-q[1]:

and its error
> d_q[2]:=d_q[3]+d_q[1]:

Computation for the dielectric constants
> for i from 1 to 3 do

> e[i]:=1/2/(-1+q[i])*(-rho*e_mat+e_void*q[i]+e_mat
```

```
*q[i]-e_void+rho*e_void-sqrt(-2*rho^2*e_mat*e_void+2
*rho*e_mat*e_void+rho^2*e_mat^2+e_void^2-2*rho*e_void
^2+rho^2*e_void^2+2*e_void^2*q[i]*rho-2*e_void*q[i]^2
*e_mat-2*rho*e_mat^2*q[i]+2*e_mat*e_void*q[i]+e_mat^2
*q[i]^2-2*e_void^2*q[i]+e_void^2*q[i]^2));
```

Computation for the error in the dielectric constant

```
> d_e[i]:=1/2*abs(1/(-1+q[i])*(-e_mat+e_void-1/2
*1/(-2*rho^2*e_mat*e_void+2*rho*e_mat*e_void+rho^2
*e_mat^2+e_void^2-2*rho*e_void^2+rho^2*e_void^2+2
*e_void^2*q[i]*rho-2*e_void*q[i]^2*e_mat-2*rho
*e_mat^2*q[i]+2*e_mat*e_void*q[i]+e_mat^2*q[i]^2
-2*e_void^2*q[i]+e_void^2*q[i]^2)^(1/2)*(-4*rho*e_mat
*e_void+2*e_void*e_mat+2*rho*e_mat^2-2*e_void^2+2*rho
*e_void^2+2*e_void^2*q[i]-2*e_mat^2*q[i])))*d_rho
+abs(-1/2/(-1+q[i])^2*(-rho*e_mat+e_void*q[i]+e_mat
*q[i]-e_void+rho*e_void-sqrt(-2*rho^2*e_mat*e_void+2
*rho*e_mat*e_void+rho^2*e_mat^2+e_void^2-2*rho*e_void
^2+rho^2*e_void^2+2*e_void^2*q[i]*rho-2*e_void*q[i]^2
*e_mat-2*rho*e_mat^2*q[i]+2*e_mat*e_void*q[i]+e_mat^2
*q[i]^2-2*e_void^2*q[i]+e_void^2*q[i]^2))+1/2/(-1
+q[i])*(e_void+e_mat-1/2*1/(-2*rho^2*e_mat*e_void+2
*rho*e_mat*e_void+rho^2*e_mat^2+e_void^2-2*rho*e_void
^2+rho^2*e_void^2+2*e_void^2*q[i]*rho-2*e_void*q[i]^2
*e_mat-2*rho*e_mat^2*q[i]+2*e_mat*e_void*q[i]+e_mat^2
*q[i]^2-2*e_void^2*q[i]+e_void^2*q[i]^2)^(1/2)*(2*rho
*e_void^2-4*e_mat*e_void*q[i]-2*rho*e_mat^2+2*e_void
*e_mat+2*e_mat^2*q[i]-2*e_void^2+2*e_void^2*q[i])))
*d_q[i];
```

Computation for the three principal indices of

```
refraction and the error in each value
> n[i]:=Re(sqrt(e[i]));

> d_N[i]:=1/2/(e[i])^(1/2)*Re(d_e[i])+1/2/(e[i])^(1/2)
          *Im(d_e[i]):

> d_n[i]:=Re(d_N[i]);

> od;
                  e[1] :=
                       d_e[1] :=
                         n[1] :=
               d_N[1] :=
                       d_n[1] :=

                  e[2] :=
                       d_e[2] :=
                         n[2] :=
               d_N[2] :=
                       d_n[2] :=

                  e[3] :=
                       d_e[3] :=
                         n[3] :=
               d_N[3] :=
                       d_n[3] :=

Computation for the index in the np direction and
the error in the value
> np:=evalf( (sin(beta)/n[3])^2
             + (cos(beta)/n[2])^2 )^(-1/2);
```

np :=

```
> d_np:=1/2*abs(1/(sin(beta)^2/n[3]^2+cos(beta)
^2/n[2]^2)^(3/2)*(2*sin(beta)/n[3]^2*cos(beta)-2
*cos(beta)/n[2]^2*sin(beta)))*d_B+abs(1/(sin(beta)
^2/n[3]^2+cos(beta)^2/n[2]^2)^(3/2)*sin(beta)^2/n[3]
^3)*d_n[3]+abs(1/(sin(beta)^2/n[3]^2+cos(beta)^2/n[2]
^2)^(3/2)*cos(beta)^2/n[2]^3)*d_n[2]:
```

Computation for the in-plane birefringence

```
> inplane_biref:=n[1]-evalf(np);
```

inplane_biref :=

Computation for the error in the in-plane birefringence

```
> d_inplane_biref:=d_n[1]+evalf(d_np);
```

d_inplane_biref :=